ELECTROLYTE ENGINEERING FOR MAGNESIUM RECHARGEABLE BATTERIES

CHEN FEIYANG

PhD

The Hong Kong Polytechnic University

2025

The Hong Kong Polytechnic University
Department of Industrial and Systems Engineering

Electrolyte Engineering for Magnesium Rechargeable Batteries

Chen Feiyang

A thesis submitted in partial fulfillment of the requirements for the degree of Doctor of Philosophy

July 2025

CERTIFICATE OF ORIGINALITY

I hereby declare that this thesis is my own work and that, to the best of my knowledge and belief, it reproduces no material previously published or written, nor material that has been accepted for the award of any other degree or diploma, except where due acknowledgement has been made in the text.

Signature: _____

Name of Student: CHEN Feiyang

Abstract

Achieving carbon neutrality hinges on the widespread adoption of clean renewable energy sources, which in turn necessitates the development of electrochemical storage devices with high energy density, safety, and cost-effectiveness. To meet decarbonization goals, research is increasingly focused on electrochemical storage systems beyond lithium-ion batteries (LIBs), which face limitations due to scarce lithium resources, safety concerns, and potential environmental impacts. Magnesium rechargeable batteries (MRBs) are promising alternatives owing to magnesium's abundance, high volumetric capacity, and superior safety. However, the development of MRBs is still in its infancy, with several challenges impeding their practical applications. In conventional electrolytes, Mg^{2+} exhibits a stronger polarizing effect compared to lithium ions, which, along with surface passivation on magnesium metal anode, often result in sluggish diffusion kinetics and suboptimal Mg^{2+} storage performance. Thus, designing electrolytes compatible with both high-capacity cathodes and anodes is crucial for advancing MRBs. This thesis presents a comprehensive study on developing new electrolytes for MRBs. By optimizing the chemical structures of the electrolytes and exploring their interface characteristics, a series of formulations have been developed that enable reversible MRBs with excellent electrochemical performance. This breakthrough is expected to significantly facilitate the commercialization of MRBs.

Firstly, a novel Mg^{2+}-conducting solid-state electrolyte (MCE) is introduced, created by directly crystalizing deep eutectic solvents composed of $Mg(TFSI)_2$ and urea at room temperature for safe and sustainable solid-state magnesium rechargeable batteries (SSMRBs). The abundant amine and carbonyl groups in urea ligands greatly tailored the intermolecular frameworks of MCE, resulting in anion-rich groups within the Mg^{2+} solvation sheath. This structure mitigates surface passivation caused by solvent decomposition that commonly observed in liquid electrolytes, *i.e.*, $Mg(TFSI)_2$/PC. Consequently, when applied in the Mg//Mg symmetric cells, an appreciable cycle life of more than 120 h at 25 μA cm^{-2} can be achieved.

The improved electrochemical performance is attributed to the F-rich and porous organic/inorganic hybrid interface layer, which effectively activates Mg metal and facilitates rapid Mg^{2+} transport across the interface. Finally, solid-state Mg//V_2O_5 full cells were constructed to demonstrate the practical feasibility of MCE, achieving a high capacity of 172 mAh g^{-1} at 20 mA g^{-1}. This work is anticipated as the way of developing novel solid-state electrolytes for safer MRBs.

Secondly, a cosolvent electrolyte composed of $Mg(TFSI)_2$ salt combined with ethylene glycol (EG) and 1,2-dimethoxyethane (DME) cosolvents is investigated. This formulation tackles the issues of sluggish Mg^{2+} desolvation at cathode-electrolyte interface (CEI) and the $TFSI^-$-induced surface passivation in typical $Mg(TFSI)_2$/DME electrolyte. Hydroxyl-rich EG molecules destabilize unfavorable $[Mg(DME)_3]^{2+}$ complexes and form hydrogen bond networks, thereby facilitating Mg ion migration and suppress $TFSI^-$ decomposition. As a result, the co-solvent electrolyte achieves a high reversible capacity of 258 mAh g^{-1} for VO_2 cathodes, with an exceptionally low capacity degradation rate of 0.0078 % per cycle over 2000 cycles at 500 mA g^{-1}, comparable to state-of-the-art Mg ion battery cathodes. The practical applicability of this electrolyte is further demonstrated by Mg//VO_2 full cells, which maintain capacities above 160 mAh g^{-1} over 50 cycles. This work establishes a new benchmark for effective electrolytes in RMBs, offering both long cycle life and high energy density.

Thirdly, a novel sulfolane hydrated eutectic electrolyte (HEE) consisting of optimized ratios of $Mg(ClO_4)_2 \cdot 6H_2O$ and sulfolane (SL) is explored, which can comprehensively reduce V_2O_5 cathode dissolution and achieve a stable and high capacity output for MRBs. In bulk electrolyte, the S=O group in the sulfolane disrupts the continuous hydrogen bonding network among water molecules, thereby reducing water activity. Additionally, its participation in Mg^{2+} solvation structure decreases interfacial bound water content and facilitates Mg^{2+} de-solvation at the CEI. Furthermore, sulfolane's preferential adsorption on the CEI protects V_2O_5 from water exposure, strengthening the structural stability of the cathode. As a result, the optimized

HEE enables V_2O_5 cathode to achieve a high capacity of 322.7 mAh g^{-1} at 50 mA g^{-1} and exceptional lifespan lasting for over 5000 cycles with a minimal capacity degradation rate of 0.0061% per cycle at 1000 mA g^{-1}. As a proof of concept, a full PTCDA//V_2O_5 battery with HEE demonstrates a capacity exceeding 190 mAh g^{-1} for over 200 cycles. This electrolyte represents a new avenue for developing high-energy and high-stable multivalent ion batteries.

List of Publications

#Equal contribution first author; *Corresponding author.

Journal papers

[1] **Feiyang Chen**, Qi Meng, Hui Wang, Jingya Yu, Renjie Li, Yuyang Yi, Yingkai Hua, Huijun Lin, Pengyan Jiang, Kang Cheung Chan, Zheng-Long Xu*, Glycol-glyme co-solvent electrolytes enable high-capacity and ultrastable VO_2 cathodes in magnesium ion batteries, *Nano Energy*, 2025, 111191.

[2] **Feiyang Chen,** Jingya Yu, Renjie Li, Fangyi Shi, Xiangli Che, Kang Cheung Chan, Yang Sun, Zheng-Long Xu*, Direct crystallization of deep eutectic solvent into solid-state electrolyte for magnesium metal batteries, *J. Power Sources*, 2024, 611, 234780.

[3] **Feiyang Chen**, Zheng-Long Xu*, Design and manufacture of high-performance microbatteries: lithium and beyond, *Microstructures*, 2022, 2 (10), 1.

[4] Huijun Lin#, Jingya Yu#, **Feiyang Chen**#, Renjie Li, Baoyu Xia*, Zheng-Long Xu*, Visualizing the interfacial chemistry in multivalent metal anodes by transmission electron microscopy, *Small Methods*, 2023, 2300561.

[5] **Feiyang Chen**, Hongxi Zeng, Qi Meng, Huijun Lin, Yuyang Yi, Renjie Li, Pengyan Jiang, Chuheng Cao, Kang Cheung Chan, Zheng-Long Xu*, Ultra-Stable aqueous magnesium ion batteries enabled by a sulfolane-based hydrated eutectic electrolyte with enhanced cathode stability, submitted.

[6] Huijun Lin, Zhen Zhan, Hongxi Zeng, Renjie Li, Yuyang Yi, **Feiyang Chen**, Songhua Cai, Ye Zhu, Chi Fai Cheung, Zheng-Long Xu*, Ultrastable Calcium Metal Anodes Enabled by a Strongly Coordinated Electrolyte Derived Bilayer Solid Electrolyte Interphase, *Adv. Mater.*, 2025, e10711.

[7] Renjie Li, Youngsu Lee, Zizheng Song, Siyuan Ma, Yuyang Yi, Huijun Lin, Yingkai Hua, Pengyan Jiang, **Feiyang Chen**, Jingya Yu, Xiangjun Pu, Zibin Chen, Kang Cheung Chan, Kyu-Young Park, Zheng-Long Xu*, Enabling Multielectron Reaction of Polyanionic Cathodes Toward High-Energy Calcium Rechargeable Batteries, *Adv. Mater.*, 2025, e06603.

[8] Jingya Yu, Zizheng Song, Qi Qi, Xiaobin Hui, Yiyuan Ma, **Feiyang Chen**, Kai Qi, Qi Meng, Renjie Li, Lyuchao Zhuang, Kang Cheung Chan, Zibin Chen, Bao Yu Xia, Zheng-Long Xu*, Sabatier principle inspired bifunctional alloy interface for stable and high-depth discharging zinc metal anodes, *Angew. Chem. Int. Ed.*, 2025, 15, e202423236.

[9] Renjie Li, Youngsu Lee, Huijun Lin, Xiangli Che, Xiangjun Pu, Yuyang Yi, **Feiyang Chen**, Jingya Yu, Kang Cheung Chan, Kyu-Young Park, Zheng-Long Xu*, KxVPO4F (x~0): a new high-voltage and low-stain cathode material for ultrastable calcium rechargeable batteries, *Adv.*

Energy Mater., 2024, 14, 2302700.

[10] Ruiting Liu, Zheng-Long Xu*, Fumin Li, **Feiyang Chen,** Jingya Yu, Ya Yan, Yu Chen, Baoyu Xia. Recent advances in proton exchange membrane water electrolysis, Chem. Soc. Rev., 2023, 52(16), 5652-5683.

[11] Renjie Li, Jingya Yu, **Feiyang Chen**, Yaqiang Su, Kang Cheung Chan, Zheng-Long Xu*, High-power and ultrastable aqueous calcium-ion batteries enabled by small organic molecular crystal anodes, *Adv. Funct. Mater.*, 2023, 33, 2214304.

[12] Jingya Yu, Chunhong Chen, Fangyi Shi, Renjie Li, **Feiyang Chen**, Zheng-Long Xu*, A multifunctional MXene-polydopamine interface enabling stable and dendrite-free zinc metal batteries, *Energy Storage Mater.*, 2023, 63, 102966.

Conference presentations

[1] **Feiyang Chen**, Zheng-Long Xu*, A sulfolane-based hydrated eutectic electrolyte inhibits cathode dissolution for ultra-stable aqueous magnesium ion batteries, PolyU Research Student Conference, Hong Kong, July 2025.

[2] **Feiyang Chen**, Zheng-Long Xu*, High-Capacity and Ultrastable Magnesium Batteries Enabled by Unique Solvation Reorganization in a Hybrid-Solvent Electrolyte, PRiME 2024, Honolulu, USA, October 2024.

[3] **Feiyang Chen**, Zheng-Long Xu*, Ethylene Glycol (EG)/Ether Hybrid Solvents Enabled Unique Solvation Reorganization for High-Performance Mg Batteries, the 5th International Conference on Energy Storage Materials, Shenzhen, China, April 2024.

[4] **Feiyang Chen**, Zheng-Long Xu*, $Mg(TFSI)_2$-based solid-state eutectic electrolyte towards safer magnesium batteries, The 243rd ECS Meeting, Boston, USA, May 2023.

[5] **Feiyang Chen**, Zheng-Long Xu*, A new chloride-free solid-state eutectic electrolyte for magnesium rechargeable batteries, PolyU Research Student Conference, Hong Kong, May 2023.

Acknowledgments

This thesis is the culmination of a journey that would not have been possible without the support, guidance, and love of many individuals.

In the first place, I would like to express my sincere gratitude to my chief supervisor, Prof. Xu Zheng-Long, for his patient guidance throughout my PhD career. His efficient feedback and constructive criticism on each of my work help me think critically and creatively, which laid the foundation for my future development.

In addition, I would like to extend my sincere thanks to my co-supervisor, Prof. Kang Cheung Chan, for his valuable insights and support throughout this research. I would also like to thank my coauthors and colleagues, Dr. Liu Ruiting, Dr. Yi Yuyang, Dr. Wang hui, Dr. Xue Weijiang, Dr. Sun Yang, Dr. Che Xiangli, Dr. Li Renjie, Dr. Lyu Linlong, Dr. Shi Fangyi, Dr. Yu jingya, Miss Lin Huijun, Mr. Meng Qi, Mr. Hua Yingkai, Mr. Jiang Pengyan, and Mr. Zeng Hongxi. Your camaraderie, support, and the countless hours we spent discussing ideas have been a source of motivation and joy. You have made this journey not only bearable but also enjoyable.

A special thanks to the Hong Kong Polytechnic University for providing me the Presidential PhD Fellowship that made this research possible. Your generosity has been instrumental in allowing me to pursue my academic goals.

To my family, words cannot express the depth of my gratitude. To my parents and grandparents, thank you for your unconditional love, sacrifices, and for always believing in me. Your support has been my anchor throughout this journey.

Finally, I would like to acknowledge my personal growth throughout this research journey. I have successfully overcome my own limitations and am proud of this achievement. This experience has strengthened my confidence in my ability to address and surmount future challenges.

Table of Contents

List of Figures

List of Tables

Chapter 1 Introduction

1.1 Electrochemical energy storage

The rapid development of modern society relies heavily on the continuous supply of electrical energy. In the past decades, electricity production has primary depended on the combustion of fossil fuels like coal, oil, natural gas, *etc.* However, the fast depletion of these limited resources, along with environmental issues such as global warming, oil spills, ocean acidification, highlights the urgent need for sustainable energy storage technologies [1, 2]. Consequently, tremendous efforts have been made to explore renewable energy technologies, including solar, wind, and hydroelectric power. Although these technologies are nearly zero carbon dioxide emission for electricity production, their inherent intermittency and uneven geographical distribution increase the cost and uncertainty of energy storage [3].

To address these challenges and ensure a stable power supply from renewable sources, efficient and reliable electrochemical energy storage (EES) technologies are seen as a promising solution. They offer advantages such as non-pollution, flexible operation, long-cycling stability, and low maintenance requirements. Among various EES systems, lithium-ion batteries (LIBs) stand out and demonstrate excellent application prospects. Since Sony introduced the first commercialized LIBs in 1991 [4], these batteries have dominated the EES market for the past three decades. Their popularity is largely due to their high energy density (approximately 200 Wh kg^{-1}) and superior cyclic stability [5]. As an intercalation-based system, rechargeable LIBs are widely used in various power devices, from portable electronics to electric vehicles and even stationary energy storage systems [6]. However, current commercial LIBs are not ideal for large-scale electrochemical energy storage. First, lithium is scarce in the Earth's crust (0.0017 wt%) and unevenly distributed, promoting the European Commission (EU) to classify lithium and cobalt as critical raw materials due to supply shortage risks [7]. Although China ranks third globally in lithium production in 2024 (33,000 metric tons, see **Table 1.1**), the low quality and dispersed nature of its reserves necessitate substantial imports [8], which is unfriendly to large-

scale domestic production. As global battery demand continues to rise, these resource constraints are expected to impede future deployment, mirroring challenges faced by fossil fuel-based technologies and potentially leading to significant geopolitical tensions. Secondly, the high reactivity of lithium metal and the propensity for dendrite formation in organic electrolyte present considerable safety hazards and introduce uncertainty in battery performance [9]. Therefore, it is imperative to develop alternative EES technologies beyond LIBs with lower cost, enhanced safety, and greater environmental benignity.

Table 1.1 Major countries in worldwide lithium mine production in 2024 (Data from US Geological Survey).

Country	Lithium production (in metric tons)
Australia	86,000
Chile	44,000
China	33,000
Argentina	9,600
Brazil	4,900
Zimbabwe	3,400
Canada	3,400
Portugal	380

1.2 From lithium-ion batteries to magnesium rechargeable batteries

1.2.1 The Advantages of magnesium rechargeable batteries

In response to rising global energy demands, the past two decades have seen significant research efforts directed toward the development of multivalent ion batteries (MIBs), including systems based on Mg^{2+}, Ca^{2+}, Zn^{2+}, and Al^{3+} ions [10]. Compared to LIBs, MIBs offer the potential for substantially higher energy densities, as their charge carriers can transfer two or three electrons per charge carrier. Among these, magnesium rechargeable batteries (MRBs) are considered particularly promising alternatives to LIBs due to several advantageous properties of Mg element [11-13]. (i) Magnesium is the seventh most abundant element in the Earth's crust (2.4 wt% versus 0.0017 wt% for Li) and is widely distributed worldwide. Notably, China accounts for

approximately ~ 61.3% of global magnesium production (**Figure 1.1a**) and over 80% of global magnesium exports, which can reduce raw material costs and ensure a stable supply for large-scale applications [14]. (ii) The divalent nature of Mg^{2+} enables redox reactions involving two electrons per intercalated ions, resulting in a high volumetric capacity of 3833 mAh cm^{-3} nearly double that of monovalent lithium (2062 mAh cm^{-3}) (**Figure 1.1b**). Additionally, magnesium metal possesses a high reduction potential of −2.37 V *vs.* the standard hydrogen electrode (SHE), which, being comparable to lithium's −3.04 V, enables high energy density output. (iii) Magnesium metal also offers enhanced safety, with a significantly higher melting point (650 °C *vs.* 180 °C of lithium), greater electrochemical stability (first ionization energy of 738 kJ mol^{-1} *vs.* 513 kJ mol^{-1} for lithium), and dendrites-free plating behavior [10]. These unique physicochemical properties make MRBs a cost-effective and safe choice for next-generation electrochemical energy storage. Consequently, research interest in MRBs has grown steadily, as evidenced by the increasing number of related publications in recent years (**Figure 1.1d**).

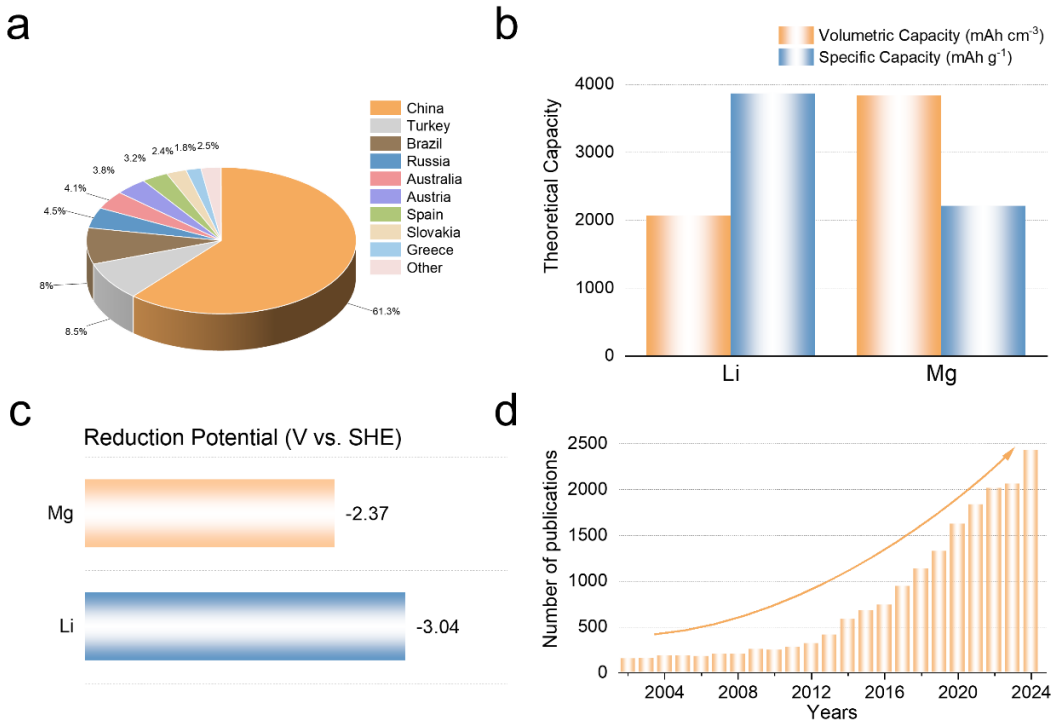

Figure 1.1 (a) Global distribution of magnesium production in 2024 (from US Geological Survey). (b) Comparison of the theoretical volumetric and specific capacities of Mg and Li

metal anodes. (c) Comparison of the reduction potentials of Li and Mg metal anodes. (d) The number of papers published on Mg batteries from 2002 to 2024 (based on Web of Science).

1.2.2 Working principle of magnesium rechargeable batteries

Similar to LIBs, MRBs consist of four main components: an anode, a cathode, an electrolyte, and a separator. The separator physically isolates the anode from the cathode, while permitting electrical connectivity through the external circuit and enabling ionic transport via the electrolyte. This setup enables cyclic energy storage through reversible redox reactions at the anode and cathode, allowing for repeated charge and discharge cycles. **Figure 1.2** illustrates the basic working mechanism of MRBs. The cathode is made of compounds that can reversibly embed and release Mg^{2+} ions, such as Chevrel phase compounds, transition-metal oxides/sulfur, and polyanionic compounds [15, 16]. The anode is composed of magnesium metal, magnesium alloy, or organic materials. In the discharging process, magnesium ions are extracted from the anode and migrate through the electrolyte to the cathode. The cathode material, which can host Mg^{2+} ions, undergoes reduction by accepting these ions. Concurrently, electrons are released at the anode, generating an electric current. During charging, Mg^{2+} ions are extracted from the cathode and migrate back to the anode. These ions are deposited or inserted into the anode materials, while electrons move through the external circuit in the opposite direction to keep charge balance.

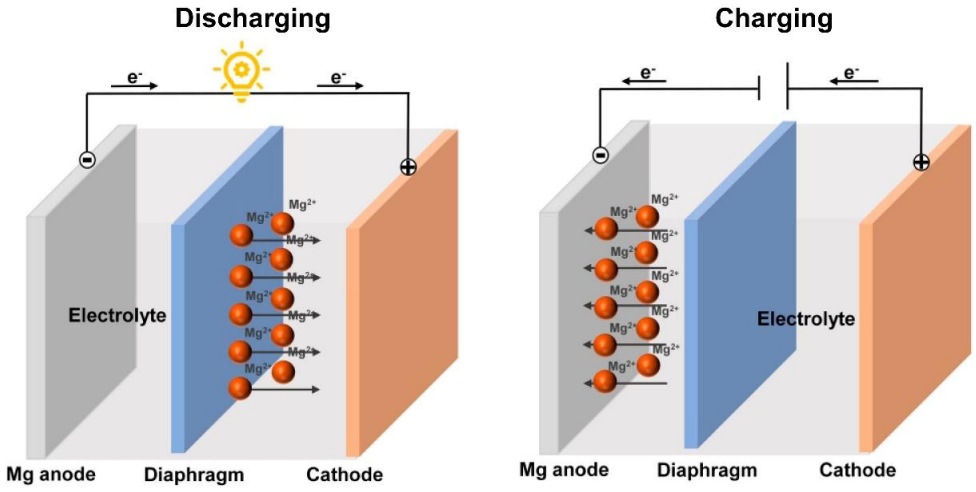

Figure 1.2 Schematic illustration of a magnesium rechargeable battery. [16]

1.2.3 Challenges for magnesium rechargeable batteries

Despite the advantages of magnesium, the development of MRBs has lagged that of LIBs. Research on MRBs began in the early 1990s [17], concurrent with the commercial emergence of LIBs. However, after more than three decades, no commercial MRB devices have been realized. A primary obstacle is the lack of suitable electrolytes that are compatible with both high-capacity cathode and anode, which is critical for reversible MRBs. This challenge stems from the intrinsic properties of Mg^{2+} cations. Compared to monovalent Li^{+} cations, divalent Mg^{2+} cations possess twice the charge density within a similar ionic radius (52 C/mm^3@0.76 Å for Li^{+} *vs.* 120 C/mm^3@0.72 Å for Mg^{2+}, **Figure 1.3**) [18]. While the high charge density of Mg^{2+} contributes to the superior volumetric capacity of Mg^{2+} storage, it also results in strong Coulombic interactions with solvent and anions, leading to sluggish diffusion kinetics at the electrode-electrolyte interface and exacerbating adverse interfacial reactions [19].

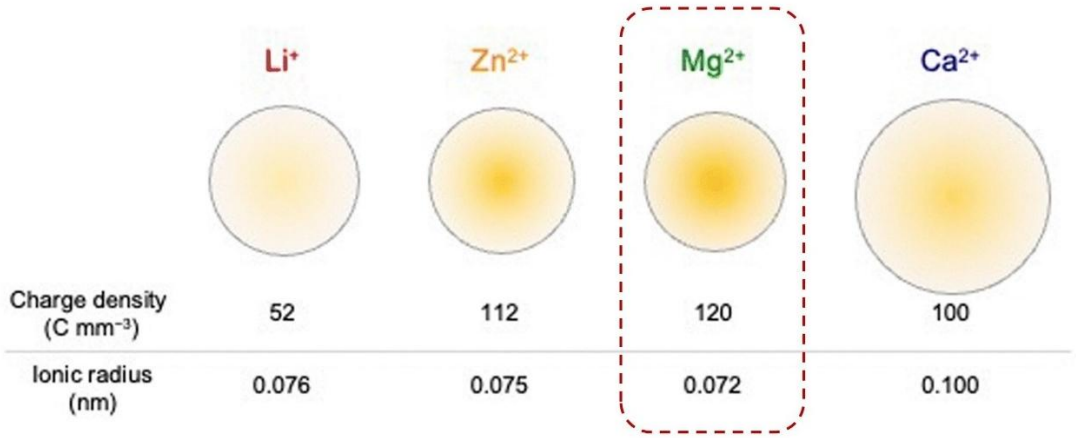

Figure 1.3 (a) Comparison of ionic radii, charge densities, and de-solvation energies of Li^{+} and Mg^{2+} ions. [18]

Specifically, on the anode side, Mg metal anode in conventional organic electrolytes undergoes multiple side reactions with the electrolyte, such as sluggish desolvation and anion decomposition, causing the formation of a passivating layer on the anode surface. This layer blocks Mg^{2+} transport and results in irreversible Mg stripping/plating [20-22]. On the cathode side, the strong polarization of Mg^{2+} significantly increases Coulomb interactions with the host

material, further impeding Mg^{2+} diffusion into the solid hosts and making most high-capacity cathodes incompatible, which ultimately leads to suboptimal energy output. Given the critical role of electrolyte properties in governing Mg^{2+} kinetics and interfacial reactions, it is crucial to develop electrolytes with high compatibility for both electrodes and to establish a clear understanding of their interfacial chemistry to enable the practical implementation of MRBs.

1.3 Electrolyte engineering for magnesium rechargeable batteries

In MRBs, the electrolyte serves as a crucial medium for transporting Mg^{2+} ions between the cathode and anode, while also establishing direct contact with these materials [23]. However, the slow diffusion kinetics of Mg^{2+} ions in conventional electrolytes and poor compatibility at the electrode-electrolyte interface significantly hinder the advancement of MRBs. Electrolyte engineering has been acknowledged as an effective strategy to address these challenges [14, 24]. By introducing suitable additives, the chemical structure of the electrolyte can be tailored to facilitate Mg^{2+} desolvation and diffusion [25]. Simultaneously, a favorable electrode-electrolyte interface might be formed *in situ*, enabling stable Mg stripping/plating process.

Initially, electrolyte engineering efforts focused on improving the compatibility with Mg metal anode. In this context, several typical electrolyte systems, such as all-phenyl complex (APC) and magnesium aluminum chloride complex (MACC), have been developed, due to their ability to enable reversible Mg metal deposition and stripping. However, these chloride-based electrolytes are corrosive to current collectors and battery casings, which undermines their suitability for sustainable and stable operation. As a result, attention has shifted to chloride-free electrolytes, such as $Mg(BH_4)_2$, $Mg(CB_{11}H_{12})_2$, and $Mg(TFSI)_2$, which offer improved anodic stability. Nevertheless, these systems still suffer from low Mg plating/stripping efficiency and unavoidable side reactions, limiting their practical application. Incorporating suitable additives into chloride-free electrolytes may enhance their electrochemical performance, but research in this area remains limited. Meanwhile, with increasing emphasis on safety and energy density, emerging systems such as aqueous and solid-state electrolytes have been proposed, further

expanding the application landscape of MRBs. These advancements will be discussed in detail in the subsequent chapters. Overall, electrolyte engineering is essential for advancing the development and practical implementation of MRBs.

1.3.1 Chloride-based electrolytes: Grignard and non-Grignard systems

Grignard electrolytes

The advancement of electrolyte engineering for MRBs dates back to the 1990s [17] (**Figure 1.4**). During this period, Gregory and his colleagues pioneered the use of single Grignard reagents as nucleophilic electrolytes, enabling the first demonstration of reversible Mg plating/stripping, thereby initiating systematic research on MRBs [17]. Grignard reagents, with the general formula R-Mg-X (where R represents an aliphatic or aromatic hydrocarbon and X is a halogen such as Cl, Br, or I), were initially explored. However, their practical application was hindered by their low anodic stability (<1 V) and limited ionic conductivity, rendering them less competitive compared to LIBs.

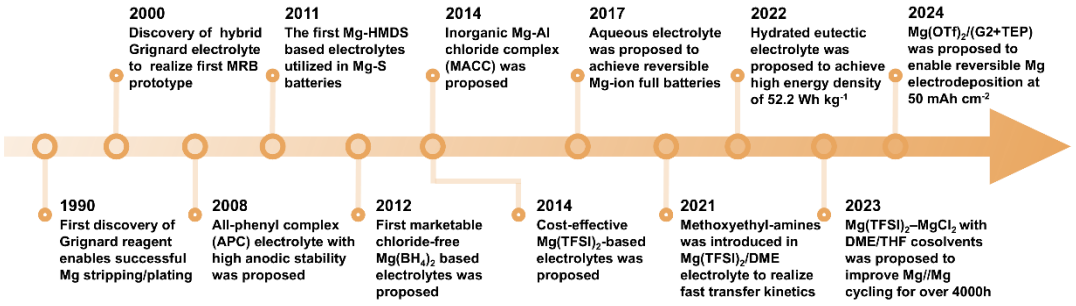

Figure 1.4 The history of representative electrolytes for MRBs.

A decade later, Aurbach *et al.* [26-28] enhanced the Grignard-based electrolyte by incorporating $AlCl_{3-n}R_n$ (R=alkyl:ethyl, butylate) Lewis acid, which improved anodic stability without compromising the high reversibility for Mg plating/stripping. The most effective formulation, 0.25 M $Mg(AlCl_2BuEt)_2$ in tetrahydrofuran (THF), referred to as the butyl ethyl complex (BEC) [26], utilizes dichloroethylaluminum ($EtAlCl_2$) as the Lewis acid and di-n-butylmagnesium (Bu_2Mg) as the Lewis base in a 2:1 molar ratio. This electrolyte achieved nearly 100% Mg plating/stripping reversibility and expanded the electrochemical stability

window to 2.5 V *vs.* Mg^{2+}/Mg. Notably, the first prototype Mg battery, employing a Mg metal anode and a Chevrel phase Mo_6S_8 cathode with this electrolyte, delivered a specific capacity of 75 mAh g^{-1} at an average voltage of 1.2 V over 580 cycles at 0.3 mA cm^{-2} (**Figure 1.5a** and **1.5b**).

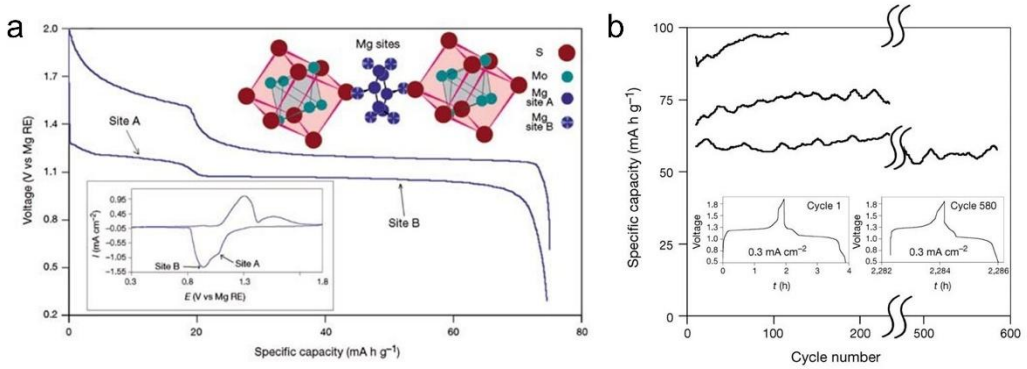

Figure 1.5 (a) Galvanostatic Charge Discharge (GCD) curves and (b) cycling performance of $Mg//Mo_6S_8$ full cell with 0.25 M $Mg(AlCl_2BuEt)_2$/THF electrolyte. [26]

Despite these advancements, the suboptimal anodic stability and ionic conductivity of these complexes remain insufficient for practical applications. Therefore, the development of new electrolyte formulations is critical for further enhancing the electrochemical performance of MRBs. Recognizing that anodic stability is greatly influenced by strength of Al-C bonds, APC was developed via the *in situ* reaction of commercially available phenyl magnesium chloride (PhMgCl) and $AlCl_3$ in THF [29]. Owing to the stronger Al–C bond in phenyl ligands compared to alkyl ligands, APC exhibits an anodic stability up to 3.3 V *vs.* Mg^{2+}/Mg (**Figure 1.6,** red line), nearly 1 V higher than that of the BEC electrolyte. Additionally, APC demonstrates high ionic conductivity (4-5 mS cm^{-1}), reduced overpotential for Mg deposition, and nearly 100% Coulombic efficiency for Mg plating/stripping. As a result, APC has become a benchmark electrolyte for MRBs and continues to be widely utilized in current research.

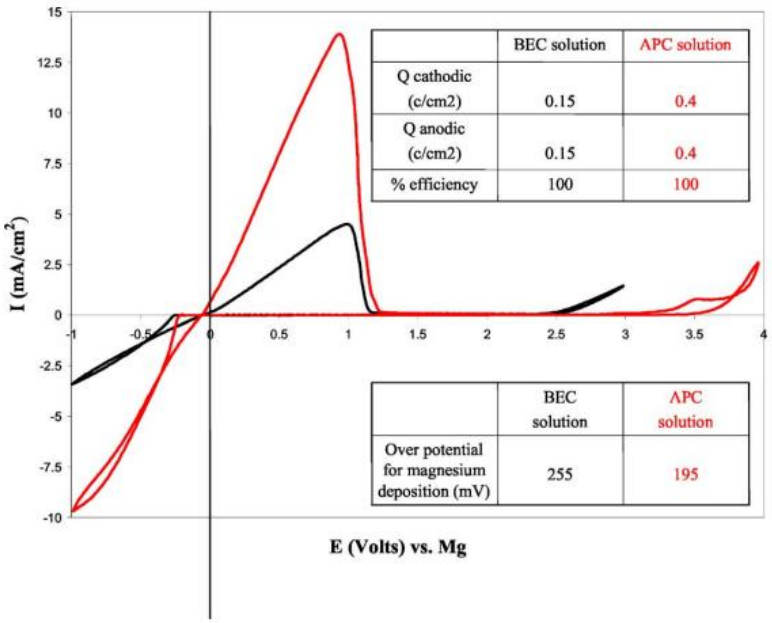

Figure 1.6 Steady-state cyclic voltammogram of APC (red line). [29]

Non-Grignard electrolytes

Although Grignard-based electrolytes exhibit excellent compatibility with Mg metal anode and enable reversible Mg plating/stripping chemistry, the use of high molecular weight Mo_6S_8 cathode determinates the overall energy density output. Furthermore, the nucleophilic nature of these electrolytes renders them incompatible with high-energy cathode such as sulfur.

To achieve higher energy densities, alternative electrolyte systems beyond Grignard reagents have been explored. For instance, Muldoon *et al.* [30] introduced a non-nucleophilic hexamethyldislazide magnesium chloride (HMDSMgCl) based electrolyte (**Figure 1.7a**). When combined with $AlCl_3$ by Lewis acid-base reactions, this electrolyte significantly enhances chemical compatibility with the electrophilic sulfur cathode, enabling an initial capacity of 1200 mAh g^{-1} (**Figure 1.7b**), which demonstrates the first proof-of-concept rechargeable Mg//sulfur battery. Nevertheless, the complexity of materials synthesis and repaid capacity decay with high-energy cathode highlight the need for further electrolyte optimization to meet practical application requirements.

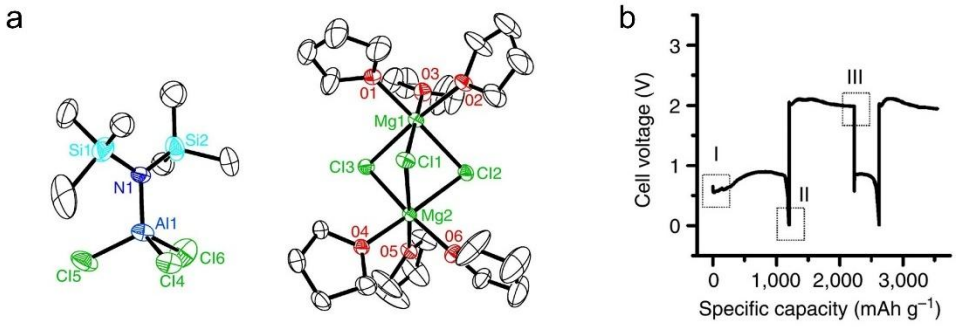

Figure 1.7 (a) ORTEP plot of $[Mg_2Cl_3\text{-}6THF][HMDSAlCl_3]$. (b) Discharging/charging of a Mg//S coin cell at 50 and 25 μA, respectively. [30]

Additionally, the organometallic compounds used in Grignard electrolytes are highly sensitive to air and moisture and exhibit high chemical reactivity with various electrode, severely restricting the development of MRBs. To address these limitations, Aurbach *et al.* [31] proposed the first inorganic MACC electrolyte as a promising alternative for Grignard-based systems. Synthesized via an acid-base reaction between $MgCl_2$ and Lewis acidic $AlCl_3$ in ethereal solvents ($mMgCl_2 + nAlCl_3 \leftrightarrows Mg_mAl_nCl_{[(2*m)+(3*n)]}$), this electrolyte achieves anodic stability up to 3.1 V, a Coulombic efficiency of 98.8%, and an overpotential below 200 mV (**Figure 1.8a** and **1.8b**), offering a potential for the commercialization of high-energy-density MRBs. Subsequently, Ceder *et al.* [32] further elucidated the electrolyte's mechanism, revealing that Al deposition on the Mg metal anode during initial cycles reduces Coulombic efficiency but stabilizes $MgCl^+$ and $AlCl_4^-$ species in the electrolyte, resulting in smoother Mg plating/stripping in subsequent cycles (**Figure 1.8c**).

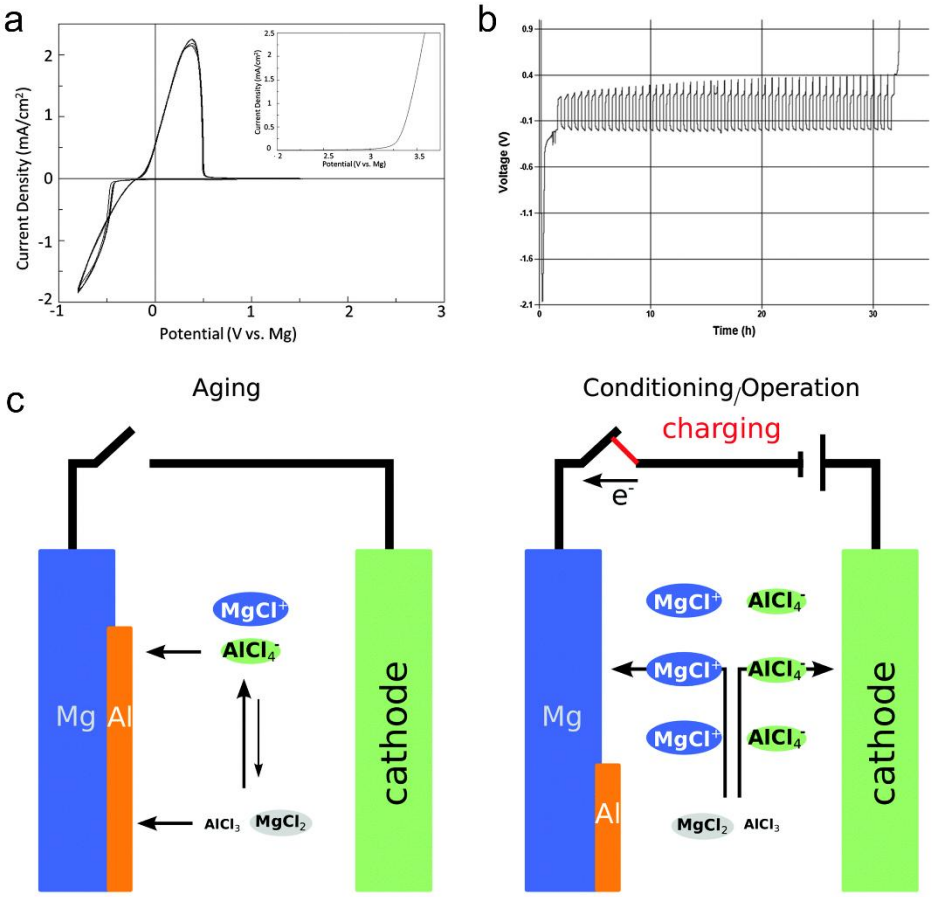

Figure 1.8 (a) Cyclic voltammetry (CV) curves and linear sweep voltammetry (LSV) of MACC in DME at 25 mV s^{-1} (working electrode: Pt, counter and reference electrode: Mg metal). (b) Voltage responses of Mg//Cu asymmetric cells with MACC in THF at a current density of 0.5 mA cm^{-2}. (c) Mechanism diagram of the MACC electrolyte. [32]

1.3.2 Chloride-free electrolytes

Both Grignard and non-Grignard electrolytes discussed above are chloride-based. While chloride species are essential for enabling reversible Mg plating/stripping chemistry with low overpotentials, the ligand exchange reactions between Mg and Al result in poor oxidation stability. Furthermore, the corrosive nature of chlorides and aluminum chloride pose significant challenges for current collectors and battery casings, rendering these electrolytes unsuitable for high-voltage and long-term MRBs. Consequently, research efforts have shifted toward developing chloride-free, single-salt electrolyte systems that offer low cost, high ionic conductivity, wide electrochemical stability windows, and non-corrosive properties to support

high-energy-density and sustainable energy storage.

The initial development of chloride-free magnesium single salt electrolytes drew inspiration from conventional LIBs systems, employing salts such as $Mg(BF_4)_2$, $Mg(ClO_4)_2$, and $Mg(CF_3SO_3)_2$ salt in polar aprotic solvents (e.g., PC, DMSO, and DMF). These systems presented several advantages over chloride-based electrolytes (**Figure 1.9**), including cost-effectiveness, simplified preparation, improved oxidation stability, and enhanced ionic conductivity. However, their practicality was hindered by poor compatibility with Mg plating/stripping, primarily due to passivation effects induced by solvents, anions, and impurities [24].

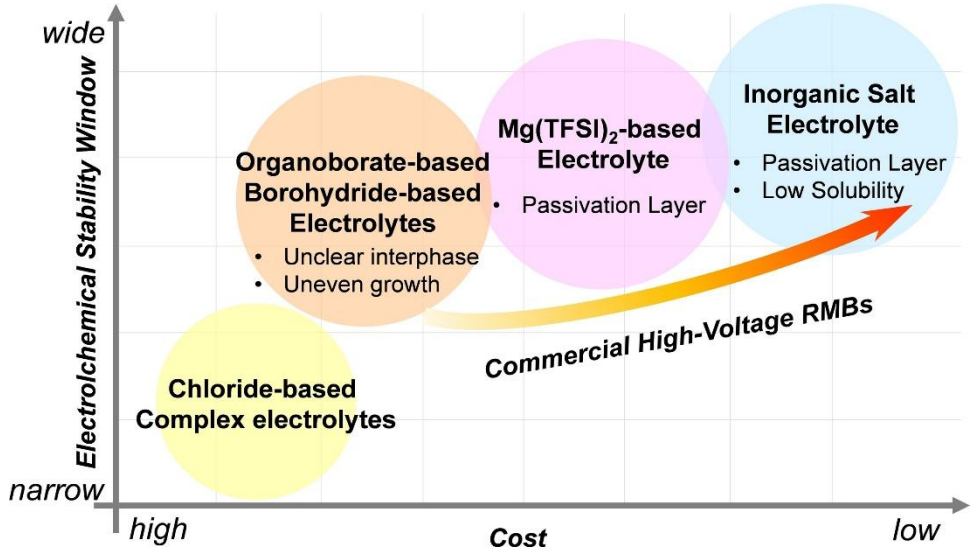

Figure 1.9 Comparison of chloride-free electrolyte systems with chloride-based electrolyte systems. [24]

Early advances in chloride-free electrolytes began with the introduction of the $Mg(BH_4)_2/LiBH_4$ hybrid electrolyte, which achieved a high coulombic efficiency of up to 94% for Mg plating/stripping [33]. Nevertheless, its low oxidative stability (1.7 V) limited its coupling ability to high-voltage cathodes. This work, however, laid the groundwork for further development of chloride-free systems. In 2015, Tutusaus *et al.* [34] synthesized $Mg(CB_{11}H_{12})_2$ salt (MMC), which exhibited improved oxidative stability (> 3.2 V) in single ether solvents (G3 or G4) and delivered over 99% Coulombic efficiency (**Figure 1.10a**). Subsequent

optimization using a DME-G2 co-solvent further enhanced Mg anode kinetics without sacrificing efficiency, enabling dendrite-free Mg plating/stripping at high current densities (**Figure 1.10b** and **1.10c**) [35].

Moreover, Fichtner *et al.* [36] reported $Mg[B(hfip)_4]_2$ based electrolytes, demonstrating high anodic stability (> 4.5 V), superior ionic conductivity (~11 mS cm^{-1}), and low overpotentials in ether-based solvents ((**Figure 1.10d** to **1.10f**). More recently, Lu *et al.* developed a cost-effective cation exchange method using $Zn(BH_4)_2$ to synthesize $Mg[B(hfip)_4]_2$ salt (**Figure 1.10g**), achieving over 99% Coulombic efficiency for Mg plating/stripping [37]. Despite these advances, the commercial application of borohydride and organoborates salts remains limited due to their high cost, complex synthesis, and sensitivity to moisture and impurities.

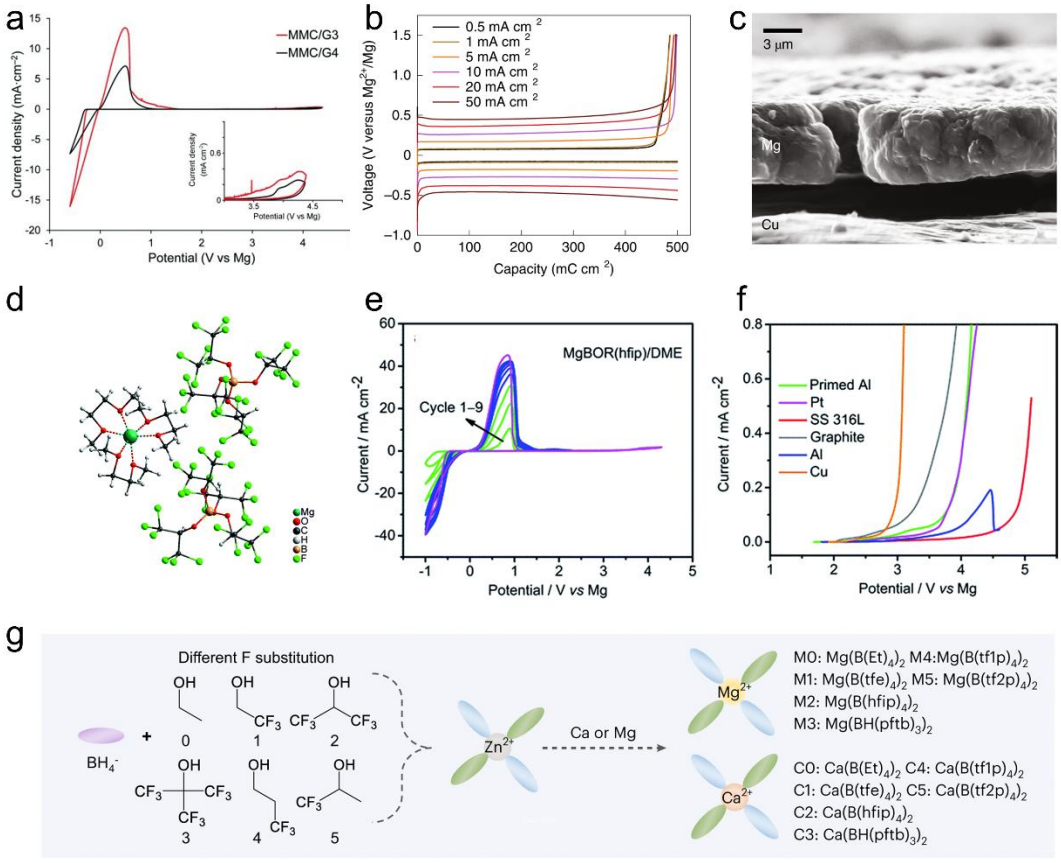

Figure 1.10 (a) CV curves of Mg//Pt asymmetric cell in MMC/G3 and MMC/G4 electrolytes at a scan rate of 5 mV s^{-1}. [34] (b) Polarizations of Mg//Cu asymmetric cell with different current densities and (c) cross-sectional SEM image of Mg plated on Cu substrate at 20 mA

cm^{-2} in MMC/(DME-G2) electrolytes.[35] (d) Ball and stick model of the $Mg[B(hfip)_4]_2$/DME electrolyte.[36] (e) CV curves of Mg//Pt asymmetric cell at a scan rate of 35 mV s^{-1} and (f) LSV of various electrodes in $Mg[B(hfip)_4]_2$/DME electrolyte.[36] (g) Synthesis scheme of Mg solvates based on $Zn(BH_4)_2$ precursor. [37]

Among chloride-free candidates, $Mg(TFSI)_2$ and $Mg(CF_3SO_3)_2$ have emerged as promising options, owing to their commercial availability, high ionic conductivity, and excellent anodic stability (> 3.5 V) [38]. However, in single-salt, single-solvent systems (*e.g.*, $Mg(TFSI)_2$ in DME), their electrochemical performance is suboptimal, characterized by high overpotentials (~2 V *vs.* Mg/Mg^{2+}) even at low current densities and unsatisfactory Coulombic efficiencies (30%~60%). These limitations are attributed to the strong solvation structure of $[Mg(DME)_3]^{2+}$ and the possible decomposition of bulky $TFSI^-$ anions at the Mg metal anode [39, 40], resulting in sluggish ion kinetics during Mg plating/stripping.

To address the limitations of $Mg(TFSI)_2$/DME-based electrolytes, significant research has focused on additive engineering, primarily through the introduction of co-solvents or functional additives. For instance, Wang *et al.* [41] incorporated methoxyethyl-amines-co-solvents with higher Lewis basicity and donor numbers-into $Mg(TFSI)_2$/DME electrolytes (**Figure 1.11a**). This modification enabled efficient Mg plating/stripping with substantially reduced overpotentials in Mg//Mg symmetric cells (**Figure 1.11b**) and achieved high coulombic efficiency of (> 99.5%) in Mg//SS asymmetric cells over approximately 100 cycles (**Figure 1.11c**). Mechanistically, methoxyethyl-amines replace DME in the Mg^{2+} solvation shell, providing stronger chelating sites, which lowers the desolvation energy barrier and suppresses DME decomposition, thereby enhancing interfacial charge transfer at the Mg metal anode.

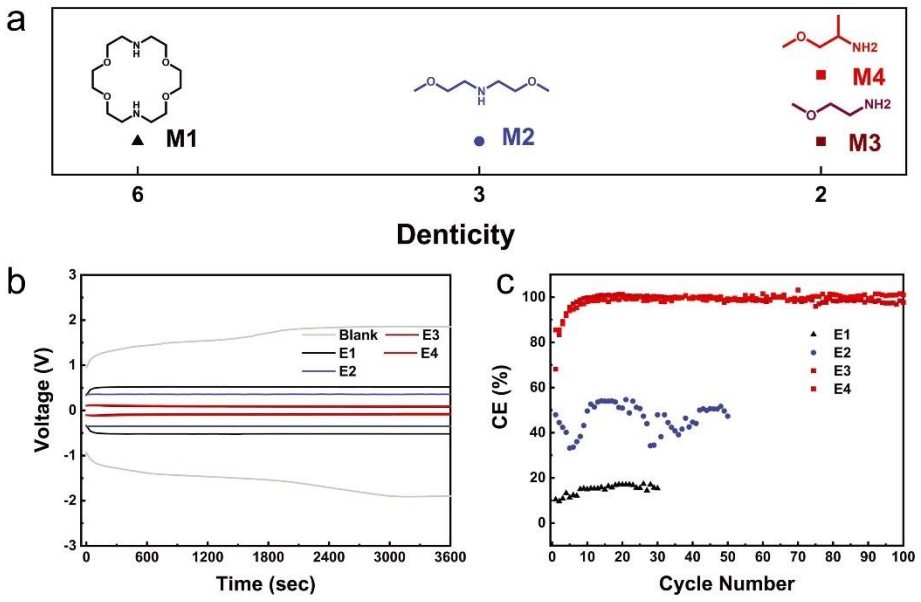

Figure 1.11 (a) The molecular structure and denticity of the methoxyethyl-amines. (b) The overpotentials of Mg||Mg symmetric cells at 0.1 mA cm^{-2} with/out the addition of methoxyethyl-amines. (c) CEs in Mg//SS cells cycled at 0.1 mA cm^{-2} with/out the addition of methoxyethyl-amines. [41]

Similarly, Zhao *et al.* [42] introduced trimethyl phosphate (TMP), a high-dielectric-constant solvent, as an effective additive in $Mg(TFSI)_2$/DME electrolytes. The competition between phosphorus-oxygen groups of TMP and the carbon-oxygen groups of DME modifies the Mg^{2+}-DME dominated solvation structure, mitigating the formation of passivation layers from DME decomposition. As a result, the TMP-containing electrolyte exhibits significantly lower overpotentials (0.15 V) for up to 600 cycles in Mg//Mg symmetric cell at 0.1 mA cm^{-2} (**Figure 1.12a**). SEM images and EIS analyses confirm that TMP addition greatly reduces side-product formation and passivation on the Mg surface (**Figure 1.12b** and **Figure 1.12c**), leading to improved cycling stability.

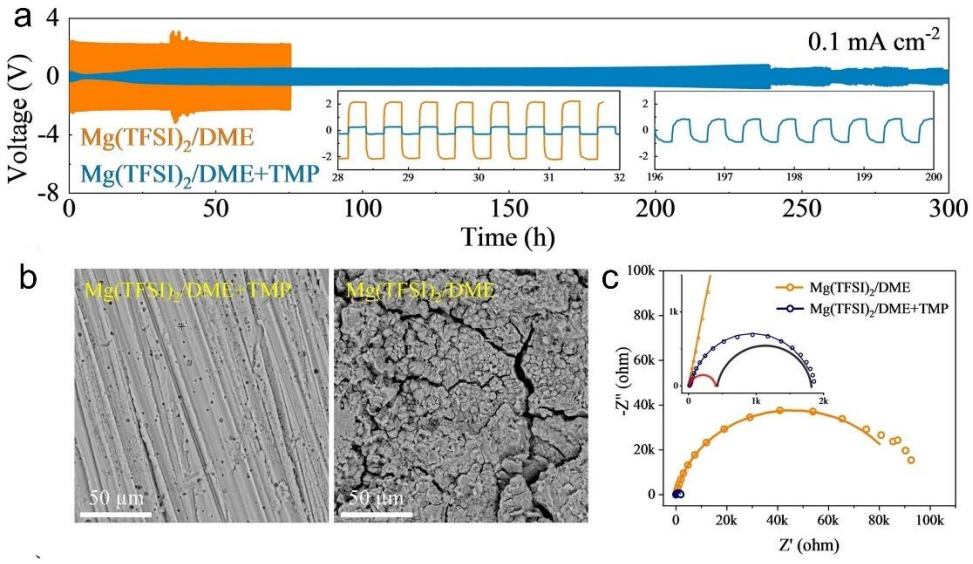

Figure 1.12 (a) Cycling performance of Mg//Mg symmetric cells at 0.1 mA cm^{-2} in $Mg(TFSI)_2$/DME and $Mg(TFSI)_2$/DME+TEP electrolytes, respectively. (b) SEM images and (c) Nyquist plots of cycled Mg anode in $Mg(TFSI)_2$/DME and $Mg(TFSI)_2$/DME+TEP electrolytes, respectively. [42]

Beyond weakening the strong solvation structure of $[Mg(DME)_3]^{2+}$, tailoring the reduction behavior of $TFSI^-$ anions offer another strategy to enhance Mg plating/stripping performance. Li *et al.* [43] developed a comprehensive co-ether phosphate electrolyte (CEPE) system based on $Mg(TFSI)_2$/DME electrolyte, incorporating triethyl phosphate (TEP) to disrupt [Mg^{2+}-$TFSI^-$] cation ion pairs (CIPs) and bis(2,2,2-trifluoroethyl) ether (BTFE) to preferentially adsorb on the Mg surface, thereby suppressing $TFSI^-$ decomposition. These additives effectively reduce $TFSI^-$ reduction, limit passivation layer thickness, and significantly lower overpotentials (**Figure 1.13**). Furthermore, G2 was employed as a co-solvent to further optimize the solvation environment of Mg^{2+}, which aided in their desolvation and supported nanoscale Mg nucleation growth. The optimized CEPE enabled ultra-stable Mg plating/stripping for over 7000 hours at 2 mA cm^{-2} and 2 mAh cm^{-2}. Notably, the CEPE exhibited anodic stability above 4 V, allowing Mg//polyaniline full cells to operate at up to 3.5 V over 400 cycles at 2C with excellent capacity retention.

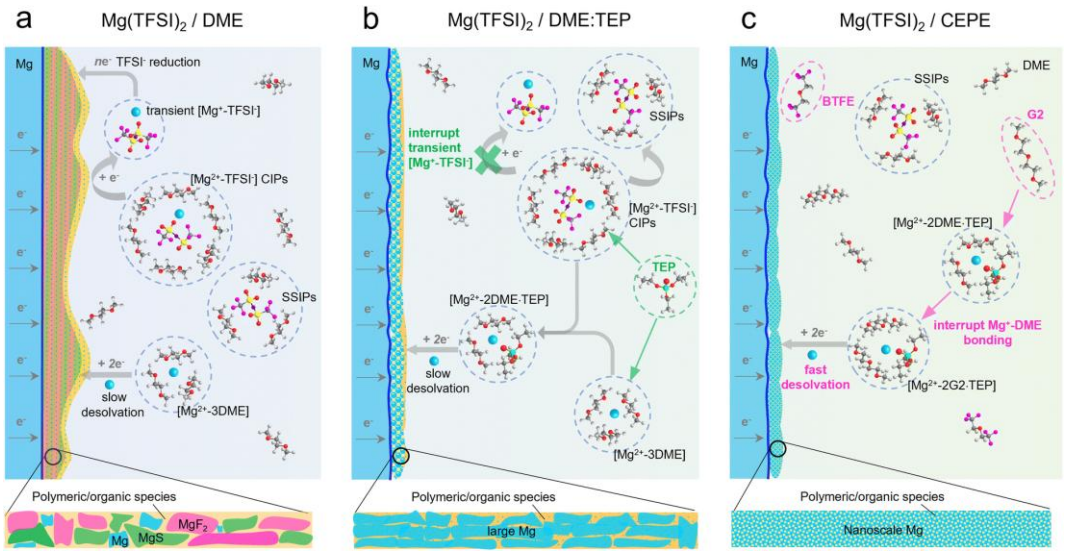

Figure 1.13 Work principle diagram of $Mg(TFSI)_2$/CEPE electrolyte. [43]

Additive engineering has also advanced $Mg(CF_3SO_3)_2$-based electrolytes. NuLi *et al.* [44] introduced 2-methoxyethylamine (MOEA) as a co-solvent in $Mg(CF_3SO_3)_2$/G2 electrolytes. MOEA's integration into the Mg^{2+} solvation structure suppresses the decomposition of G2, reducing passivation on the Mg metal anode. Meanwhile, the preferential decomposition of MOEA forms a beneficial Mg_3N_2-containing interphase, enhancing Mg^{2+} interfacial transport. Consequently, Mg//SS asymmetric cells demonstrated superior cycling stability for 8200 cycles at 0.5 mA cm^{-2} with a Coulombic efficiency of 98.3%. More recently, Nazar *et al.* [45] added TEP to $Mg(CF_3SO_3)_2$/G2 electrolyte to weaken CIPs, resulting in a dynamically bare Mg/electrolyte interface that facilitates complete Mg stripping and plating. This approach achieved an ultra-high plating capacity of (>50 mAh cm^{-2}) in Mg//Cu asymmetric cells, with a Coulombic efficiency of 98.6% and a magnesium utilization rate of 94.3% (**Figure 1.14**).

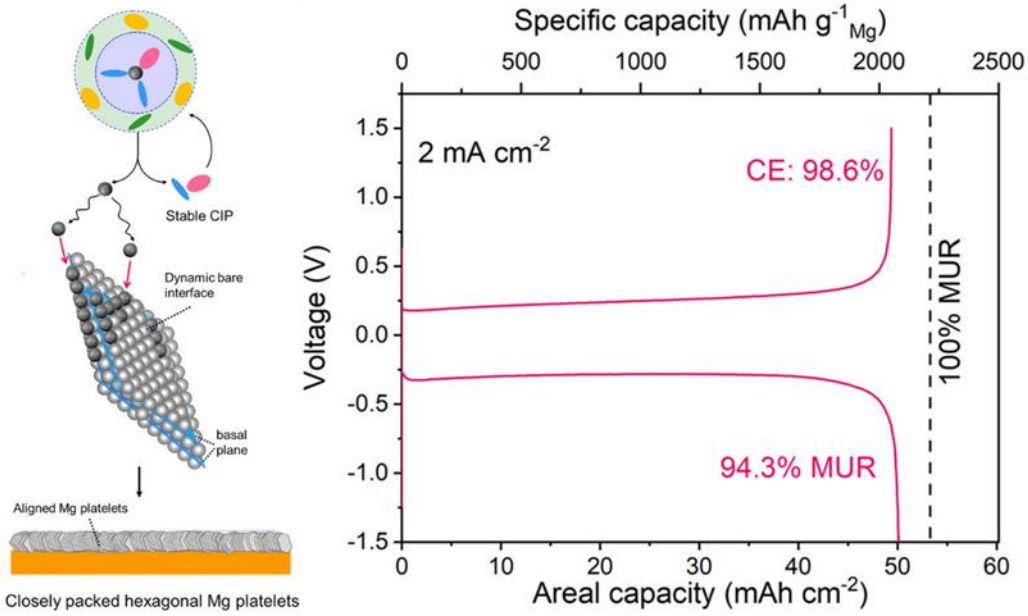

Figure 1.14 Schematic diagram of introducing TEP in $Mg(CF_3SO_3)_2$/G2 electrolyte to weaken CIPs. [45]

1.3.3 Cathode-electrolyte compatibility

So far, significant research efforts have been dedicated to improving the compatibility between electrolytes and Mg metal anode to enhance the efficiency for Mg stripping/plating. However, for high-energy MRBs, efficient Mg^{2+} intercalation chemistry at the cathode is equally critical, necessitating careful consideration of cathode-electrolyte compatibility [19]. Despite this, less attention has been paid to the cathode side, largely due to the scarcity of cathode materials capable of effective and reversible Mg^{2+} storage. Unlike monovalent Li^+ ions, the solid-state diffusion of divalent Mg^{2+} within cathode hosts is inherently more challenging due to its higher charge density and bivalency [46]. While this high charge density enables greater theoretical capacity, it also results in strong Coulombic interactions with anions and solvent molecules in the electrolyte, leading to higher desolvation barriers compared to Li^+. These barriers can promote electrolyte decomposition at the cathode-electrolyte interface (CEI), potentially forming passivation layers that impede Mg^{2+} transport.

Recent studies have demonstrated that Mg^{2+} storage performance varies significantly with cathode type and electrolyte formulation. To date, the Chevrel phase Mo_6S_8 remains the most

prominent cathode, exhibiting high compatibility with both chloride-based and chloride-free electrolytes. This is attributed to its soft, covalent sulfide lattice, which facilitates rapid Mg^{2+} mobility. In chloride-based electrolytes, Mg_xCl_y species promote Mg^{2+} insertion into the Mo_6S_8 host. For instance, Prendergast *et al.* [47] demonstrated that Mo atoms catalytically interact with Cl, reducing the dissociation energy of Mg_xCl_y species on the Mo_6S_8 cathode surface from 3 eV to 0.2 eV, thereby facilitating Mg^{2+} intercalation (**Figure 1.15a**). Subsequently, Aurbach *et al.* [48] proved that a chloride-containing adsorption layer on the cathode surface lowers the activation energy for interfacial charge transfer, enabling efficient Mg^{2+} insertion (**Figure 1.15b**).

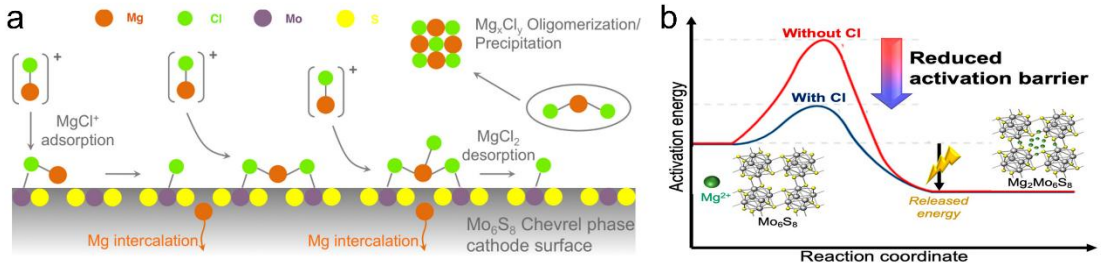

Figure 1.15 (a) Catalytic effect of Mg^{2+} intercalation into Mo_6S_8 in APC electrolyte. [47] (b) Cl^--containing interphase on Mo_6S_8 cathode at CEI in APC electrolyte. [48]

In contrast, the mechanisms governing Mg^{2+} insertion into Mo_6S_8 in chloride-free electrolytes are less well understood due to limited studies. It is generally accepted that Mg^{2+} insertion is hindered in these systems by sluggish diffusion kinetics [19]. Cui *et al.* [49] systematically investigated the interactions between Mo_6S_8 and $Mg[B(hfip)_4]_2$/DME electrolyte, revealing that the anions can be oxidized at appropriate cut-off voltages to form a B_xO_y-rich CEI. This CEI promotes the desolvation of Mg^{2+} at the cathode surface, thereby enhancing interfacial transport kinetics and improving Mg^{2+} storage capacity (**Figure 1.16a**). Similarly, Nuli *et al.* [44] demonstrated that introducing MOEA into $Mg(CF_3SO_3)_2$/G2 electrolyte generates a beneficial CEI containing Mg_3N_2 and C_xN_y complexes, which improves intercalation dynamics and overall electrochemical performance (**Figure 1.16b**).

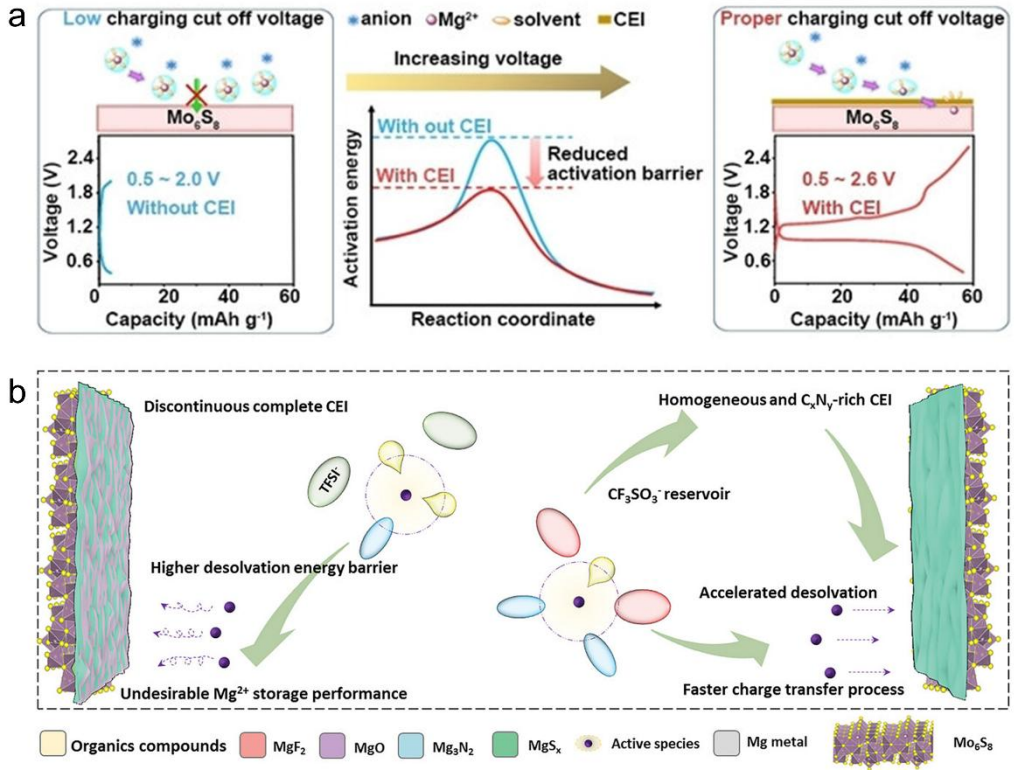

Figure 1.16 (a) CEI chemistry and the corresponding effect on Mo_6S_8 cathode in $Mg[B(hfip)_4]_2$/DME electrolyte. [49] (b) CEI chemistry and the corresponding effect on Mo_6S_8 cathode in $Mg(CF_3SO_3)_2$/ MOEA/G2 electrolyte. [44]

Despite the widespread use of Mo_6S_8, its low capacity (60-80 mAh g^{-1}) and limited voltage output (slightly above 1 V) necessitate the search for higher-capacity and higher-voltage alternatives. Layered oxides and organic compounds have emerged as promising candidates, but they exhibit strong dependence on specific electrolyte formulations, and a universal electrolyte for these cathodes remains elusive. Aurbach *et al.* [38, 50] comprehensively analyzed the failure mechanisms of chloride-free $Mg(TFSI)_2$/DME electrolyte with high-capacity V_2O_5 cathodes, attributing performance limitations to strong Mg^{2+}-DME coordination (**Figure 1.17a**) and $TFSI^-$-induced surface passivation (**Figure 1.17b**). The introduction of cosolvents into $Mg(TFSI)_2$/DME electrolyte has proven effective; Wang *et al.* [41] reported that adding MOEA modifies the strong $[Mg(DME)_3]^{2+}$ coordination to more flexible solvation structure, reducing the reorganization energy required for Mg^{2+} intercalation into layered $Mg_{0.15}MnO_2$ cathodes (**Figure 1.17c**).

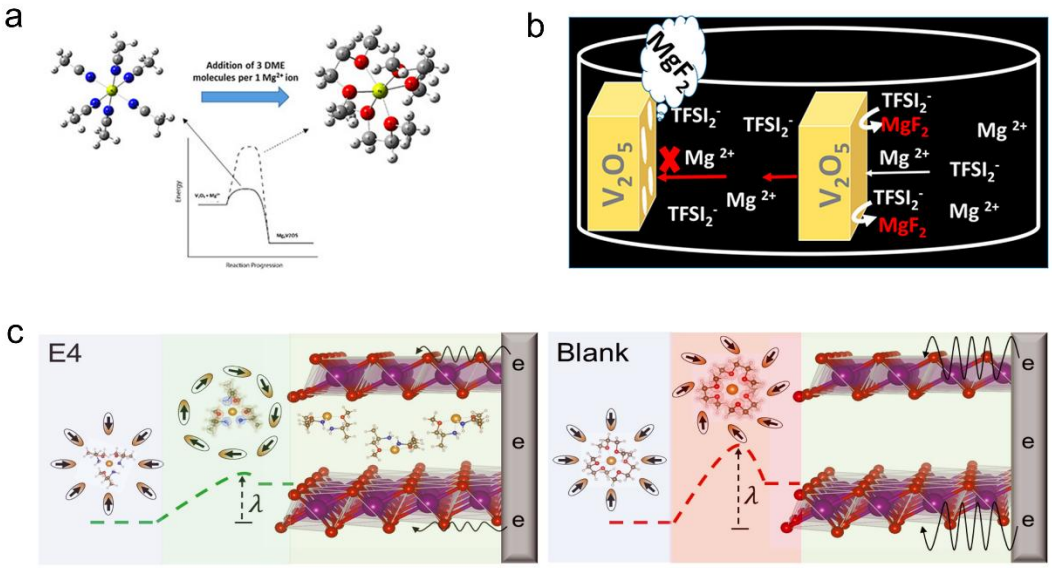

Figure 1.17 (a) Stable Mg^{2+}-DME coordination hinders Mg^{2+} intercalation with cathode host. [38] (b) Partial passivation of $TFSI^-$ anions on V_2O_5 cathode. [50] (c) Reduced intercalation energy by incorporating methoxyethyl-amine into $Mg(TFSI)_2$/DME electrolyte.[41]

For organic cathode, Yao *et al.* [35] identified pyrene-4,5,9,10-tetraone (PTO) as a promising candidate due to its unique heterogeneous enolization redox chemistry, which circumvents the sluggish kinetics associated with bond cleavage and reformation. However, the high viscosity of conventional single-ether electrolytes impedes ionic transport at the CEI, and the dissolution of PTO intermediates in these electrolytes compromises cycling stability (**Figure 1.18**). To address these challenges, a modified $Mg(CB_{11}H_{12})_2$/(DME-G2) co-solvent electrolyte was employed, enabling faster Mg^{2+} diffusion and suppressing the intermediate dissolution, thereby achieving a high specific power of 30.4 kW kg^{-1}.

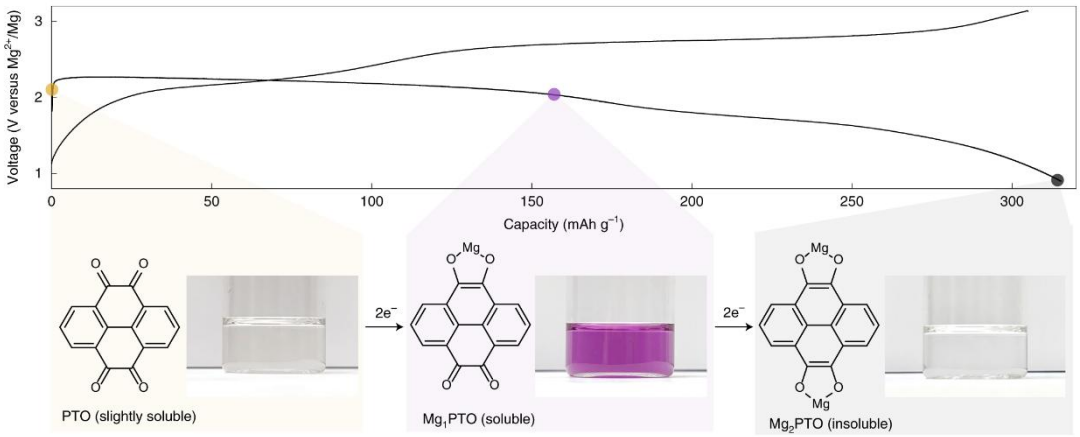

Figure 1.18 The GCD profile of Mg//PTO cell in $Mg(CB_{11}H_{12})_2$/G4 electrolyte with the photographs of electrodes at different discharge states dissolved in DME. [35]

In summary, despite notable progress, research on cathode-electrolyte compatibility in MRBs remains in its early stages, particularly given the diversity of cathode and electrolyte types. Further systematic studies are essential to deepen our understanding of these interactions and to pave the way for the advancement of high-energy MRBs.

1.3.4 Aqueous electrolytes

Since the successful construction of the first MRB prototype in 2000, practical MRBs have yet to be realized. Most reported electrolytes are ether-based organic systems, which enable reversible Mg plating/stripping. However, these electrolytes are flammable and highly sensitive to air and moisture, posing significant safety risks. The high reactivity of Mg metal anodes towards surface reactions restricts the choice of compatible salts and solvents. To advance MRB commercialization and address the growing demand for green and sustainable energy storage, aqueous MRBs, which exhibit high-energy potential in the anode/electrolyte/cathode integration, have recently attracted considerable attention due to their low cost, facile fabrication, enhanced safety, and environmental-friendliness [51].

In this context, the role of water in aqueous electrolytes is being re-evaluated. While water is generally believed to passivate Mg metal, it has beneficial effects on certain high-capacity cathode materials. For example, Novak *et al.* [52] demonstrated that water facilitates Mg^{2+}

insertion into V_2O_5, and subsequent studies have reported similar enhancements for cathodes such as MnO_2, C4Q *etc.* [53] As research progresses on alternative anodes beyond Mg metal, aqueous MRBs are expected to move closer to large-scale application [54]. For instance, Mai *et al.* [55] employed a 1 M $Mg(CH_3COO)_2$ aqueous electrolyte with a VO_2(B) electrode, achieving a high capacity of 257 mAh g^{-1}, excellent cycling stability over 3000 cycles, and 81.5% capacity retention. This performance is attributed to the lower diffusion energy barrier of proton (0.37 eV) compared to hydrated Mg^{2+} ions (2.7 eV). A full pouch cell using VO_2(B)//copper hexacyanoferrate (CuHCF) with this aqueous electrolyte delivered a capacity of 17.6 mAh and an average discharge plateau of 1.1 V. Similarly, Zhang *et al.* [56] utilized 1 M $Mg(TFSI)_2$-H_2O aqueous electrolyte, demonstrating that proton co-insertion significantly enhances Mg^{2+} storage in the organic electrode 3,4,9,10-perylenetetracarboxylic diimide (PTCDI), achieving a specific capacity of 110 mAh g^{-1} at 0.2 A g^{-1}, substantially higher than the 60 mAh g^{-1} obtained with Mg^{2+} insertion alone in an organic electrolyte (1 M $Mg(TFSI)_2$ in EC/PC). These findings underscore the advantages of aqueous electrolytes for MRBs.

Despite these benefits, aqueous MRBs face significant challenges, primarily due to the properties of aqueous electrolytes. The high activity of water limits the ESW to 1.2~1.8 V, mainly due to the hydrogen evolution reaction (HER). Furthermore, excessive proton insertion can compete with Mg^{2+} and induce parasitic side reactions, such as electrode dissolution and decomposition, ultimately degrading battery performance. Rapid proton transport in these systems relies on the Grotthuss mechanism, which is governed by hydrogen bonds networks of free water molecules. Therefore, regulating hydrogen bonding (HB) interactions is crucial to suppress water activity and mitigating side reactions [57].

To address these issues, several strategies have been developed to modulate HB networks and minimize parasitic reactions in aqueous MRBs, including water-in-salt electrolytes (WISEs) [58], hydrated eutectic electrolytes (HEEs) [59, 60], organic/water hybrid electrolytes [54, 61], and solvent-in-water electrolytes (SIWEs) [62]. Among these, HEEs have emerged as particularly

promising. Formed through Lewis acid-base and hydrogen bond interactions, HEEs can effectively suppress free water activity and enable stable battery operation, while also offering low cost, environmental compatibility, and ease of preparation [63, 64]. For example, Alshareef *et al.* [59] utilized a hydrated $Mg(NO_3)_2 \cdot 6H_2O$ salt with acetamide to form a hydrated eutectic electrolyte (**Figure 1.19a**), which suppressed water activity and facilitated Mg^{2+} transport via a three-dimensional HB network. This approach prevents electrode dissolution and enabled stable cycling of a perylene-3,4,9,10-tetracarboxylic dianhydride (PTCDA) electrode for over 1500 cycles at a 10 C rate (**Figure 1.19b**). A full aqueous MRB with a PTCDA anode, CuHCF cathode, and the hydrated eutectic electrolyte achieved an energy density of 52.2 Wh kg^{-1} and an operational voltage of 2.2 V (**Figure 1.19c** and **1.19d**).

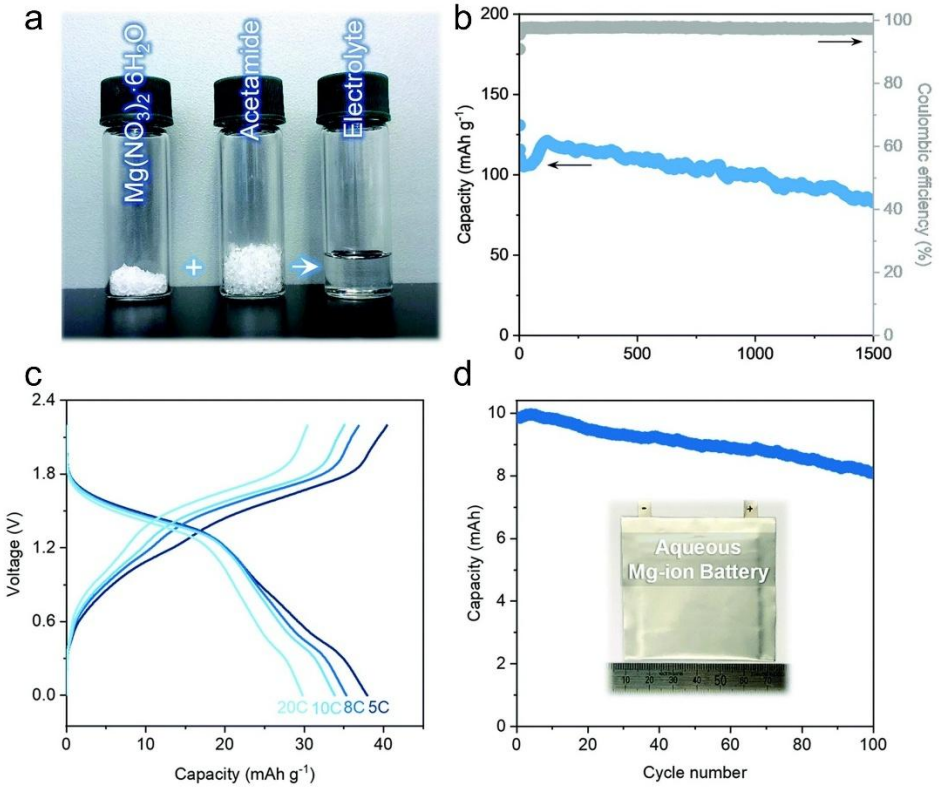

Figure 1.19 (a) Optical photographs of preparing hydrated eutectic electrolytes. (b) Cycling performance of PTCDA anode with the hydrated eutectic electrolyte at 10 C. (c) GCD curves of the full PTCDA//CuHCF AMIB with different current densities. (d) Cycling performance of the pouch type PTCDA//CuHCF AMIB at 5 C. [59]

Subsequently, Jin *et al.* [60] introduced a ternary eutectic electrolyte consisting of $MgCl_2 \cdot 6H_2O$, urea, and acetamide (**Figure 1.20a**). In this system, acetamide competes with urea in the first Mg^{2+} solvation shell, forming an HB network that expands the ESW to 3.5 V. The Mn-NVO electrode with this electrolyte exhibited a high capacity exceeding 190 mAh g^{-1}, attributed to the "breathing effect" at the electrode/electrolyte interface (**Figure 1.20b** to **1.20d**). A full Mn-NVO//CuHCF aqueous MRB with this eutectic electrolyte demonstrated stable cycling over 800 cycles with a specific capacity of ~40 mAh g^{-1} (**Figure 1.20e**). Despite these advances, current HEE systems in aqueous MRBs are largely limited to amide-based eutectics. To further broaden their application, it is essential to develop HEEs beyond amide systems and to achieve a comprehensive understanding of the electrode-electrolyte interface. Such insights will guide the rational design of next-generation electrolytes for practical MRBs implementation.

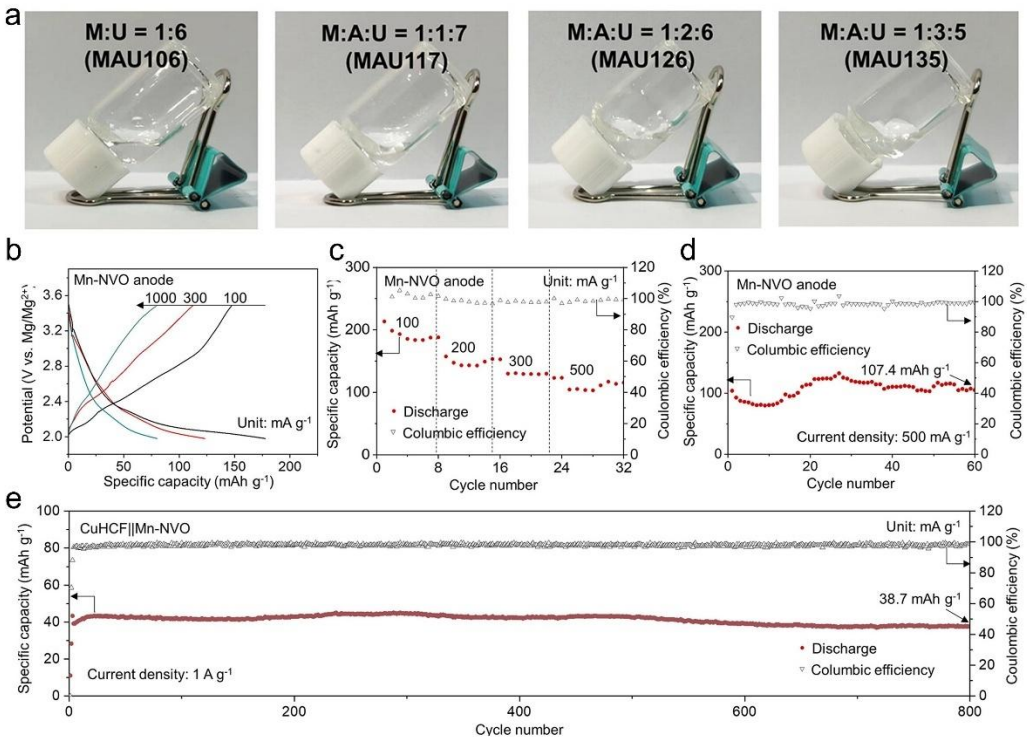

Figure 1.20 (a) Optical photographs of the prepared eutectic electrolytes. (b) GCD curves at various current densities, (c) rate performance, and (d) cycling performance of Mn-NVO anode in the MAU117 eutectic electrolyte. (e) Cycling performance of a full Mn-

NVO//CuHCF AMIB in the MAU117 eutectic electrolyte. [60]

1.3.5 Solid-state electrolytes

In addition to aqueous electrolytes, solid-state electrolytes are emerging as promising candidates for safe and high-energy MRBs due to their inherent nonflammability, non-volatility, excellent thermal stability, and mechanical flexibility [65]. Notably, the use of solid-state electrolytes can completely eliminate safety concerns associated with liquid electrolyte leakage in practical batteries systems. Among various types, polymer-based solid-state electrolytes are the most widely reported, attributed to their cost-effectiveness and robust mechanical stability [66]. However, their relatively ionic conductivity remains a significant barrier to achieving high-performance requirements. Strategies such as incorporating nanofillers or blending different polymers have shown some improvements in electrochemical performance and stability [67, 68], yet these approaches still fall short of meeting practical application requirements. Overall, the low ionic conductivity and high interfacial impedance of current solid-state electrolytes result in inferior performance compared to liquid electrolytes, thereby limiting their further development. Consequently, there is an urgent need to design new solid-state electrolyte systems with enhanced ionic conductivity and improved electrode-electrolyte compatibility for practical MRBs utilizations.

1.4 Objectives and outline

MRBs are considered promising candidates for next-generation EES beyond LIBs. However, the lack of suitable electrolytes compatible with both high-capacity cathodes and anodes remains a major obstacle to their practical deployment. Although several electrolyte systems, such as APC and MACC, have been developed to enable reversible Mg stripping/plating, issues including toxicity, corrosion of current collectors and battery casings, and limited oxidative stability hinder their sustainability and energy density. Chloride-free electrolytes, offering greater cost-effectiveness, higher electrochemical stability, and improved environmental compatibility, represent a viable alternative. Nevertheless, their sluggish Mg^{2+} kinetics and

passivation tendencies impede efficient reversible Mg deposition. Therefore, optimizing existing chloride-free electrolytes or developing novel electrolyte systems is critical for advancing sustainable and high-performance MRBs. This thesis focuses on the optimization of chloride-free electrolytes and exploration of new electrolyte systems for MRBs, and the objectives are as follows:

(1) To optimize existing magnesium electrolytes through the incorporation of suitable additives or solvents, or by developing novel electrolyte systems, in order to achieve enhanced ionic conductivity and high electrochemical stability. These improvements aim to ensure better compatibility with both high-performance cathodes and anodes, thereby enabling superior electrochemical performance in MRBs.

(2) To elucidate the chemical structures of the developed electrolytes, providing a fundamental understanding of their behavior.

(3) To investigate the mechanisms governing electrode-electrolyte interactions, thereby deepening insights into factors influencing battery performance.

(4) To assemble full batteries to evaluate the practical applicability of the developed electrolytes.

By developing new electrolytes, systematically studying their chemical structures and electrode-electrolyte interaction mechanisms, and assessing their practical applications, this work aims to provide comprehensive insights and actionable guidance for future research in MRBs. The thesis contents are listed as follows:

Chapter 1: This chapter briefly introduces the background and challenges of MRBs, especially focusing on systematically describing and analyzing the electrolyte systems developed so far in MRBs.

Chapter 2: This chapter summarizes the experimental methods and related reagents used in this thesis.

Chapter 3: This chapter presents a novel eutectic solid-state electrolyte by directly crystallizing the $Mg(TFSI)_2$/urea liquid mixture at room temperature to realize reversible Mg

stripping/plating.

Chapter 4: This chapter describes a new glycol-glyme co-solvent electrolyte, which exhibits high compatibility with both high-performance VO_2 cathode and Mg metal anode.

Chapter 5: This chapter describes a new sulfone-based hydrated eutectic electrolyte for magnesium ion batteries, which could suppress water activity and inhibit cathode dissolution to realize better capacity output and longer cycling stability.

Chapter 6: This section summarizes the series work on the developed electrolytes and proposes future directions for further exploration of magnesium electrolytes.

Chapter 2 Experimental methods

This chapter describes the main chemicals and reagents used in the experiments. It also outlines the experimental procedures, including materials preparation, characterization methods, device assembly, electrochemical measurements, and theoretical simulations.

2.1 Chemicals and reagents

All chemicals were used as received without further purification, and relevant details are provided in **Table 2.1**.

Table 2.1 Chemistry and reagents required for the experiment.

Chemical	Abbreviation	Specifications	Manufacturer
Magnesium(II)Bis(trifluoromethane sulfonyl)imide	$Mg(TFSI)_2$	AR	Aladdin
Magnesium perchlorate hexahydrate	$Mg(ClO_4)_2 \cdot 6H_2O$	AR	Aladdin
Propylene carbonate	PC	AR	Aladdin
1,2-dimethoxyethane	DME	AR	Sigma-Aldrich
Ethylene glycol	EG	AR	Aladdin
1-Methyl-2-pyrrolidinone	NMP	AR	Aladdin
Acetamide	ACE	AR	Aladdin
N-Methylacetamide	NMAc	AR	Aladdin
Urea	Urea	AR	Aladdin
Sulfolane	SL	AR	Aladdin
Tetrahydrofuran	THF	AR	Aladdin
Anhydrous acetonitrile	ACN	AR	Aladdin
Vanadium (V) oxide	V_2O_5	AR	Aladdin
3,4,9,10-Perylenetetracarboxylic dianhydride	PTCDA	AR	Aladdin
Activated carbon	AC	AR	Aladdin
Super P	Super P	AR	Aladdin
Polyvinylidene fluoride	PVDF	AR	Aladdin

2.2 Material preparation

2.2.1 Electrolytes preparation

Mg^{2+}-conducting solid-state electrolytes (MCEs): MCEs were prepared by simple magnetic stirring and naturally cooling processes. In detail, homogenous liquid solutions were prepared by steadily stirring $Mg(TFSI)_2$ and urea mixtures with different molar ratios ($n_{Mg(TFSI)2}$: n_{urea} =1:2, 1:4, 1:6, 1:8, and 1:12) at 80 ℃ for 24 hours. When the liquid samples cooled down to room temperature, waxy-like solid state electrolytes were obtained. 0.5 M $Mg(TFSI)_2$/PC was synthesized as the control electrolyte. All these electrolytes were synthesized in an Ar-filled glove box.

Glycol-glyme co-solvent electrolytes: The co-solvent electrolytes were prepared by stirring 0.5 M $Mg(TFSI)_2$ in EG/DME solvents with different volume ratios (v_{EG} = 0 %, 25%, 50%, 75%, and 100%, respectively) for more than 6 h. 0.5 M $Mg(TFSI)_2$/DME was prepared as the control electrolyte. All these electrolytes were prepared in an Ar-filled glove box.

Hydrated eutectic electrolytes (HEEs): HEEs were prepared by stirring hydrated $Mg(ClO_4)_2 \cdot 6H_2O$ salt in SL at various molar ratios ($Mg(ClO_4)_2 \cdot 6H_2O$: SL = 1:4, 1:6, 1:8, and 1:10) for over 3 h. Control electrolytes of 1 M $Mg(ClO_4)_2/H_2O$ and $Mg(ClO_4)_2$/SL (1:8) were also prepared.

2.2.2 Electrodes preparation

Preparation of VO_2 cathode: The VO_2 nanorods was synthesized according to the previous report [69]. Typically, 1 g V_2O_5 powder and 12 ml EG were added to 18 mL deionized water and was vigorously stirred at room temperature for 2 hours. The suspension was then transferred into a 100 mL Teflon-lined autoclave for hydrothermal reactions at 180 ˚C for 5 hours. The dark green products were finally collected by centrifugation and washed with deionized water and absolute ethanol several times. The final product was then dried in a vacuum oven at 80 ˚C for 12 hours. The VO_2 electrode slurry was prepared by mixing the as-synthesized VO_2, super P and PVDF at a weight ratio of 7:2:1 in NMP and cast onto carbon coated Al foil. The electrode

was dried overnight in a vacuum oven at 70 ℃, with an active material loading of approximately 0.5 mg cm^{-2}.

Preparation of V_2O_5 cathode: The V_2O_5 electrode was synthesized via a hydrothermal method [61, 70]. Typically, 0.546 g V_2O_5 powder was dissolved in 24 ml deionized water for 30 minutes. Then, 6 ml H_2O_2 were added to the yellow suspension until a reddish-brown solution formed. The solution was transferred to a 50 mL Teflon-lined autoclave for hydrothermal reaction at 200 ˚C for 48 hours. After cooling to room temperature naturally, the samples were collected by centrifugation and washed several times with deionized water and absolute ethanol. The samples were dried in a vacuum oven at 60 ˚C for 12 hours. The V_2O_5 electrode slurry was prepared by mixing the synthesized V_2O_5, Super P and PVDF in a weight ratio of 7:2:1 in NMP, and casting onto stainless steel foil. The electrode was then dried overnight in a vacuum oven at 60 ℃, with an active material loading of approximately 1 mg cm^{-2}.

Preparation of Mg metal anode: Magnesium foil, with a thickness of 0.1 mm, was polished using sandpaper and then cut into discs with a diameter of 10 mm inside a glove box for cell assembly.

Preparation of PTCDA anode: PTCDA anode was prepared by grinding PTCDA powder, Super P, and PVDF in a weight ratio of 8:1:1 using NMP as the solvent. This mixture was then formed into a uniform slurry, coated evenly onto Ti foil, and dried overnight under vacuum.

2.3 Characterization methods

Differential Scanning Calorimeter (DSC): DSC (Netzsch DSC 200 F3) was used to determine the freezing and melting point of the electrolytes. This thermoanalytical technology measures enthalpy changes during transitions and reactions as a function of temperature. The measured melting point can be used to assess the suitability of electrolytes for applications in harsh environments, such as low temperatures.

*Thermogravimetric analysis (TGA)***:** TGA (TA Q500) was utilized to assess the thermal stability of the electrolytes. It continuously measures the mass change of a sample as the temperature

changes, providing information on phase transitions and thermal decomposition.

*Fourier-transform infrared (FTIR)***:** FTIR (Thermo Fisher Scientific Nicolet iN10) was used to observe changes in the chemical bonds and structure of the electrolytes. In this technique, infrared radiation passes through the sample, inducing molecular vibrations and resulting in the adsorption of characteristic frequencies. Consequently, high-resolution spectral data over a wide range can be obtained to identify functional groups and changes in chemical bonds within the sample.

Raman microscopy: Raman microscopy (Horiba LabRAM HR Evolution) equipped with a 532 nm laser was utilized to investigate the crystal structure and molecular vibrations of the samples. Specifically, Raman spectroscopy of electrolytes can identify changes in the solvation environment of Mg^{2+} in bulky electrolytes.

Nuclear magnetic resonance (NMR): ^{13}C and ^{1}H liquid NMR (Bruker Avance NEO 400MHz) was used to examine the chemical environment of carbon and hydrogen in the electrolytes, contributing to both qualitative and quantitative analysis of their chemical structure. When exposed to an applied magnetic field, certain atomic nuclei absorb energy from a radio frequency field at characteristic frequencies, producing distinct NMR signals. The chemical shift offset intuitively reflects the strength of the interactions between chemical bonds.

X-ray diffraction analysis (XRD): XRD (Rigaku SmartLab 9 kW diffractometer with Cu-Kα radiation) was used to identify the phase structure of electrode materials and chemical composition of the solid electrolyte interphase (SEI). Rietveld refinement was carried out using the GSAS program. In-situ XRD experiments were conducted using a custom cell with an X-ray transparent beryllium (Be) window to observe the electrode phase changes during the charging/discharging process.

Scanning Electron Microscope (SEM): SEM (Tescan MIRA, Tescan MAIA3, Tescan VEGA3) was used to observe the morphology of the prepared samples. As a non-destructive characterization technique, SEM uses electrons that interact with atoms in the sample to

produce signals reflecting the materials morphology and composition characteristics.

Transmission Electron Microscope (TEM) and High-resolution TEM (HRTEM): TEM and HRTEM (JEOL JEM-F200 and JEOL 2100) was utilized to analyze the nanostructure of the prepared materials. The material was ultrasonically dispersed in ethanol multiple times and subsequently dropped onto copper grids coated with carbon membranes. The electron beams in TEM and HRTEM can focus on a very small size scale, allowing detailed information such as lattice defects and grain size to be obtained.

X-ray Photoelectron Spectroscopy (XPS): XPS (Thermo Scientific Nexsa) is utilized to identify the chemical composition and electronic states on the surface of the electrode materials. This quantitative method operates on the principle of the photoelectric effect. When the sample is exposed to a high-energy X-ray beam, surface photoelectrons are emitted and captured, providing chemical information such as chemical structure, oxidation state and electronic state.

Time-of-Flight Secondary Ion Mass Spectrometry (TOF-SIMS): TOF-SIMS (TOF-SIMS 5 iontof) was employed for in-depth analysis of the chemical distribution on the surface of electrode materials at the nanoscale. In TOF-SIMS, a pulsed ion beam removes molecules from the outermost layer of the surface, and the collected molecules are accelerated into flight tube to determine their mass based on their specific arrival times. Compared with other technology, TOF-SIMS offers high spatial resolution and advanced capabilities like depth profiling and 3D analysis, making it a powerful method for surface analysis.

2.4 Electrochemical measurement

2.4.1 Battery Assembly

All batteries were assembled in CR2032-type coin cells, with glass fiber membranes serving as separators.

For the Mg^{2+}-conducting solid-state electrolytes (MCEs) system: three types of cells were constructed. The Mg//Mg symmetric cell used Mg metal as both the cathode and anode with the MCEs. The Mg//SS asymmetric cell featured SS as the cathode and Mg metal as the anode

with the MCEs. Mg//V_2O_5 full cell was assembled with the as-prepared V_2O_5 as the cathode and Mg metal as the anode, incorporating MCEs.

For the glycol-glyme co-solvent electrolytes system: Two main types of cells were constructed. Mg ion half cells were assembled using the as-prepared VO_2 as cathode and AC on carbon cloth as the counter electrode, with co-solvent electrolytes. Mg//VO_2 full cells were assembled in a glovebox using the as-prepared VO_2 cathodes, Mg metal anodes, and the co-solvent electrolytes.

For the HEEs: Mg ion half cells were assembled using the prepared V_2O_5 as cathode and AC on carbon cloth as the counter electrode, with HEEs. PTCDA//V_2O_5 full cells were assembled utilizing the prepared V_2O_5 cathodes, PTCDA anodes, with HEEs in air.

2.4.2 Electrochemical characterization

Typical electrochemical tests like electrochemical impedance spectroscopy (EIS), cyclic voltammetry (CV), and linear sweep voltammetry (LSV) were carried on a CHI 660E and Biological-Logic VSP-3 electrochemical workstation. Electrochemical charge/discharge profiles, rate performance, and the Galvanostatic intermittent titration technique (GITT) measurements were recorded with a Neware CT-4008 battery tester.

2.5 Theoretical calculation

Quantum chemistry calculations were carried out with the Gaussian 16 software. The geometries of molecules were optimized using the B3LYP exchange-correlation functional in conjunction with the basis set of 6-311++G (d, p) under the gas phase approximation. All of the optimized structures were confirmed as potential minima, with no frequency modes with imaginary eigenvalues, through frequency analyses following geometry optimizations. The LUMO and HUMO orbital energy levels and electrostatic potential (ESP) were analyzed by using Multiwfn software [71] and visualized by using VMD software.

Molecular dynamics (MD) simulations were conducted using the Gromacs 2022 software. General Amber force fields (GAFF) parameters of the EG and DME molecules, Mg^{2+} and $TFSI^-$ were obtained by Sobtop program (Tian Lu, Sobtop, Version 1.0,

http://sobereva.com/soft/Sobtop, accessed on octomber 31, 2023). RESP2(0.5) charge for all solvent molecules and anions was defined by Multiwfn software. Particularly, a scaling factor of 0.8 was employed for Mg^{2+} and anions charge owing to the charge transfer effect. The initial size of the simulation box is 40×40×40 Å3. After the energy minimization, the systems were initially heated from 0 K to 350 K during 3.5 ns and relaxed at 350 K for 5 ns. Next, the systems were annealed to 300 K at 0.5 K ps−1 and remained at 300 K for 2 ns. All these annealing processes were simulated by NPT ensemble utilizing Berendsen barostat for modulating the pressure. Finally, the systems were simulated in NVT ensemble regulated by Velocity-rescale for 10 ns and the last 5 ns trajectories were utilized to analyze local coordination structure of Mg^{2+}.

Chapter 3 Direct crystallization of deep eutectic solvents into solid-state electrolytes for magnesium metal batteries

3.1 Introduction

The ever increasing demands of portable devices and vehicle electrification have stimulated intense desire on energy dense and safe solid-state rechargeable batteries [72]. To date, the research on solid-state rechargeable battery has been mainly focused on lithium batteries due to the well-established Li-ion chemistry and the availability of a handful of Li-ion solid state electrolytes (SSEs) [73, 74]. Concerns rising from the unsustainable supply of Li feedstock and the uncontrollable Li dendrite generation have triggered explorations on new battery systems using more abundant element as charge carriers [9, 10]. Among the many options, solid-state magnesium rechargeable batteries (SSMRBs) are considered promising owing to the low cost and high abundance of Mg element (2.33 wt% *vs.* 0.0002 wt% for Li), the superior physical stability (melting point of 648.9 °C for Mg metal *vs.* 180.5 °C for Li metal) and a higher volumetric capacity (3833 mAh cm^{-3} for Mg metal *vs.* 2062 mAh cm^{-3} for Li metal) [75-77]. In addition, Mg metal anode earned the reputation of non-dendritic plating/stripping processes [78-82]. Nevertheless, solid-state electrolytes with rapid Mg^{2+} transportation are lacking.

The research on Mg-ion solid-state electrolyte is mainly focused on gel polymer electrolytes (GPEs) by mixing polymeric matrices like polyethylene oxide (PEO) [65], polyvinylidene fluoride (PVDF) [83], and poly(vinylidene fluoride-co-hexafluoropropylene) (PVDF-HFP) [84] with Mg salts (*i.e.,* $Mg(ClO_4)_2$, $Mg(CF_3SO_3)_2$, $Mg(AlCl_2EtBu)_2$) in ethylene carbonate (EC) or propylene carbonate (PC) solvents [85-87]. Although considerable ionic conductivities were reported for GPEs, the highly corrosive chloride-based salt (*i.e.,* Mg organohaloaluminates) [88], the Mg-ion blocking interphase (*i.e.,* Mg halides formed by reacting with $Mg(ClO_4)_2$), and the flammable organic solvents impede the development of safe SSMRBs [59, 89]. In addition, the side reactions between GPEs and Mg metal can cause irreversible Mg metal electrodes reaction [25]. The irreversibility was mainly caused by the ion-blocking solid

electrolyte interphase (SEI). [68, 90, 91] To be specific, for $Mg(ClO_4)_2$ or $Mg(CF_3SO_3)_2$-based electrolytes, the ClO_4^- and $CF_3SO_3^-$ anions would react with Mg metal to generate insoluble and ionic insulating Mg halides/salts [88, 92]. For the magnesium organohaloaluminates-based (*i.e.,* APC) electrolyte, the corrosion of current collectors by chloride-containing species is highly detrimental [93]. In addition, the strong binding energies between polymer skeletons and Mg^{2+} induced poor ionic conductivity and low transference number, which further retarded the Mg deposition kinetics.[94] Hence, new electrolyte formulations with appreciable safety and compatibility are eagerly awaited to promote the development of SSMRBs.

Recently, an intriguing approach of directly crystalizing liquid electrolytes into solid phase at room temperature (RT) was proposed [95, 96]. The solid-state ionic conducting ices (*i.e.,* freezing Li^+, Mg^{2+} and Zn^{2+} sulphate solutions at RT) indicated notable ionic conductivities, which are attributed to the full salt dissociation and the elevated ion-carrier densities [97, 98]. Compared with the procedures of fabricating ceramic pellets (*i.e.,* $MgPS_3$-MgI_2 [99]) and GPE solid state electrolytes, this strategy is considerably simple and effective. Deep eutectic solvents (DESs), which only consist of metal salts and amide-based ligands, is a promising approach to realize this strategy. Different from the traditional liquid electrolyte with abundant organic solvents, the DES could utilize widely accessible and green chemicals to associate biphasic solution formation via hydrogen bonds. In addition, DESs intrinsically possess superior ionic liquid-like properties, such as low vapor pressure, high ionic conductivity, excellent electrochemical stability, and highly flammable resistance [87, 100]. By directly adjusting molar ratios of metal salts (*i.e.,* $Zn(CF_3SO_3)_2$) and amide-based ligands (*i.e.,* acetamide), high-entropy DESs were solidified for Zn-ion batteries at RT [101]. The direct crystallization of Mg ion DES holds promises for developing high-performance SSMRBs, an avenue yet to be explored.

Herein, for the first time, we reported a Mg^{2+}-conducting solid state electrolyte (MCE) by directly crystalizing the $Mg(TFSI)_2$: urea (molar ratio = 1: 8) DES structure at room temperature for SSMRBs. The copious amine and carbonyl groups in urea ligands tailored the

intermolecular frameworks with $Mg(TFSI)_2$, thereby creating anion-rich groups in the Mg^{2+} solvation sheath. This structure can alleviate surface passivation from solvent decomposition as observed in liquid electrolytes, *i.e.*, $Mg(TFSI)_2$/PC. The Mg//Mg solid-state symmetric cells made from the MCE demonstrated an appreciable cycle life of more than 120 h at 25 μA cm^{-2}. The improved electrochemical performance is attributed to the F-rich and porous organic/inorganic hybrid interface layer, which effectively activated Mg metal and facilitated rapid Mg^{2+} transportation through the interface. Finally, solid-state Mg//V_2O_5 full cells were built to verify the practical feasibility of MCE, which exhibited a high capacity of 172 mAh g^{-1} at 20 mA g^{-1}. This work is expected to pave a new way towards developing novel MCEs for safe SSMRBs.

3.2 Results and discussion

3.2.1 Key properties of the Mg^{2+} conducting solid-state electrolyte

The preparation and characterization of the MCE are shown in **Figure 3.1a**. Homogenous liquid solutions were prepared by steadily stirring $Mg(TFSI)_2$ and urea mixtures with different molar ratios ($n_{Mg(TFSI)2}$: n_{urea} =1:2, 1:4, 1:8, and 1:12) at 80 ℃ for 24 h. When the liquid samples cooled down to room temperature, waxy-like solid state electrolytes were obtained.

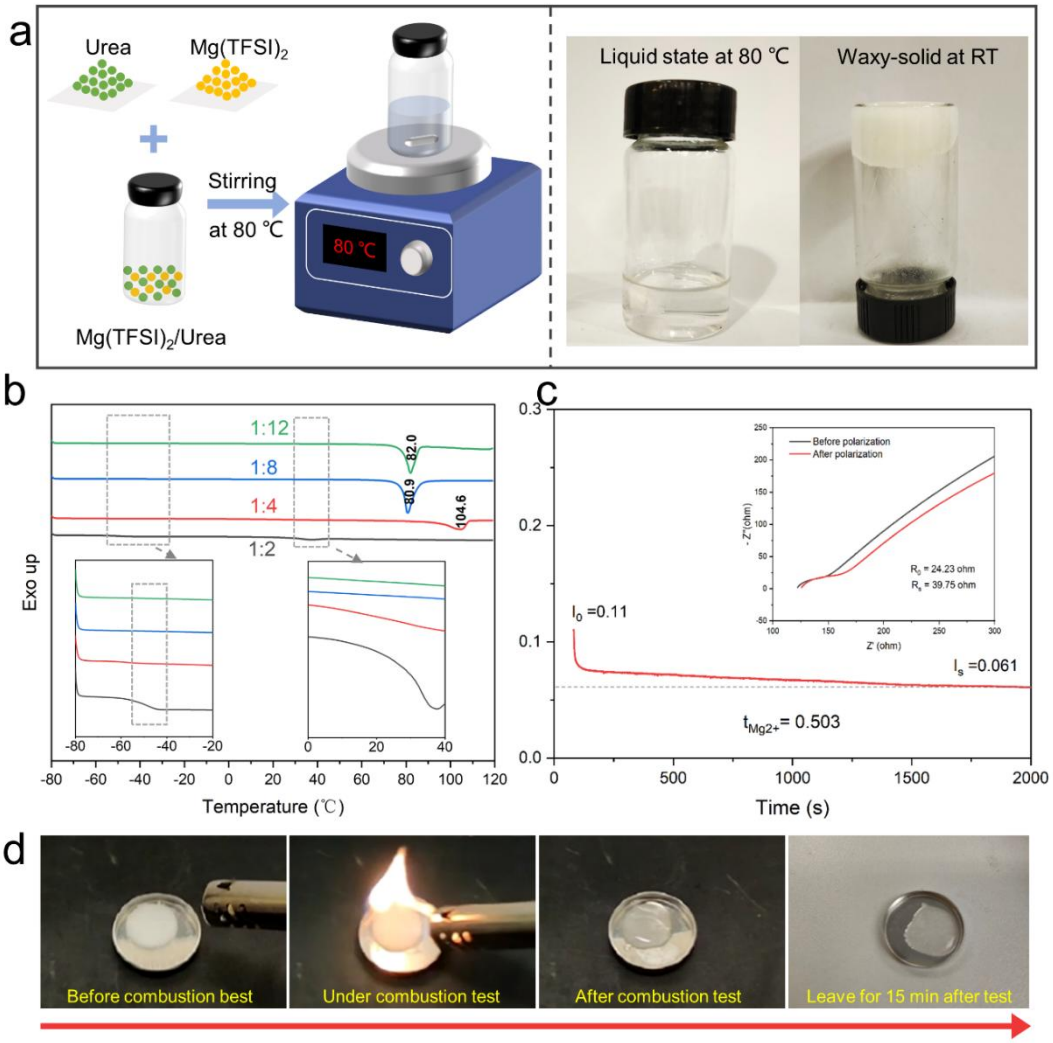

Figure 3.1 (a) The preparation diagram for MCE. (b) DSC profiles of the $Mg(TFSI)_2$/urea electrolytes with different molar ratios. (c) Direct current polarization curve of Mg//Mg symmetric cells with MCE under an overpotential of 5 mV, inset showing the Nyquist plots before and after the polarization tests. (d) Flammability test of MCE.

DSC was conducted to examine the thermal property of these electrolytes (**Figure 3.1b**). In solid or liquid electrolytes, there will be only one peak corresponding to the melting point. In contrast, the melting of a eutectic binary mixture starts at the eutectic temperature and follows with a second melting process for the remaining solid or liquid compositions [97, 98]. For MCE of $n_{Mg(TFSI)2}$: n_{urea} = 1:2, the eutectic temperature is around -50.5 ℃ and a melting temperature is at approximate 40 ℃. These values are much lower than the melting temperatures of their individual components (*i.e.*, ~133 ℃ for urea and >200 ℃ for $Mg(TFSI)_2$ salt). Therefore, we

speculated that the $n_{Mg(TFSI)2}$: n_{urea} = 1:2 is close to the eutectic point. With the increase of urea content in MCEs, the eutectic feature is steadily weakened (as shown in the dashed box of **Figure 3.1b**). For MCEs of $n_{Mg(TFSI)2}$: n_{urea} ≥1:4, MCE can be completely solidified at room temperature, with melting temperatures ranging from 80.9 to 104.6 ℃. The disappearance of the eutectic point would not affect the high degree of chaos in the ionic conductive solid-state electrolytes, which are expected to form local ion percolating networks. By comparing the cyclic performance of Mg metal in these electrolytes at room temperature (**Figure 3.2** and **3.7a**), the $n_{Mg(TFSI)2}$: n_{urea} =1:8 with well-balanced physical and electrochemical performance was selected as the optimal MCE for the following experiments.

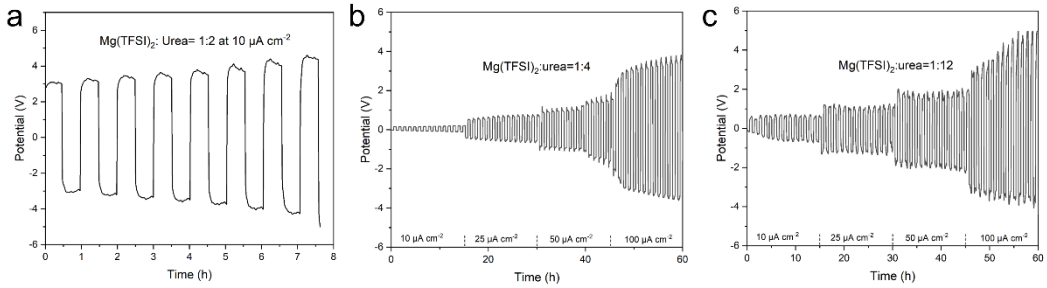

Figure 3.2 Voltage responses of Mg//Mg symmetric cells with MCEs at different molar ratios cycling from 10 μA cm^{-2} to 100 μA cm^{-2}.

The electrochemical window of the MCE was examined by using a stainless-steel (SS) working electrode and Mg metal as the reference/counter electrode at room temperature. The MCE exhibited (**Figure 3.3a**) a competitive stability of ~2.7 V *vs.* Mg/Mg^{2+}, surpassing the traditional Grignard reagent (~1.3 V) by more than two times [102]. The ionic conductivity of MCE was calculated to be 1.47×10^{-3} S cm^{-1} at room temperature by EIS measurements. By increasing the temperature, the ionic conductivity could be improved to 3.43 $\times10^{-3}$ S cm^{-1} at 70 ℃ (below the melting temperature, **Figure 3.3b**), surpassing the reported values for GPEs (**Table 3.1**).

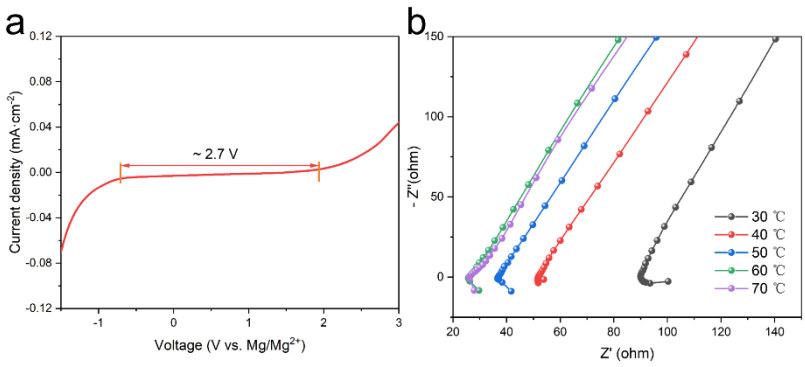

Figure 3.3 (a) LSV profile of SS working electrode in eutectic $Mg(TFSI)_2$/Urea electrolyte, using Mg as the reference at a scan rate of 2 mV s^{-1}. (b) Nyquist plots of the MCE sandwiched between two stainless-steel electrodes measured at different temperatures.

According to the Bruce−Vincent−Evans equation, the Mg^{2+} transference number was determined to be 0.503 at room temperature (**Figure 3.1c**), which is higher than previous reported chloride-free solid-state electrolytes (0.3~0.4, **Table 3.2**). The high Mg^{2+} transference number is attributed to the entrapment of the negatively charged anions in the peculiar cationic Mg^{2+} solvating with tethered anions. [103] Nonflammability is another notable merit of MCE for safe rechargeable batteries. As depicted in **Figure 3.1d**, the MCE did not support combustion with only phase change between solid and liquid states at different temperatures. This phenomenon is in sharp contrast to the rapid burning of conventional $Mg(TFSI)_2$/PC electrolyte (**Figure 3.4**).

Figure 3.4 Flammability test of glass fiber membranes soaked with 0.5 M $Mg(TFSI)_2$/PC.

The thermal stability of MCE was further evaluated using TGA. The MCE presented no volatility up to 180 ℃ (**Figure 3.5**), superior to the typical carbonate-based liquid electrolyte with flash points near 120 ℃.

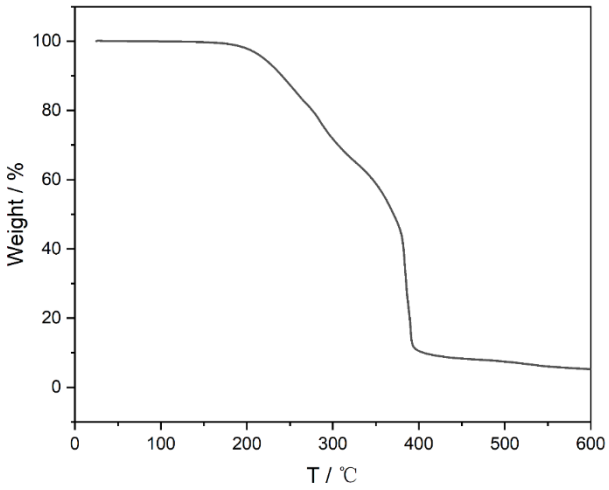

Figure 3.5 TGA curve of the eutectic $Mg(TFSI)_2$/Urea MCE.

FT-IR affirmed the intermolecular interactions between $Mg(TFSI)_2$ and urea in the deep eutectic structure. As shown in **Figure 3.6a**, the characteristic peaks observed in pure urea at approximately 1681 cm^{-1}, 1590 cm^{-1}, and 1460 cm^{-1} can be attributed to C=O, N-H, and C-N stretching vibrations, respectively [104]. Notably, **Figure 3.6 a** and **b** show the redshift of the characteristic peaks corresponding to S-N-S (1052 cm^{-1}), SO_2 (1187 and 1348 cm^{-1}), and C-F (1198 cm^{-1}) groups in $Mg(TFSI)_2$ after adding urea, indicative of chemical interactions between $TFSI^-$ anion and urea molecule. A close look at the FTIR spectra revealed an obvious change for the C=O stretch, which downshifted by 14 cm^{-1} from urea to MCE, accompanied by a visible expanding in the region of 3100-3600 cm^{-1} (N-H group). These results signify the formation of metal-oxygen coordination between Mg^{2+} and C=O groups, thus constructing a eutectic framework in MCE.

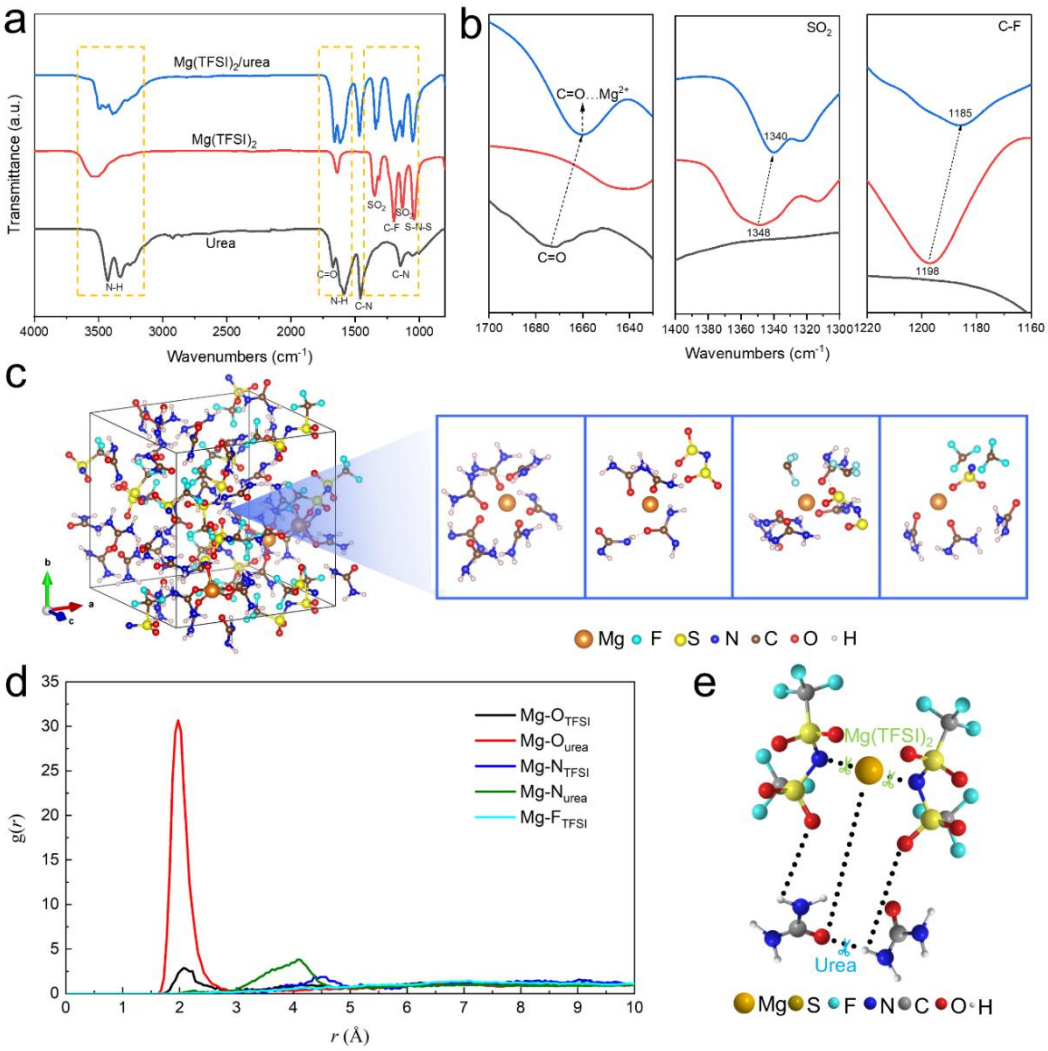

Figure 3.6 (a) FT-IR spectra of MCE. (b) Partial enlargement of view (a). (c) Snapshot of MD simulation box and the representative Mg^{2+}-solvation structures of $Mg(TFSI)_2$/urea with the molar ratio of $Mg(TFSI)_2$:urea = 1: 8. (d) RDF plots of MCE. (e) Schematic diagram of the interplay among Mg^{2+}, $TFSI^-$ and urea in MCE.

Theoretical simulations were carried out to elucidate the ion dissociation property in MCE. As shown in **Figure 3.6c**, the $TFSI^-$ anion and urea molecules are competing to coordinate with Mg^{2+} ions. The primary solvation sheath is dominated by urea molecules. By virtue of its structural flexibility, the urea ligand exhibited multiple coordination configurations with Mg^{2+} ions. To be specific, Mg^{2+} ions can be coordinated by six O atoms from urea molecules to form a crisscrossed framework, accompanied with the generation of hydrogen bond networks between urea and $TFSI^-$ anions (O_{urea}-H_{TFSI}). The O atom in $TFSI^-$ anions and N atom in urea

may replace Mg-O_{urea} solvation bonds to coordinate with Mg^{2+}, thus enriching the interionic attractions for enhanced Mg^{2+} mobility. [105] Moreover, radial distribution function (RDF) analysis provided more detailed information about the Mg^{2+} solvation configurations in the electrolyte. **Figure 3.6d** shows that the Mg^{2+} are primarily coordinated by urea molecules at around 2 Å (Mg-O_{urea}) and 4 Å (Mg-N_{urea}). The peak intensity of Mg-O_{urea} at around 2 Å is typically higher than that of Mg-O_{TFSI}, which indicates a strong ionic association force for Mg^{2+}-C=O. Analogous to the fast ionic mobility in highly concentrated lithium electrolytes with C=O-Li^+ coordination structures [106], the Mg^{2+}-C=O structure should promote the salt dissociation with enhanced oxidation stability. Overall, the interplays among Mg^{2+}, $TFSI^-$ and urea can be schematically depicted in **Figure 3.6e**, in which the coordination between Mg^{2+} and urea contributed to rapid Mg^{2+} diffusion.

3.2.2 Electrochemical performance

Solid-state batteries always encounter challenges of high electrolyte/electrode interfacial resistance and poor electrolyte permeability among active particles [107]. Leveraging the reversible melting and recrystallizing properties of MCE at elevated (above 80 ℃) and room temperatures, we proposed an in-situ interfacial regulation strategy to ensure conformal coating of MCE on electrode materials. Specifically, the liquid MCE at 80 ℃ was directly dropped on electrodes for direct solidification at room temperature, thus ensuring good electrolyte wettability. The feasibility of MCE for Mg stripping/plating was initially examined by cycling Mg//Mg symmetric cells. **Figure 3.7a** presents the voltage responses of the Mg//Mg cells using MCE at current densities ranging from 10 μA cm^{-2} to 100 μA cm^{-2}. Mg//Mg cells in $Mg(TFSI)_2$/PC liquid electrolyte were also measured as control. It is clearly observed that the symmetric cells in MCE delivered much lower overpotentials than these in $Mg(TFSI)_2$/PC.

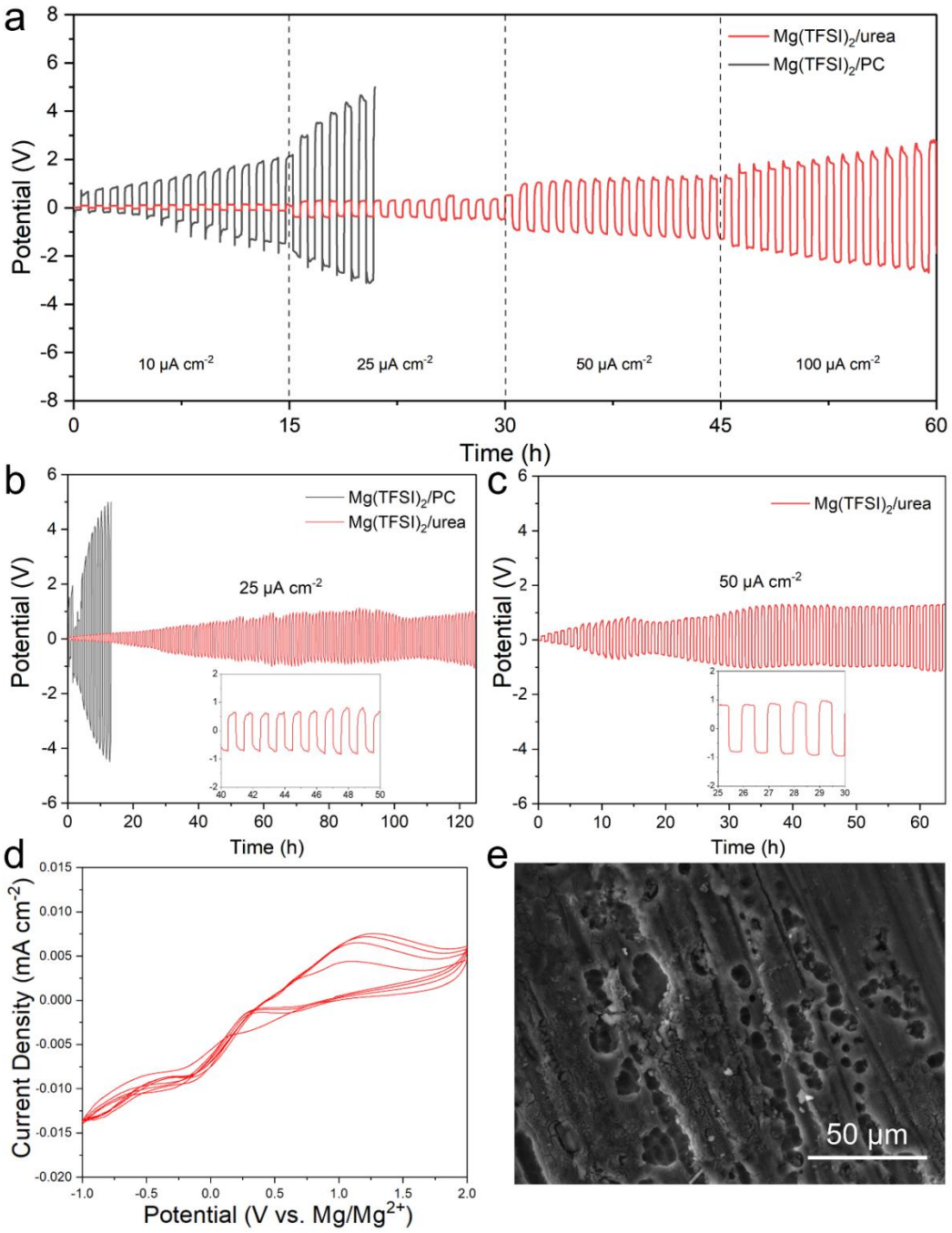

Figure 3.7 (a) Voltage responses of Mg//Mg symmetric cells with MCE and $Mg(TFSI)_2$/PC electrolytes at current densities from 10 μA cm^{-2} to 100 μA cm^{-2}. (b) Mg//Mg symmetric cells with MCE and $Mg(TFSI)_2$/PC electrolytes cycling at 25 μA cm^{-2}. (c) Mg//Mg symmetric cells with MCE cycling at 50 μA cm^{-2}. (d) CV curves of Mg//SS asymmetric cells with MCE. (e) SEM image of the Mg metal anode after stripping.

The extended cycling performance of Mg anode in MCE and $Mg(TFSI)_2$/PC electrolytes was also evaluated. Different from the long-cycling Mg-ion batteries using liquid electrolytes,

the reported solid-state Mg metal batteries in literature always present moderate cycle life at low current densities (**Table 3.1**). As shown in **Figure 3.7b** and **3.7c**, the cells with MCE exhibited remarkable reversibility of more than 120 hours at 25 μA cm^{-2} and 60 hours at 50 μA cm^{-2} with overpotentials of below 1 V, which indicates excellent compatibility with Mg metal electrodes. The fluctuating overpotentials of Mg//Mg symmetric cells can be attributable to the activation of solid-state-electrolyte at beginning and the cumulative unstable solid-state electrolyte/electrode interfaces during cycling, which should be ameliorated in future studies. In sharp contrast, the Mg//Mg cells with $Mg(TFSI)_2$/PC electrolyte experienced a rapid increase in polarization and failed in 13 hours at 25 μA cm^{-2}. This rapid failure aligns with previous reports of non-conductive interface forming on the surface of Mg metal [108]. Successful plating and stripping of Mg metal were further confirmed in SS//Mg asymmetric cells (**Figure 3.7d**). CV tests were performed at a scan rate of 0.5 mV s^{-1}, which presents reversible peaks at 1.2 V and -0.6 V *vs.* Mg/Mg^{2+} for plating and stripping reactions. Furthermore, SEM images of the cycled Mg metal anode and SS (**Figure 3.7e**) clearly illustrate the stripping and deposition of Mg metal.

Table 3.1 Summary of the compatibility of chloride-free solid-state electrolytes with Mg metal anodes.

Electrolyte formula	**ESW (SS *vs.* Mg/Mg^{2+})**	**Transference number**	**Mg//Mg cells**	**Overpotential (*vs.* Mg/Mg^{2+})**	**Ref.**
$Mg(TFSI)_2$/urea	**2.7 V**	**0.503**	**120 h at 25 μAcm^{-2}, 60 h at 50 μAcm^{-2}**	**< 1V**	**This work**
β-$Mg(BH_4)_2 \cdot CH_3NH_2$	1.2V	/	50 cycles at 10 μA cm^{-2} (60°C)	~50 mV	[109]
UIO66-MgIL	3.2 V	/	200 cycles at 1.57 μA cm^{-2}	~0.33 V	[110]
$Mg(NO_3)_2$/PEO-PVP	/	0.33	/	/	[111]
PEC-$Mg(TFSI)_2$/LiFSI	2 V	/	/	/	[112]

$Mg(ClO_4)_2$/ PVA-PVP	3.5 V	0.31	/	/	[113]
$Mg(Tf)_2$/PEO/$PYR_{14}TFSI$	/	0.4	Only CV	/	[114]
PEC-$Mg(TFSI)_2$	2.2 V	/	Only CV	/	[115]

To evaluate the practical feasibility of the MCE, Mg//V_2O_5 solid-state full cells were assembled. V_2O_5 is a widely used intercalation cathode for Mg ion batteries [116]. The solid-state full cells were tested at a current density of 20 mA g^{-1} within a voltage window of 0 and 2.2 V *vs.* Mg/Mg^{2+} (**Figure 3.8**). They demonstrated a high capacity of 172 mAh g^{-1} with a high average Coulombic efficiency of ~98%, and a moderate cycle life at room temperature, which is competitive among the reported chloride-free SSMRBs (**Table 3.2**).

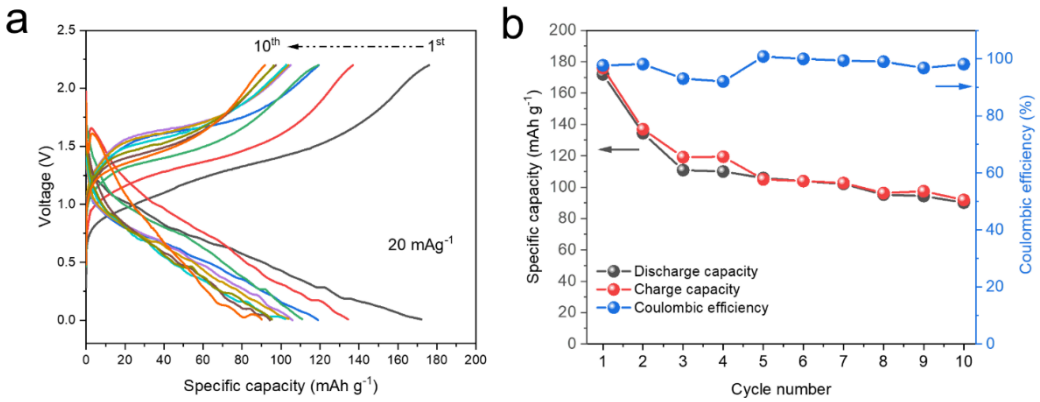

Figure 3.8 (a) Discharging/charging voltage profiles and (b) cyclic capacities and Coulombic efficiencies for Mg metal//V_2O_5 solid-state cells at 20 mA g^{-1}.

Table 3.2 Summary of the electrochemical performance of Mg metal batteries with chloride-free solid-state electrolytes.

Electrolyte formula	**Conductivity (S cm^{-1}) at RT**	**Cell type**	**Cell performance**	**Ref**
$Mg(TFSI)_2$/urea	**1.47×10^{-3}**	**Mg//V_2O_5**	**172 mAh g^{-1} at 20 mA g^{-1}**	**This work**
UIO66-MgIL	5.7×10^{-5}	Mg//PTCDA	27.7 mAh g^{-1} at 1 mA g^{-1}	[110]

$Mg(NO_3)_2$/PEO-PVP	5.8×10^{-4}	Mg//$MgMn_2O_4$	/	[111]
$Mg(TFSI)_2$/SiO_2/PVDF-HFP/THF-G3	0.83×10^{-3}	Mg//HTO-rGO	129 mAh g^{-1} at 50 mA g^{-1}	[117]
$Mg(BH_4)_2$/ MgO/ PEO	-	Mg//Mo_6S_8	100 mAh g^{-1} at 100℃	[118]
$Mg(BH_4)_2(NH_3BH_3)_2$	1.3×10^{-5} (30℃)	Mg//Mo	/	[119]
$Mg(NO_3)_2$/PVA-PAN	1.71×10^{-3}	Mg//MnO_2	/	[120]
$MgBr_2$/PWA/SN/PVA	1.1×10^{-6}	Mg//TiO_2	17.5 mAh g^{-1} at 0.1 mA cm^{-2}	[121]
$Mg(Tf)_2$/PEO/PYR_{14}TFSI	3.7×10^{-4}	Mg//TiO_2	45 mAh g^{-1} at 0.015 C	[114]

3.2.3 Electrolyte/electrode interface

Our electrochemical characterizations unequivocally demonstrated that the MCE enabled reversible Mg stripping and plating, highlighting the Mg^{2+} ion conducting nature for the electrode/electrolyte interface derived from MCE. To elucidate the structure and compositions of interface, we conducted rigorous characterizations after cycling Mg metal in symmetric cells. SEM images in **Figure 3.9a** and **3.9b** provide an overview of the interface, revealing an obvious macroporous structure. The highly rough morphology with the large electrolyte/electrode contact area can facilitate the Mg^{2+} ion diffusion [122].

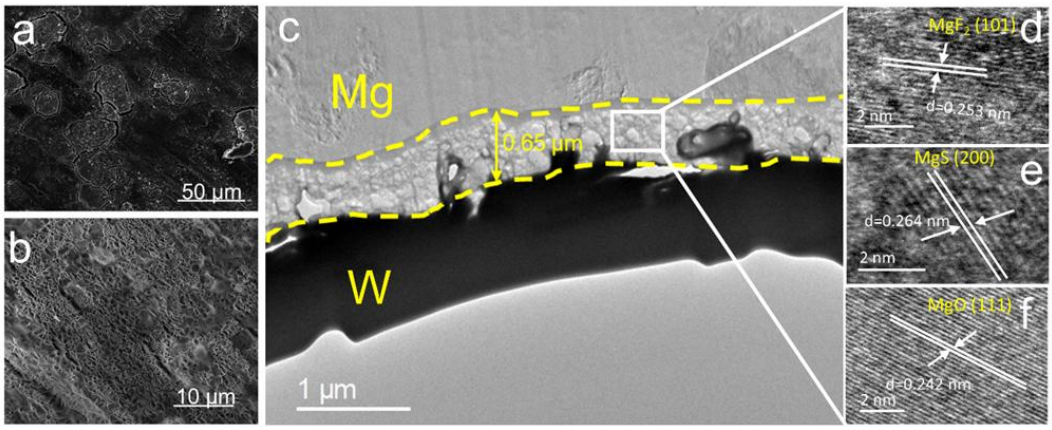

Figure 3.9 (a, b) SEM images of cycled Mg anodes showing porous surface morphology. (c-f) HRTEM images of the porous interface with inorganic compounds of MgF_2, MgO and MgS.

EDS mapping of the cross-sectional view in **Figure 3.10** indicates that the interface layer is mainly composed of Mg, F, O, S, and C elements, possibly forming inorganic (*i.e.*, MgF_2, MgO, MgS) and organic compounds. The FIB-TEM image in **Figure 3.9c** showed that the thickness of the macroporous Mg stripping layer was about 0.65 μm.

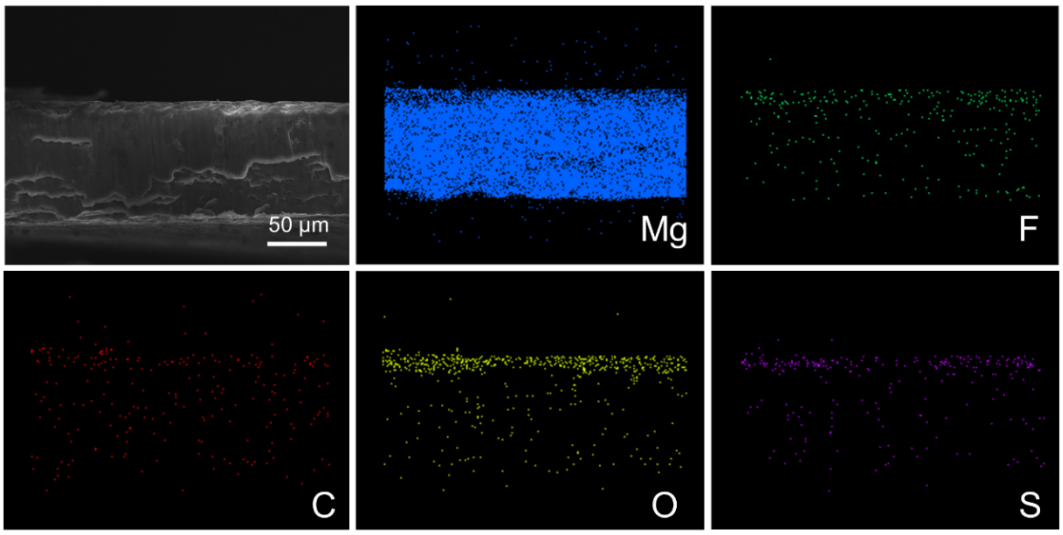

Figure 3.10 Cross-sectional SEM image of the cycled Mg electrode with the corresponding EDS mapping showing distinct separation of the Mg metal and the surface passivation layer.

EELS mapping (**Figure 3.11**) and HRTEM images revealed three kinds of nanocrystals, namely MgF_2 (**Figure 3.9d**), MgO (**Figure 3.9e**), and MgS (**Figure 3.9f**) in the interface layer. In the early studies, these compounds were regarded as passivating components [108]. However, recent works indicated that MgF_2 and MgS are Mg^{2+} ion conducting, which potentially contributes to the efficient Mg^{2+} diffusion [91, 122, 123]. MgF_2 was verified as an effective protective layer to suppress the side reactions and boost Li^+ migration in $LiCoO_2$ cathodes [124]. In addition, MgF_2 was also used as an electrolyte additive to regulate the electrolyte and the Mg^{2+} diffusion property at the interfacial regions in Mg rechargeable batteries [25, 125].

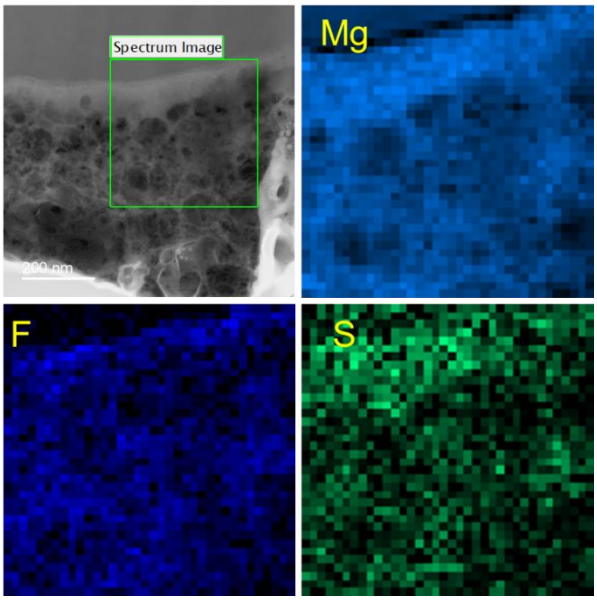

Figure 3.11 The STEM-EELS map on the surface of cycled Mg metal anode.

We also rested the Mg metal in contact with MCE for two days before delivering for SEM characterization. **Figure 3.12** shows no chemical corrosion trace and porous interface. Therefore, the porous interface layer on Mg cycling in MCE should be generated from electrochemical cycling. When the Mg metal was cycled in the $Mg(TFSI)_2$/PC electrolyte, no stripping pits were observed on the Mg metal surface, consistent with the previous report [91]. Therefore, the porous interface layer on Mg cycling in MCE should be generated from electrochemical cycling.

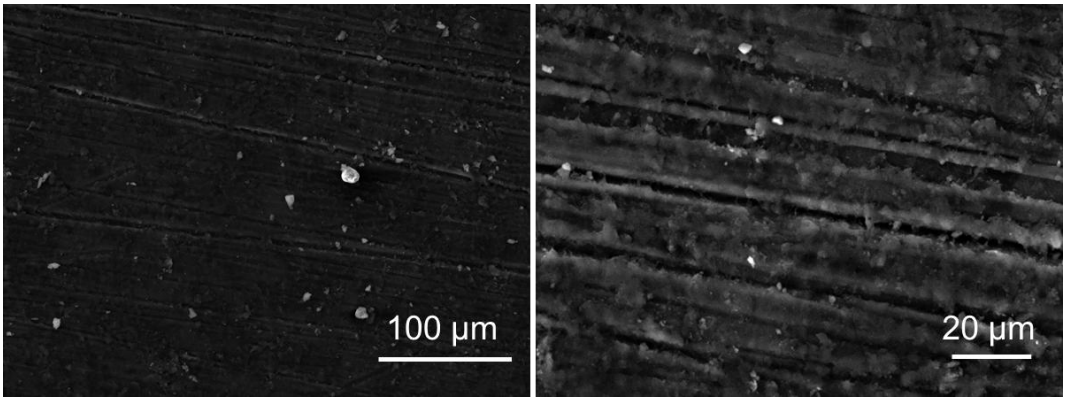

Figure 3.12 SEM images of Mg metal in contact with MCE for two days. No aggressive corrosion was observed on the surface of Mg metal.

To better understand the chemical nature of the interface layer, XRD and XPS measurements were carried out for cycled Mg electrodes in MCE and $Mg(TFSI)_2$/PC electrolytes. Grazing incidence XRD, a surface sensitive diffraction method, showed distinct MgF_2 peaks (PDF #41-1443) on Mg cycled in MCE (**Figure 3.13**), which is absent for the Mg metal cycled in $Mg(TFSI)_2$/PC electrolyte. This disparity is in line with above TEM observations and the reported interface generated from $Mg(TFSI)_2$/PC [108].

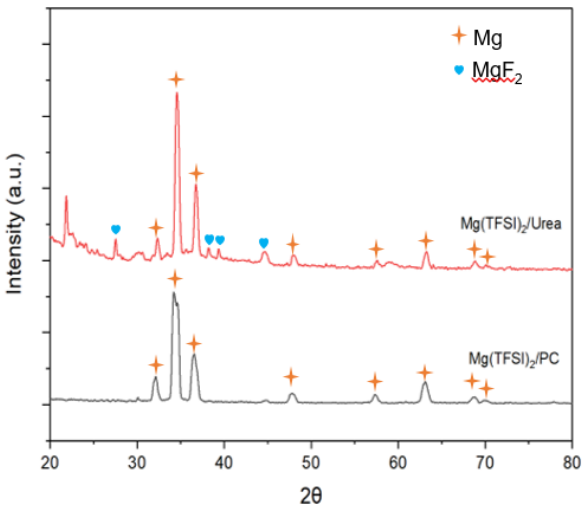

Figure 3.13 Grazing XRD patterns of the SEI layers on Mg metal cycling in MCE and $Mg(TFSI)_2$/PC electrolyte.

In view of the spatial chemical distribution of interfacial components, depth profiling XPS analyses with increasing sputtering time (0, 60, and 300 s) were performed. The C 1s spectra in **Figure 3.14** showed the carbonaceous species like C-C (284.6 eV), C-O (285.5 eV) and C=O (289.6 eV) throughout the sputtering depth [126], indicating the exist of organic species in the interface layer. The deconvoluted F1s spectra revealed the coexistence of organic -CF_3 component (688.8 eV) and inorganic MgF_2 (685.8 eV) [127]. With increasing the sputtering time, the peak intensity for MgF_2 improved gradually accompanied the decline for CF_3 peaks, suggesting a transfer from organic-rich surface to the inorganic-rich inner layer. Similarly, the S 2p and Mg 2p spectra also evidenced the hybrid organic (*i.e.*, -C-SO_2-C-) and inorganic (*i.e.*, MgS, MgF_2 and MgO) compounds in the interface layer [128]. As the formation of thick interface layer and the oxidation of Mg metal during sampling, the metallic Mg 2p peak is negligible. In virtue of the generation of these favorable chemicals with abundant grain boundaries and pores, the organic/inorganic hydride structure could allow Mg^{2+} transport through the interface layer for reversible Mg plating/stripping [122].

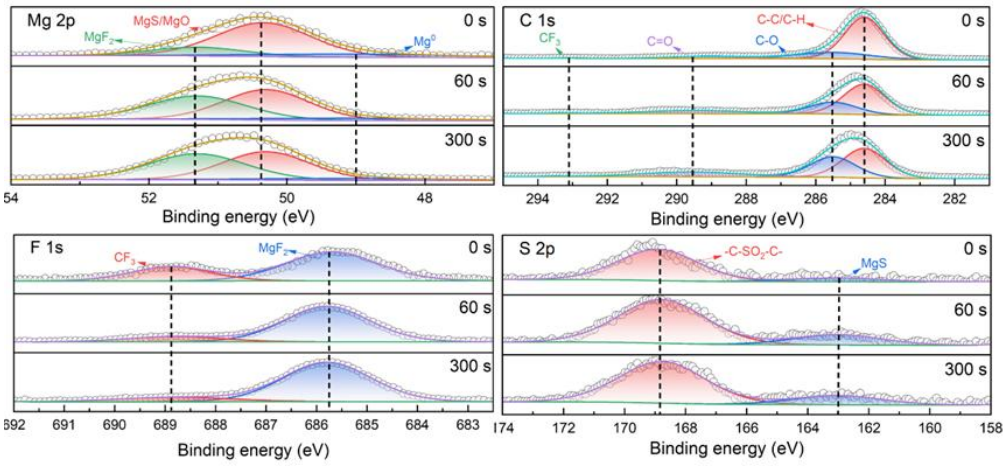

Figure 3.14 The depth XPS spectra of Mg 2p, C 1s, F 1s and S 2p for the surface of cycled Mg metal.

As a comparison, no MgF_2 and MgS signals were claimed on the surface of Mg metal cycled in $Mg(TFSI)_2$/PC electrolyte (**Figure 3.15**), which agrees with the grazing incidence XRD result.

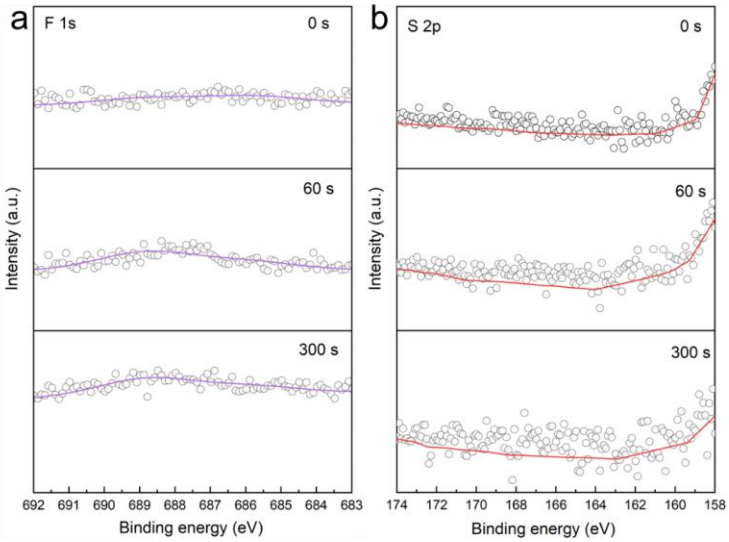

Figure 3.15 The depth (a) F1s and (b) S 2p XPS spectra of the surface of cycled Mg metal in 0.5 M $Mg(TFSI)_2$/PC.

TOF-SIMS was further conducted to corroborate the chemical distribution in the interface layer derived from MCE. As shown in **Figure 3.16a**, the layer is primarily made of F-containing species, which is widely distributed on the interface in both organic and inorganic forms. The F-rich species, especially MgF_2, are recognized as beneficial for the Mg^{2+}-conducting and

mechanical stability of SEI [129, 130]. Therefore, we highlighted the content variation diagram for MgF_x inorganics in **Figure 3.16b**. **Figure 3.16b** displays the depth-profiling distribution of the representative species, *i.e.*, F^-, O^-, MgF_3^- and MgF^-. MgS^- and MgF^- become more abundant closer to the Mg surface, which can be attributed to the $TFSI^-$ decomposition in contact with highly active Mg metal. Nevertheless, most inorganic fragments are F-containing compounds. The gradual decrease of MgF_3^- intensity is associated with the increment of MgF^- as a function of the sputtering time. This means that F-based inorganics are widely distributed through the interface layer in different forms. The increasing amounts of inorganics approaching the Mg metal surface agree with the HRTEM observation (**Figure 3.9c**). In conclusion, the reversible Mg stripping/plating capability in the new MCE can be attributed to the collective effect of the macroporous, organic/inorganic hybrid and F-rich interface layer, which could permit Mg^{2+} transport (**Figure 3.16c**). The inorganic/organic hybrid structure indicated better Mg^{2+} percolation compared to the organic-rich interface derived from $Mg(TFSI)_2$/PC electrolyte.

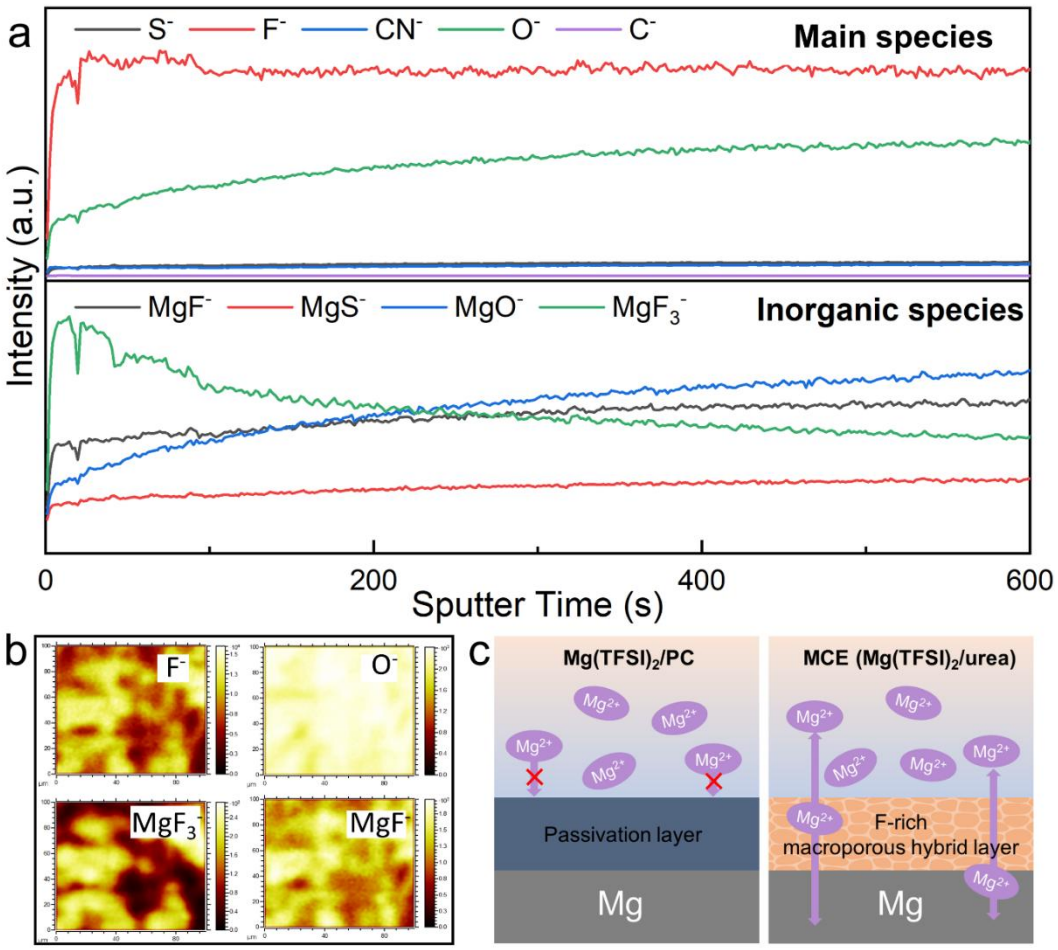

Figure 3.16 TOF-SIMS analysis of the interface layer on the surface of cycled Mg metal in MCE. Intensity evolutions of (a) chemical compounds as a function of sputtering time. (b) The corresponding distributions of the representative species in the sputtered section. (c) Schematic illustration of the Mg ion migration behaviors through the $Mg(TFSI)_2$/PC and MCE derived interface layers.

3.3 Summary

In this work, we have demonstrated the feasibility of in-situ crystallizing $Mg(TFSI)_2$/urea DES into solid-state electrolyte for room temperature solid-state Mg metal batteries. The introduction of urea could effectively dissociate Mg^{2+} and $TFSI^-$ to form urea-rich solvation configurations in the MCE. The resultant Mg^{2+}-C=O configurations can expedite Mg^{2+} ion diffusion and augment the transference number. The novel electrolyte has facilitated a commendable cycle life for Mg//Mg symmetric cells, exhibiting low overpotentials at room

temperature. Moreover, the practicability of the MCE was substantiated in Mg//V_2O_5 full cells, delivering a high reversible capacity of 172 mAh g^{-1}. The impressive electrochemical performance is attributed to the beneficial electrode/electrolyte interface structures, wherein the macroporous and organic/inorganic hybrid configuration aids the migration of Mg^{2+} ions through otherwise insulating materials. The insights gleaned from this study are anticipated to stimulate further advancements in the development of safe solid-state multivalent metal batteries.

Chapter 4 Glycol-glyme co-solvent electrolytes enable high-capacity and ultrastable VO_2 cathodes in magnesium ion batteries

4.1 Introduction

Stripping and plating of Mg metal had been extremely difficult because of the inevitable passivation of Mg metal surface in most aprotic electrolytes. Recently, a handful of novel electrolytes have been proposed for reversible Mg metal anodes, including APC [29] and MACC [32] solutions, thus propelling the RMB a step closer to practice. Unparalle to the decirnible progress in Mg anodes, high-capacity and high-power cathodes are still inaccessible, for example, a typical Mo_6S_8 cathode only delivers capacities of 60-80 mAh g^{-1} [131]. The limited Mg ion storage capacities have been mainly attributed to insufficent intersitial sites to accommodate Mg^{2+}, whereas the impact of cathode-electrolyte interface has been largely overlooked. Unlike Li counterparts, the strong solvation strength induces high energy barriers for the desolvation process at the cathode-electrolyte interface and facilitates the decomposition of anions [19, 49], thus leading to depressed Mg^{2+} transport and ionic-blocking CEI layers for unappealing cathode performance.

To enhance the compatbility between organic electrolytes and cathodes, several strategies have been proposed, including adding anion regulators [90], optimizing the solvent species [44, 132], and constructing artificial CEI layers for cathode materials [133, 134]. However, most of these investigations have been conducted on base of chloride-containing electerolytes and low-capacity Mo_6S_8 cathodes, leading to the corrosion of current collectors and unfavorable energy densities. Cathode-electrolyte compatibility is significantly influenced by the solvation structure of Mg^{2+}. Taking the commercially available $Mg(TFSI)_2$/DME electrolyte as the example, the strong interactions between DME and Mg^{2+} form a highly stable solvation structure, $[Mg(DME)_3]^{2+}$ [42]. This structure slows down the de-solvation process, affecting the

insertion kinetics of Mg^{2+} into cathode host [50]. The aggressive decomposition of $TFSI^-$ anions could also particially passivate the electrode surface that hinders Mg^{2+} ions transport [38].

Introducing cosolvents can effectively address these issues. For instance, Wang *et al.* [41] incorporated methoxyethyl-amine into $Mg(TFSI)_2$/DME electrolyte. The amines with stronge chelating effect adjusting the $[Mg\text{-solvent}]^{2+}$ configurations for facilitated desolvation and intercalation kinetics into $Mg_{0.15}MnO_2$ cathode. Despite the efficacy of methoxyethyl-amine additive, its high cost and limited availability necessitates the exploration of more affordable and effective chelators for high-capacity and statble cathodes in advanced RMBs.

In this work, we introduced a hydroxyl-rich ethylene glycol (EG) solvent into the chloride-free $Mg(TFSI)_2$/DME electrolyte as a solvation chelator. EG can weaken the strongly coordinated $[Mg(DME)_3]^{2+}$ complexes and create hydrogen-bonding networks for rapid Mg^{2+} diffusion. When cycling a high-capacity VO_2 cathode in the optimal $Mg(TFSI)_2$ EG/DME electrolyte, it presents remarkable electrochemical performance with a high capacity of 258 mAh g^{-1} and an exceptional capacity retention of 84.4% after 2000 cycles at 500 mA g^{-1}, which are much higher than the initial capacities of 54 mAh g^{-1} in $Mg(TFSI)_2$/DME electrolyte and 160 mAh g^{-1} in $Mg(TFSI)_2$/EG electrolyte. The enhanced cathode performance can be attributed to the synergistic effects from enhanced electrochemical kinetics and modified CEI, namely, (i) EG could disrupt the strong solvation of $[Mg(DME)_3]^{2+}$ complexes by forming hydrogen bonding network with DME, thus lowering the de-solvation energy barrier and facilitating Mg^{2+} diffusion into the VO_2 cathode host, (ii) the strong interactions between EG and $TFSI^-$ ions suppress the CEI growth from $TFSI^-$ decomposition, thereby enhancing the cyclic performance. The $Mg(TFSI)_2$ EG/DME also exhibit high compatibility with Mg anode. The Mg//Mg symmetric cells demonstrated a stable cycle life exceeding 300 cycles with low polarization. Furthermore, the practical applicability of the electrolyte was confirmed in Mg//VO_2 full cells, which delivered high capacities above 160 mAh g^{-1} over 50 cycles.

4.2 Results and discussion

4.2.1 Chemical structure of the co-solvent electrolytes

$Mg(TFSI)_2$/DME electrolyte solution has been widely investigated in RMBs with high solubility and oxidative stability, thus it is selected as the model electrolyte in this work to correlate the electrolyte structure and cathode performance [19, 50]. To facilitate the desolvation of $[Mg(DME)_3]^{2+}$ complex at cathode/electrolyte interface, we introduced the EG solvent because of its low volatility, high polarity, and abundant long pair oxygens, which could enter the primary solvation sheath [135, 136]. **Figure 4.1a** illustrates that the oxygen atoms in EG exhibit a stronger negative electrostatic potential (-31.93 kcal mol^{-1}) than that in DME (-29.98 kcal mol^{-1}). The high polarity for EG enhances its coordination with Mg^{2+} in EG/DME-based electrolytes. The lower highest occupied molecular orbital (HOMO) energy level of EG (-7.85 eV) than DME (-7.094 eV) indicates the higher theoretical oxidative stability of EG.

To illustrate the role of EG in regulating $Mg(TFSI)_2$/DME electrolyte structure, we prepared a series of $Mg(TFSI)_2$ EG/DME electrolytes with EG ratios (v_{EG}) of 0 %, 25 %, 50 %, 75 %, 100 % in volume. **Figure 4.1b** exhibits the Raman spectra of these electrolyte solutions. It shows that the characteristic peaks for free DME (849 cm^{-1}) and EG (864 cm^{-1}) molecules can be split into two peaks at 848/882 cm^{-1} and 865/899 cm^{-1}, respectively, after adding 0.5 M $Mg(TFSI)_2$. For the $Mg(TFSI)_2$/DME electrolyte (v_{EG} ratio = 0%), the solvated DME is illustrated by a characteristic peak at ~882 cm^{-1} [137]. With the increase of v_{EG} ratio, the peak intensity for Mg^{2+}-DME coordination (red highlighted) decreases gradually in association with the increase of the Mg^{2+}-EG peak intensities at 899 cm^{-1} (blue highlighted).[138] This gradual evolution suggests stronger coordination of Mg^{2+}-EG than Mg^{2+}-DME, consistent with our DFT calculations (**Figure 4.1a**).

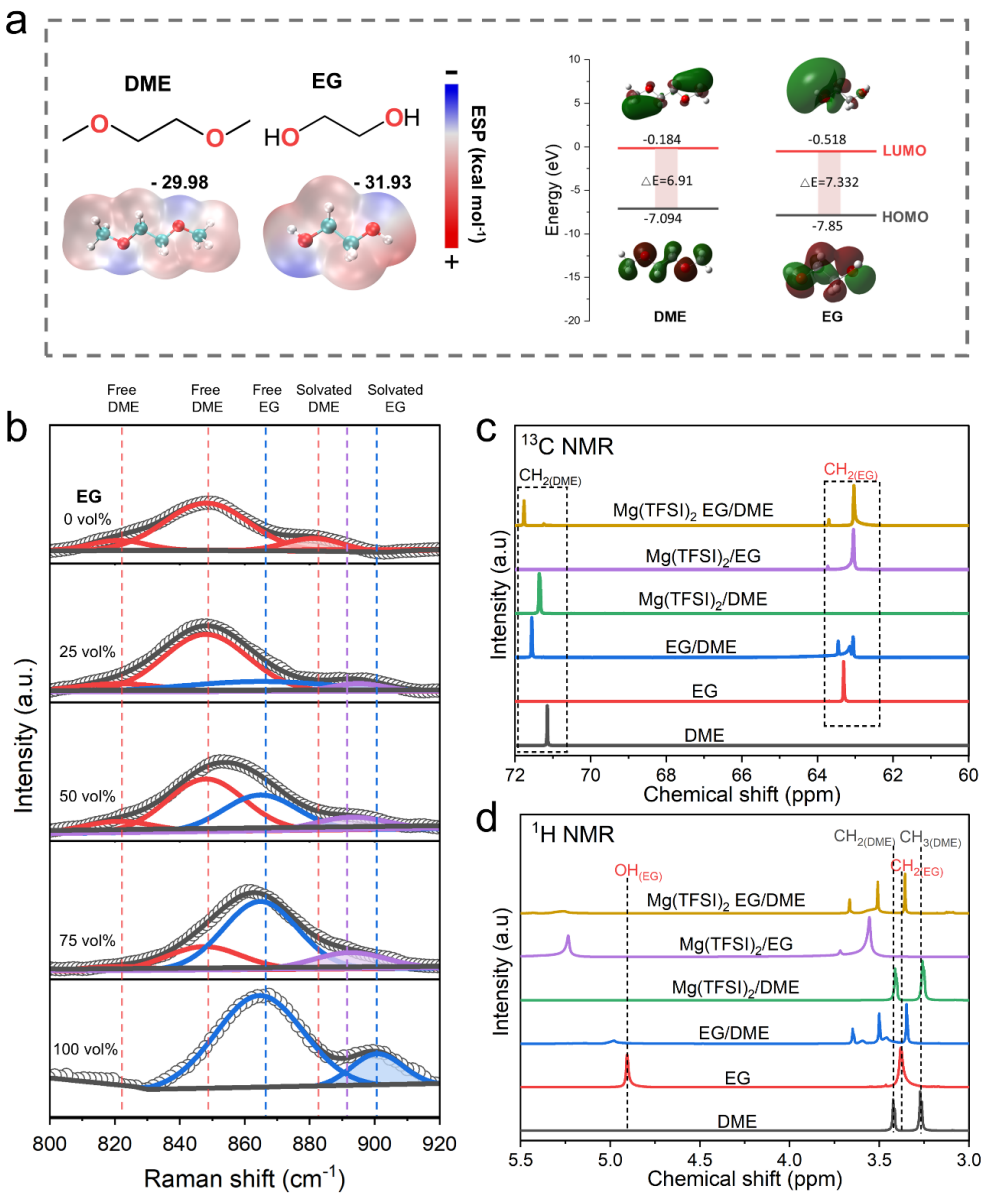

Figure 4.1 (a) Chemical structure, electrostatic potential and LUMO and HOMO energy levels comparison of DME and EG solvents. (b) Raman spectra of hybrid electrolytes with different volume ratios of EG. (c) ^{13}C and (d) ^{1}H NMR spectra of DME, EG, and EG/DME solvents, as well as their corresponding electrolyte solutions.

The ionic conductivity of the electrolytes decreased as the v_{EG} ratios increased, *i.e.,* 15.3 mS cm^{-1} for v_{EG} = 0 % to 2.53 mS cm^{-1} for v_{EG} = 100 % (**Figure 4.2a**), possibly due to the high viscosity of EG [139]. The optimal Mg(TFSI)$_2$ EG/DME electrolyte (v_{EG} = 75 %) delivered an electrochemical stability window of 3.85 V (**Figure 4.2b**), which will be large enough for the high-capacity VO_2 cathodes.

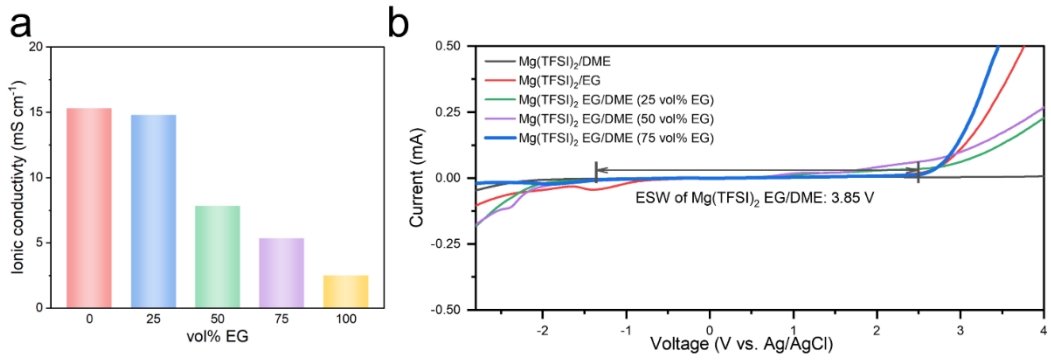

Figure 4.2 (a) Ionic conductivities and (b) ESW of electrolytes with different volume ratio of EG.

FTIR characterizations were carried out to decipher the intermolecular structures in the electrolytes (**Figure 4.3**). The EG-containing electrolytes show a broad and strong O–H stretching vibration between 3100 and 3700 cm^{-1}, which is ascribed to diverse hydrogen bonding environments in EG molecules. The peaks in the regions of 820-920 cm^{-1} and 1320-1380 cm^{-1} are assigned to solvent-Mg^{2+} and anion-Mg^{2+} coordination. Compared to the $Mg(TFSI)_2$/DME electrolyte, the $Mg(TFSI)_2$ EG/DME electrolyte exhibits a blue shift for the Mg^{2+}-DME peak from 865.9 cm^{-1} to 880.5 cm^{-1}, consistent with Raman spectra in **Figure 4.1b**. In addition, the SO_2 stretching vibrations at 1333.7 and 1354.5 cm^{-1} shifted to 1310 and 1351.3 cm^{-1} after adding the EG solvent. FTIR results suggest the strong Mg^{2+}-EG coordination and the hydrogen bonding interactions between EG and $TFSI^-$ anions.

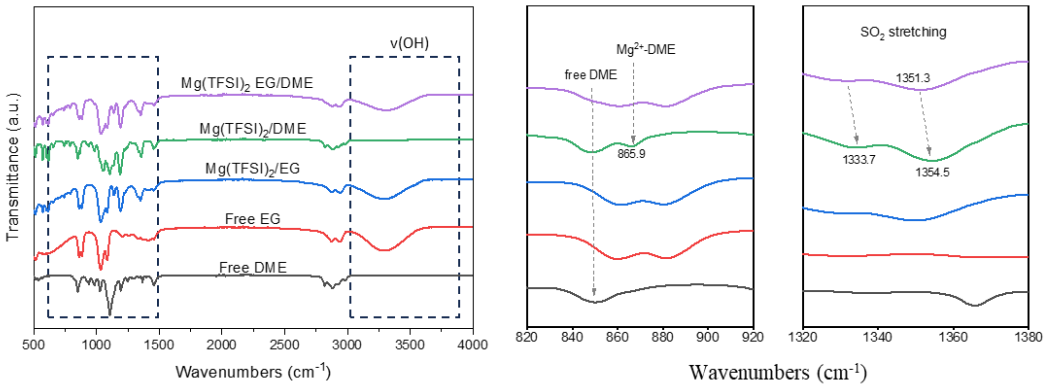

Figure 4.3 FT-IR spectra of EG, DME and EG/DME solvents with/out $Mg(TFSI)_2$.

The ^{13}C and ^{1}H NMR spectra of EG, DME solvents and their corresponding electrolyte solutions are shown in **Figure 4.1c and 4.1d**, respectively. Upon the addition of $Mg(TFSI)_2$ salt into DME solvent, the methylene ^{13}C peak ($-CH_2$) in DME slightly shifted to upfield by 0.22 ppm. The ^{1}H NMR peaks at 3.42 ppm ($-CH_2$ in DME) and 3.26 ppm ($-CH_3$ in DME) showed negligible shifts. In constrast, the addition of $Mg(TFSI)_2$ salt into EG or EG/DME solvents resulted in significant changes in both ^{13}C and ^{1}H chemical shifts. Specially, the ^{13}C peaks in EG shifted upfield by 0.3 ppm, while the ^{1}H NMR peak in EG red-shifted by 0.33 ppm for the $Mg(TFSI)_2$/EG solution. The difference suggests that EG exhibits stronger coordination strengths than DME to $Mg(TFSI)_2$ species. Similarly, in the $Mg(TFSI)_2$/EG electrolyte, the ^{1}H peak at 4.98 ppm for EG/DME solvent shifted to 5.26 ppm. The ^{13}C NMR spectra of EG/DME cosolvent and the corresponding electrolyte also showed noticeable differences in chemical shifts, comparable to these in EG systems. Interestingly, the ^{1}H peaks for -OH and $-CH_2$ in EG/DME cosolvent are broader and shifted upfield compared to EG solvent, suggesting the formation of hydrogen-bonding networks between the $CH_3{-}O{-}CH_2{-}$ group in DME and -OH group in EG. Such hydrogen bonding network can facilitate Mg^{2+} diffusion [54, 140].

MD simulations were conducted to analyze the electrolyte structures by comparing the radical distribution functions (RDFs) and coordination numbers (CN). For the $Mg(TFSI)_2$/DME electrolyte (**Figure 4.4a** and **4.4b**), the coordination mainly happens between Mg^{2+} and C-O groups with three DME molecules surrounding one Mg^{2+} (designated as $[Mg(DME)_3]^{2+}$) [42]. The rigid $[Mg(DME)_3]^{2+}$ has been recognized unfavorable for Mg^{2+} intercalation reactions arising from its high desolvation energy barriers [19, 141]. Furthermore, RDF reveals a higher Mg-O(EG) peak intensity than these for Mg-O(DME) and Mg-O($TFSI^-$) (**Figure 4.4c**). DME molecules are potentially squeezed into the secondary solvation sheath. The average CN of Mg^{2+} ions with EG is 2.8, which is higher than the 1.7 for DME solvent and 1.5 for $TFSI^-$ anion. The dominant solvation species are calculated as $[Mg(EG)_2(DME)(TFSI^-)]^+$ in the electrolyte (**Figure 4.4d**),comprising the highest proportion of 62.5% among the solvation species (**Figure 4.5**).

Figure 4.4a and **4.4b** shows the binding energies among the electrolyte components. EG exhibits stronger binding strength with DME (-0.239 eV) and $TFSI^-$ (-0.627 eV) than these for DME solvent molecules. On the other hand, EG indicates the weakest binding strenght with Mg^{2+} (*i.e.,* Mg^{2+}-$TFSI^-$ > Mg^{2+}-DME > Mg^{2+}-EG, **Figure 4.4c**). It is reasonable to speculate that abundant hydrogen bonds can form between DME and EG, and the $TFSI^-$ anions surrounding Mg^{2+} can be interacted by EG in the secondary solvation sheath.

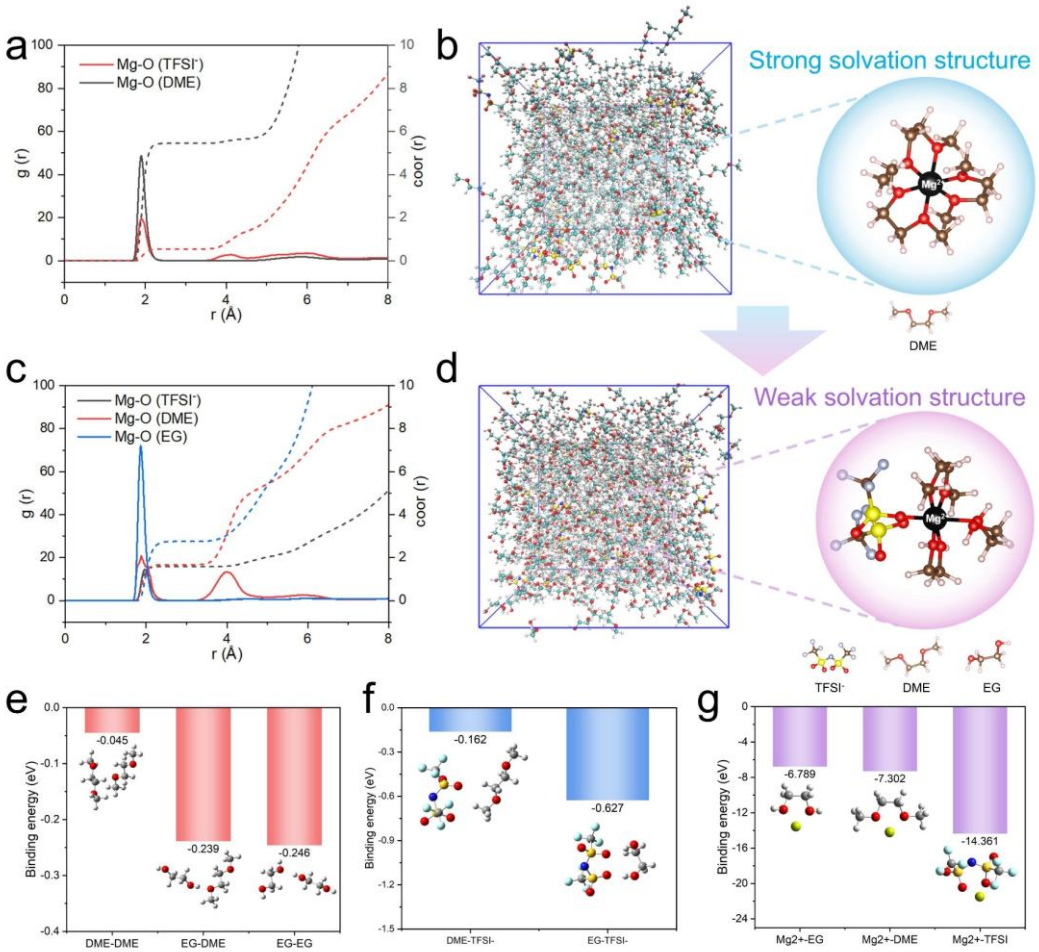

Figure 4.4 (a) MD simulated radial distribution functions for $Mg(TFSI)_2$/DME electrolyte. (b) 3D snapshot of $Mg(TFSI)_2$/DME electrolyte highlighting the Mg^{2+}-solvation structure. (c) MD-simulated radial distribution functions for $Mg(TFSI)_2$ EG/DME electrolyte. (d) 3D snapshot of $Mg(TFSI)_2$ EG/DME electrolyte showing the typical Mg^{2+}-solvation structure. (e) Binding energies among DME-DME, DME-EG and EG-EG. (f) Binding energies of $TFSI^-$ with DME, EG. (g) Binding energies of Mg^{2+} with DME, EG, and $TFSI^-$.

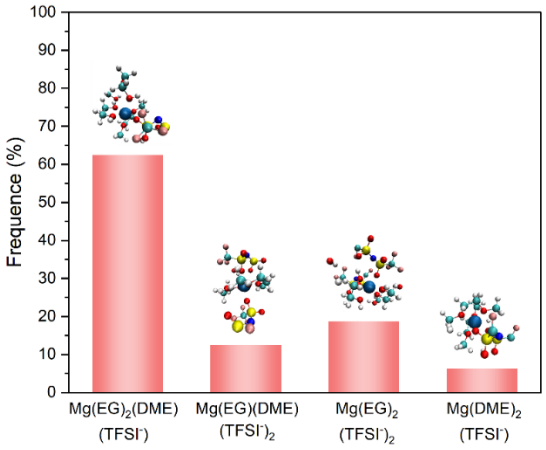

Figure 4.5 Distribution of Mg^{2+} solvation species from MD simulations of the $Mg(TFSI)_2$ EG/DME electrolytes.

Impressively, the weaker binding strength of EG-Mg^{2+} (-6.789 eV) than DME-Mg^{2+} (-7.302 eV), combined with the reduced steric hindrance effect of EG molecules (**Figure 4.6a**), enhanced the entrance of $TFSI^-$ anions into the first solvation sheath of Mg^{2+} in the cosolvent electrolyte. Although EG presents slightly higher negative electrostatic potential than DME, the stronger chelation effect results in a higher binding energy of Mg^{2+}-DME than Mg^{2+}-EG (**Figure 4.6b)** [142, 143], implying the dominant role of DME in the solvation sheath.Together with above experimental characterizations, we can clonclude that EG molecules could greatly modify the $Mg(TFSI)_2$/DME electrolyte strucrure by weakening the $[Mg(DME)_3]^{2+}$ complex and stabilizing the $TFSI^-$ anions.

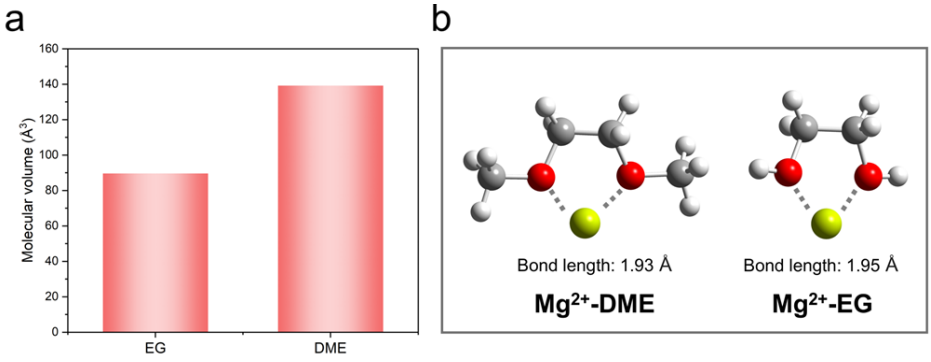

Figure 4.6 (a) Molecular volumes of EG and DME. (b) Bond lengths for Mg^{2+}-DME and Mg^{2+}-EG.

4.2.2 Electrochemical performance with VO_2 cathode

To evaluate the electrochemical performance of the $Mg(TFSI)_2$ EG/DME electrolyte in intercalation-type cathodes, we assembled a Mg-ion half-cell containing VO_2 cathodes and AC counter electrodes. VO_2 is chosen for its high electronic conductivity and elevated operating voltage. However, the narrow channels inherent to its monoclinic structure restrict Mg^{2+} diffusion, resulting in limited capacity and sluggish kinetics in conventional electrolytes. The VO_2 was prepared by a hydrothermal method [69]. SEM and TEM images in **Figure 4.7a to 4.7c** show a nanorods morphology and high crystallinity for the VO_2 cathode material. Rietveld XRD refinement in **Figure 4.7d** indexed the VO_2 to a monoclinic B-phase with lattice parameters of a = 12.03 Å, b = 3.693 Å, c = 6.42 Å, and $\alpha = \gamma = 90°$, $\beta = 106.1°$ in the C2/m space group [144]. AC is chosen as the counter electrode because of its high specific surface area and electrochemical inactivity in Mg ion electrolytes, which could rule out the complexity arising from unexpected side reactions of Mg metal anodes in most electrolytes. Mg^{2+} intercalation in cathodes is accompanied by anion adsorption on AC [89, 145].

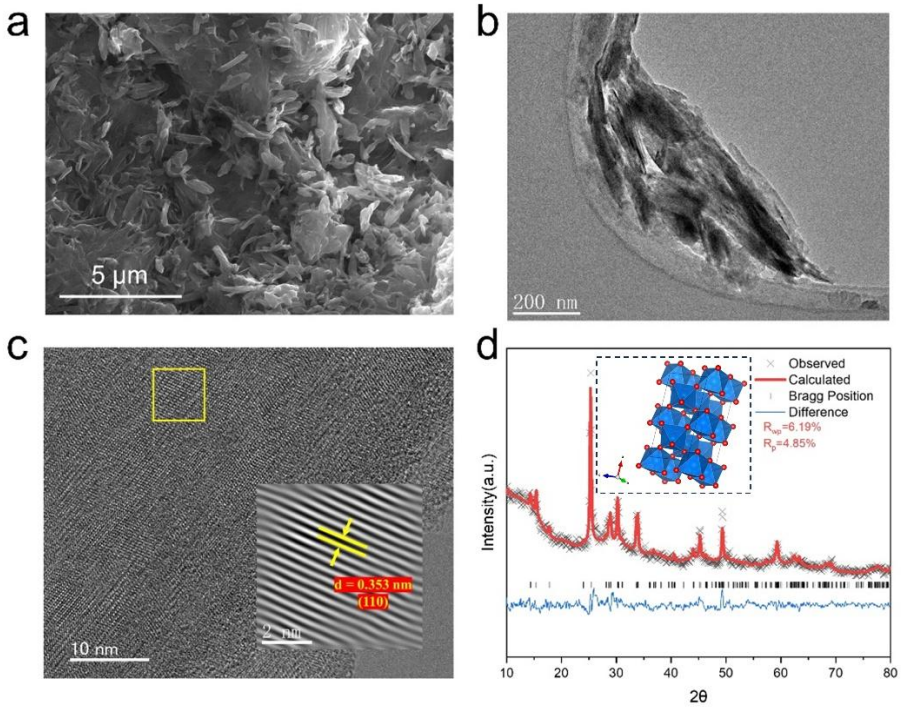

Figure 4.7 (a) SEM image, (b) TEM image, and (c) HRTEM image of VO_2. Inset (c) shows

the FTT image of the (110) planes with a lattice distance of 0.353 nm for pristine VO_2. (d) XRD pattern and Rietveld refinement of VO_2, with the crystal structure shown in the inset).

CV measurements were initially performed at a scan rate of 0.2 mV s^{-1} to identify the Mg-ion intercalation/deintercalation reactions in a voltage window of −1.3 to 0.2 V versus AC, which can be calibrated to the voltage range of 1.1 to 2.6 V versus Mg^{2+}/Mg, according to previous works [70, 89]. As shown in **Figure 4.8**, the CV curves in $Mg(TFSI)_2$/DME electrolyte show neglectable reduction and oxidation peaks, suggesting poor activity of VO_2 cathodes. The irreversibility may be caused by the slow desolvation kinetics in $Mg(TFSI)_2$/DME electrolyte [146]. In contrast, the EG solvent could significantly improve Mg ion storage capacities in VO_2. The initial cycling profiles in $Mg(TFSI)_2$ EG/DME electrolyte display distinctive cathodic and anodic redox peaks at -1.15 V and -0.88 V versus AC, respectively. Over the following ten cycles, the cathodic peak shifts positively to -1 V and remains stable, while a new anodic peak emerges at -0.23 V, likely indicating the activation behavior. CV curves in $Mg(TFSI)_2$ EG/DME electrolyte are highly overlapped for excellent reversibility of the Mg-ion cells. The VO_2 cathode exhibited similar CV results in $Mg(TFSI)_2$/EG electrolyte, but the current response is not as high as in $Mg(TFSI)_2$ EG/DME electrolyte, attributable to the lower ionic conductivity of $Mg(TFSI)_2$/EG electrolyte.

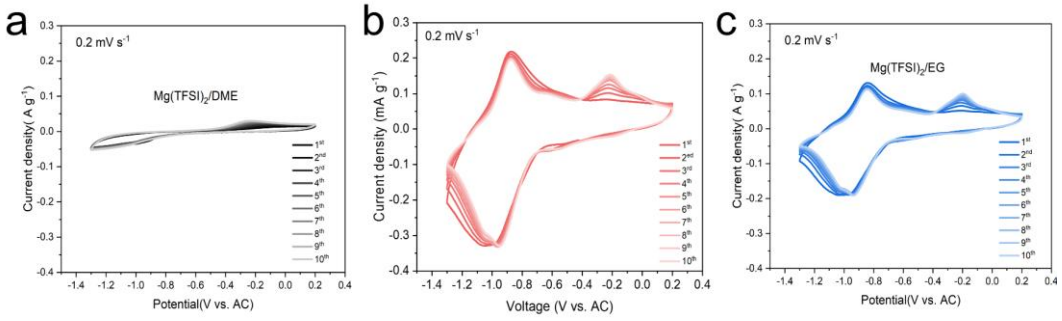

Figure 4.8 The 1st to 10th cycles of CV curves for VO_2 cathodes in (a) $Mg(TFSI)_2$/DME, (b) $Mg(TFSI)_2$ EG/DME, and (c) $Mg(TFSI)_2$/EG electrolyte.

The cyclic performance of VO_2 cathodes in $Mg(TFSI)_2$/DME, $Mg(TFSI)_2$/EG, and $Mg(TFSI)_2$ EG/DME electrolytes at 100 mA g^{-1} are shown in **Figure 4.9a** and **4.9b**.

Interestingly, VO_2 cathodes indicate solvent-dependent capacities. The initial capacity of VO_2 cathode in DME-based electrolyte is only 54 mAh g^{-1}, which declines to 29 mAh g^{-1} at the 500th cycle. In the EG-based electrolyte, VO_2 cathode delivers a higher capacity of 160 mAh g^{-1} at the 1st cycle and maintains half of the initial capacity after cycling. Notably, in the EG/DME-based electrolyte, VO_2 cathode achieves the highest specific capacity of 255 mAh g^{-1} and retains 210 mAh g^{-1} after 500 cycles.

The rate performances are shown in **Figure 4.9c**. VO_2 cathodes delivered high capacities of 254, 202, 180, 155, 131 and 121 mAh g^{-1} in the $Mg(TFSI)_2$ DME/EG electrolyte at current densities of 100, 200, 300, 500, 800, and 1000 mA g^{-1}, respectively. When the current density returned back to 100 mA g^{-1}, a high capacity of 236 mAh g^{-1} is maintained, in contrast to the low cyclic capacities in $Mg(TFSI)_2$/EG and $Mg(TFSI)_2$/DME electrolytes. **Figure 4.9d** shows the discharge/charge voltage profiles of VO_2 in $Mg(TFSI)_2$ EG/DME electrolyte at different current densities with distinguished voltage plateaus. The VO_2 cathodes were also cycled in $Mg(TFSI)_2$ EG/DME electrolyte at a high current density of 500 mA g^{-1} over 2000 cycles (**Figure 4.9e**), which delivers an exceptionally high capacity retention of 84.4%, corresponding to a capacity decay rate of 0.008 % per cycle. We compared the cyclic performance VO_2 cathodes in $Mg(TFSI)_2$ EG/DME electrolyte with representative cathodes in $Mg(TFSI)_2$-based electrolytes (**Table 4.1**). This work demonstrates one of the highest cyclic capacities (>250 mAh g^{-1}) and an ultralong cycle life (2000 cycles) for cathodes in RMBs.

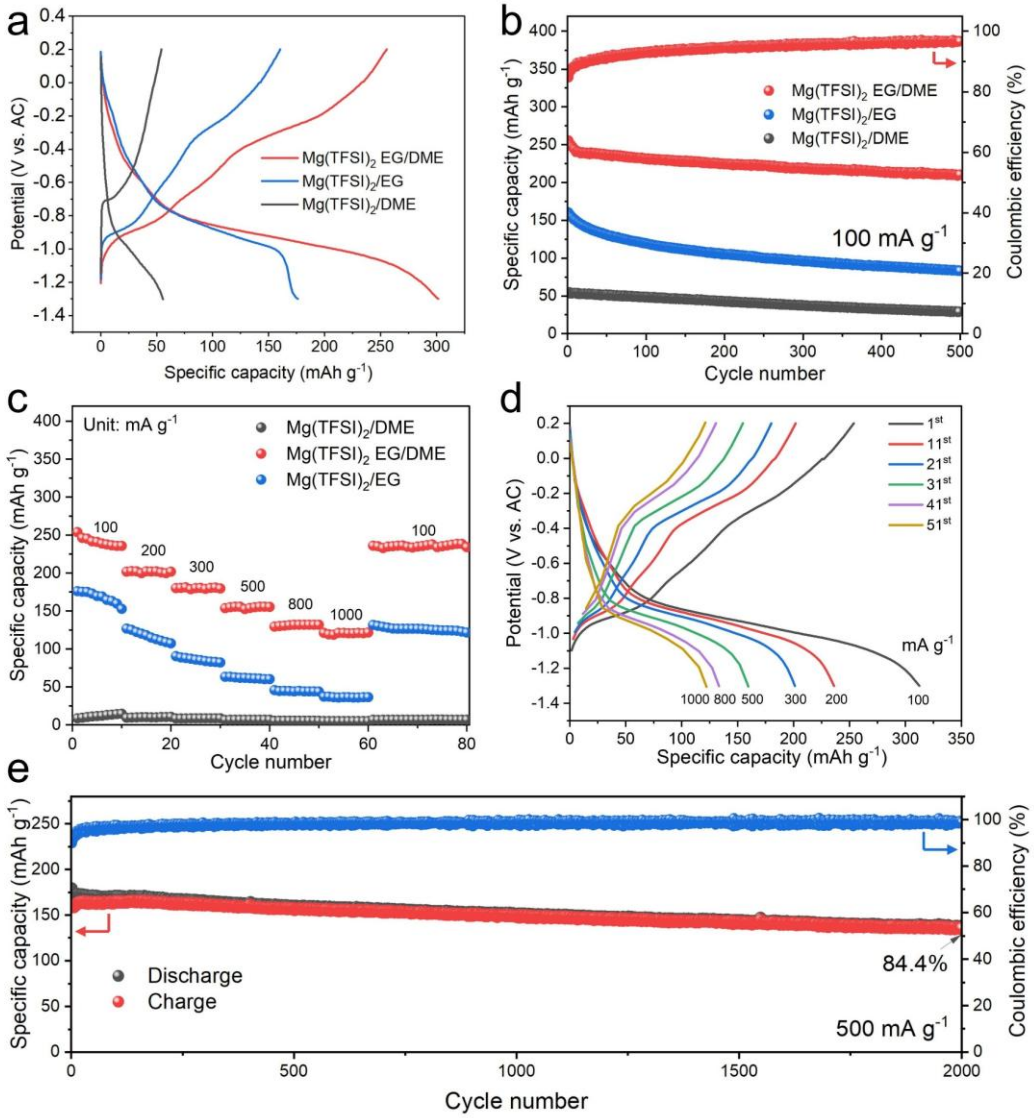

Figure 4.9 (a) Voltage profiles curves, (b) cyclic capacities and Coulombic efficiencies, and (c) rate capability of VO_2 cathodes in the three electrolytes of $Mg(TFSI)_2$ EG/DME, $Mg(TFSI)_2$/EG, and $Mg(TFSI)_2$/DME. (d) Voltage-capacity curves of VO_2 cathodes in $Mg(TFSI)_2$ EG/DME electrolyte at different current densities. (e) Cycling stability of VO_2 in $Mg(TFSI)_2$ EG/DME electrolyte at 500 mA g^{-1}.

Table 4.1 Comparison of the electrochemical performance for VO_2 in $Mg(TFSI)_2$ EG/DME electrolyte with other representative cathodes in Mg ion batteries.

Working electrode	Counter electrode	Electrolyte	Specific capacity	Capacity /Cycle number/current	Ref.
VO_2	AC	$Mg(TFSI)_2$ EG/DME	258 mAh g^{-1}@100 mA g^{-1}	136 mA g^{-1} /2000/500 mA g^{-1}	This work

$V_2O_5 \cdot nH_2O$	Sn	$Mg(ClO_4)_2$/AN	160 mAh g^{-1}@20 mA g^{-1}	120 mAh g^{-1}/50/30 mA g^{-1}	[147]
NaV_3O_8	AC	$Mg(ClO_4)_2$/AN	204.2 mAh g^{-1} @100 mA g^{-1}	175 mAh g^{-1}/100/100mA g^{-1}	[148]
Mg-OMS-2	AC	$Mg(NO_3)_2/H_2O$	115 mAh g^{-1} @100 mA g^{-1}	44.1 mAh g^{-1}/500/100 mA g^{-1}	[149]
CuHCF	Mn-NVO	$MgCl_2 \cdot 6H_2O$/ acetamide/urea	59.1 mAh g^{-1} @100 mA g^{-1}	38.7 mAh g^{-1}/800/1 A g^{-1}	[60]
$Mg_XLiV_2(PO_4)_2$	PPMDA @MCNTs	$Mg(TFSI)_2/H_2O$	52 mAh g^{-1} @100 mA g^{-1}	38.9 mAh g^{-1}/6000/2 A g^{-1}	[150]
Nb_2O_5@GO	AC	$Mg(TFSI)_2$/DME	100 mAh g^{-1}@50 mA g^{-1}	75 mAh g^{-1}/200/ 50 mA g^{-1}	[151]

4.2.3 Reaction kinetics of the electrolytes

The largely different Mg ion storage capacities for VO_2 cathodes in different electrolytes can be attributed to the ameliorated Mg^{2+} diffusion at the electrolyte/electrode interface. To this end, we examined the desolvation energy and diffusion kinetics of Mg^{2+} in the VO_2 cathode. Mg^{2+} de-solvation energy was evaluated by assembling symmetric cells with VO_2 cathodes at a half-charged state in varying-temperature electrochemical impedance spectroscopy (EIS) [152, 153]. As shown in **Figure 4.10a** to **4.10c** and **Table 4.2**, the desolvation energy in $Mg(TFSI)_2$ EG/DME electrolyte is 4.61 kJ mol^{-1}, which is significantly lower than that in $Mg(TFSI)_2$/DME electrolyte (9.94 kJ mol^{-1}). The relatively larger charge transfer impedance of VO_2 cathodes in $Mg(TFSI)_2$ EG/DME electrolyte can be attributed to its lower ionic conductivity and cathode wettability.

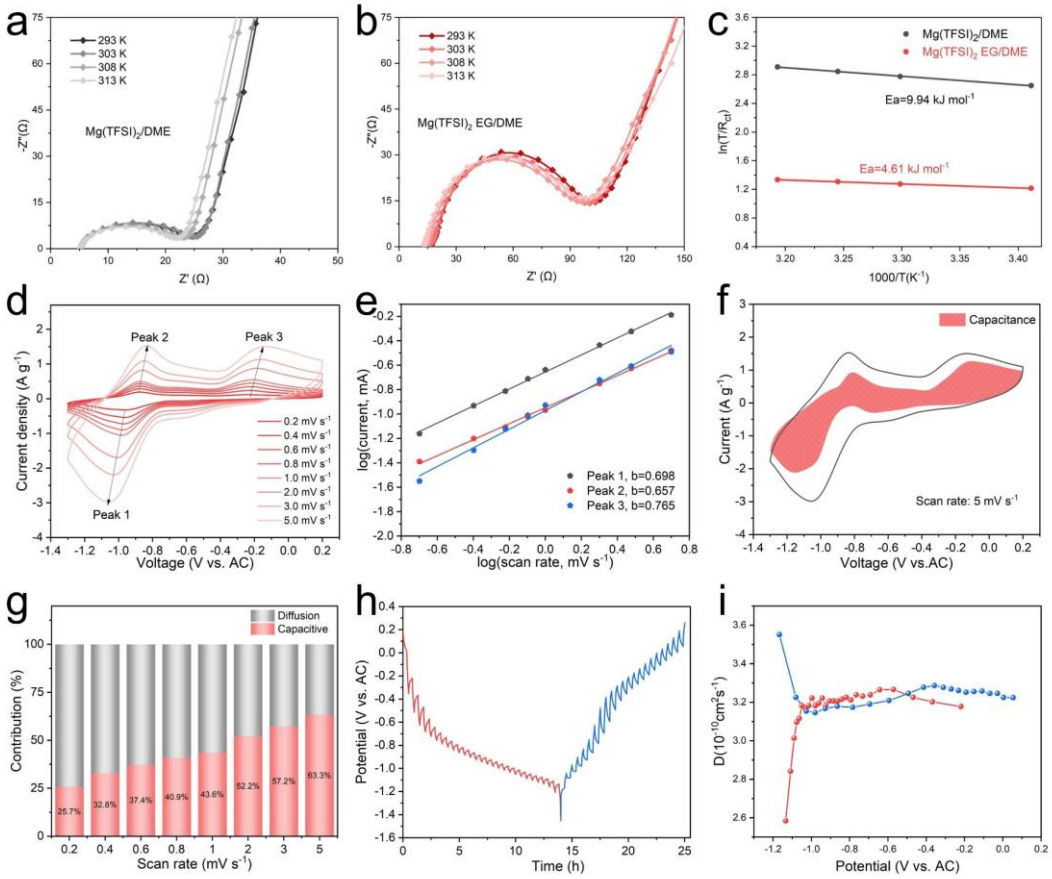

Figure 4.10 Temperature-dependent Nyquist plots of symmetric VO_2//VO_2 cells in (a) $Mg(TFSI)_2$/DME electrolyte and (b) $Mg(TFSI)_2$ EG/DME electrolyte. (c) Desolvation energy of Mg^{2+} derived from Nyquist plots. (d) CV curves of VO_2 in the $Mg(TFSI)_2$ EG/DME electrolyte with increasing scan rates from 0.2 to 5 mV s^{-1}. (e) Log(*i*) versus log(*v*) plots for the redox peaks in (d). (f) Capacitive contribution to the total charge storage at 5 mV s^{-1}. (g) Diffusion and capacitive contributions to charge storage at different scan rates. (h) GITT profile and (i) corresponding Mg^{2+} diffusion coefficient in VO_2.

Table 4.2 The fitting value of R_{ct} with $Mg(TFSI)_2$/DME and $Mg(TFSI)_2$ EG/DME by the simulation of EIS spectra.

Electrolyte	T(K)	293	303	308	313
	1000/T(K^{-1})	3.41	3.30	3.25	3.19
$Mg(TFSI)_2$/DME	R_{ct}(Ω)	20.73	18.90	17.90	17.07

	$\ln(T/R_{ct})$	2.65	2.78	2.85	2.90
$Mg(TFSI)_2$ EG/DME	$R_{ct}(\Omega)$	87.10	84.83	83.48	82.5
	$\ln(T/R_{ct})$	1.21	1.27	1.31	1.33

Then, the electrochemical reaction kinetics of VO_2 cathodes in $Mg(TFSI)_2$ EG/DME electrolyte was investigated through CV scanning at increasing sweeping rates from 0.2 to 5 mV s^{-1} (**Figure 4.10d**). The calculated *b* values were 0.698 for the cathodic peak (peak 1 in **Figure 4.10e**), and 0.657 and 0.765 for the anodic peaks (peak 2 and 3), indicating that the reaction kinetics are governed by both diffusion and capacitive process. Then, the fitted capacitive-controlled charge storage proportion is around 63 % at a high scan rate of 5 mV s^{-1}. Following the similar way, the capacitive contribution ratios were calculated to increase from 26 % at 0.2 mV s^{-1} to 63 % at 5 mV s^{-1} (**Figure 4.10f**). The increased capacitive capacity ratios are favorable for high rate capability of VO_2 cathodes.

The Mg^{2+} diffusion coefficient in VO_2 was calculated to be 2.58×10^{-10} to 3.55×10^{-10} cm^2 s^{-1} by GITT method, which was executed by cycling the cells at a current density of 100 mA g^{-1} for 10 min and resting for 20 min between each step (**Figure 4.10h** and **4.10i**). These values are several folds higher than these in $Mg(TFSI)_2$/EG electrolyte (9.8×10^{-11} to 1.13×10^{-10} cm^2 s^{-1}) and $Mg(TFSI)_2$/DME (3.78×10^{-11} to 4.01×10^{-11} cm^2 s^{-1}, **Figure 4.11**). Such a dramatic difference in Mg^{2+} diffusion kinetics evidences the different electrochemical performance of VO_2 as aforementioned.

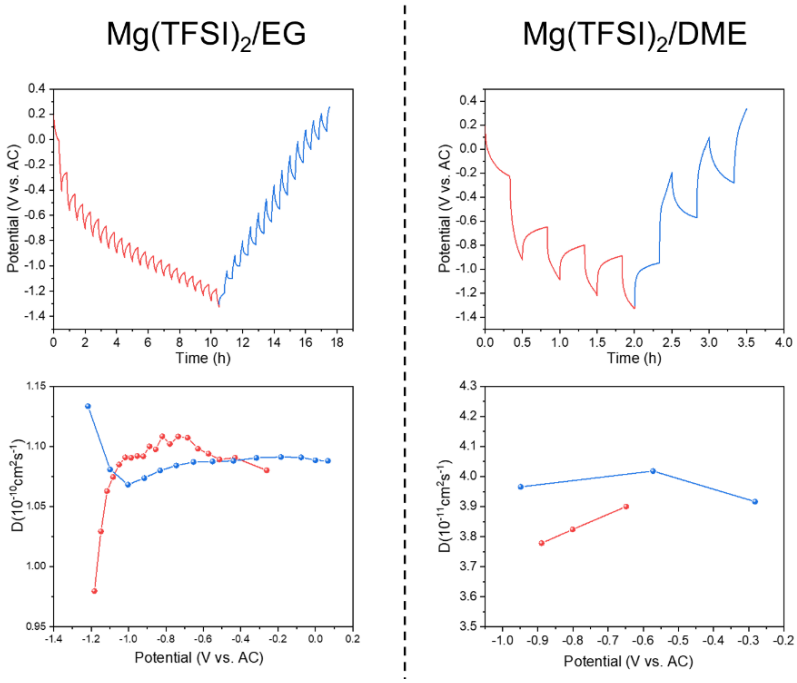

Figure 4.11 GITT profile of VO_2 in Mg(TFSI)2/EG and Mg(TFSI)2/DME electrolytes.

4.2.4 Mg^{2+} storage mechanism within VO_2 cathode

To understand the Mg^{2+} storage mechanism in VO_2 in the $Mg(TFSI)_2$ EG/DME electrolyte, in-situ XRD was conducted (**Figure 4.12a**). Upon discharging to -1.3 V, the XRD peaks at 25.3°, 30.3°, and 45.2°, corresponding to the (110), (111), and (-601) crystal planes, gradually shifted to lower angles, suggesting the intercalation of Mg^{2+} into VO_2 with a solid solution process. When charging back to 0.2 V, these XRD peaks shifted reversibly to their original positions, indicative of excellent structural reversibility of VO_2 cathodes. The lattice parameter changes were also calculated and plotted in **Figure 4.12b**. During discharging, *a* and *c* increased by 2.5% and 1.15%, while *b* decreased by 2.25%, leading to a moderate volume change of approximately 2.57%. The small volume changes are favorable for the long-term cycling stability.

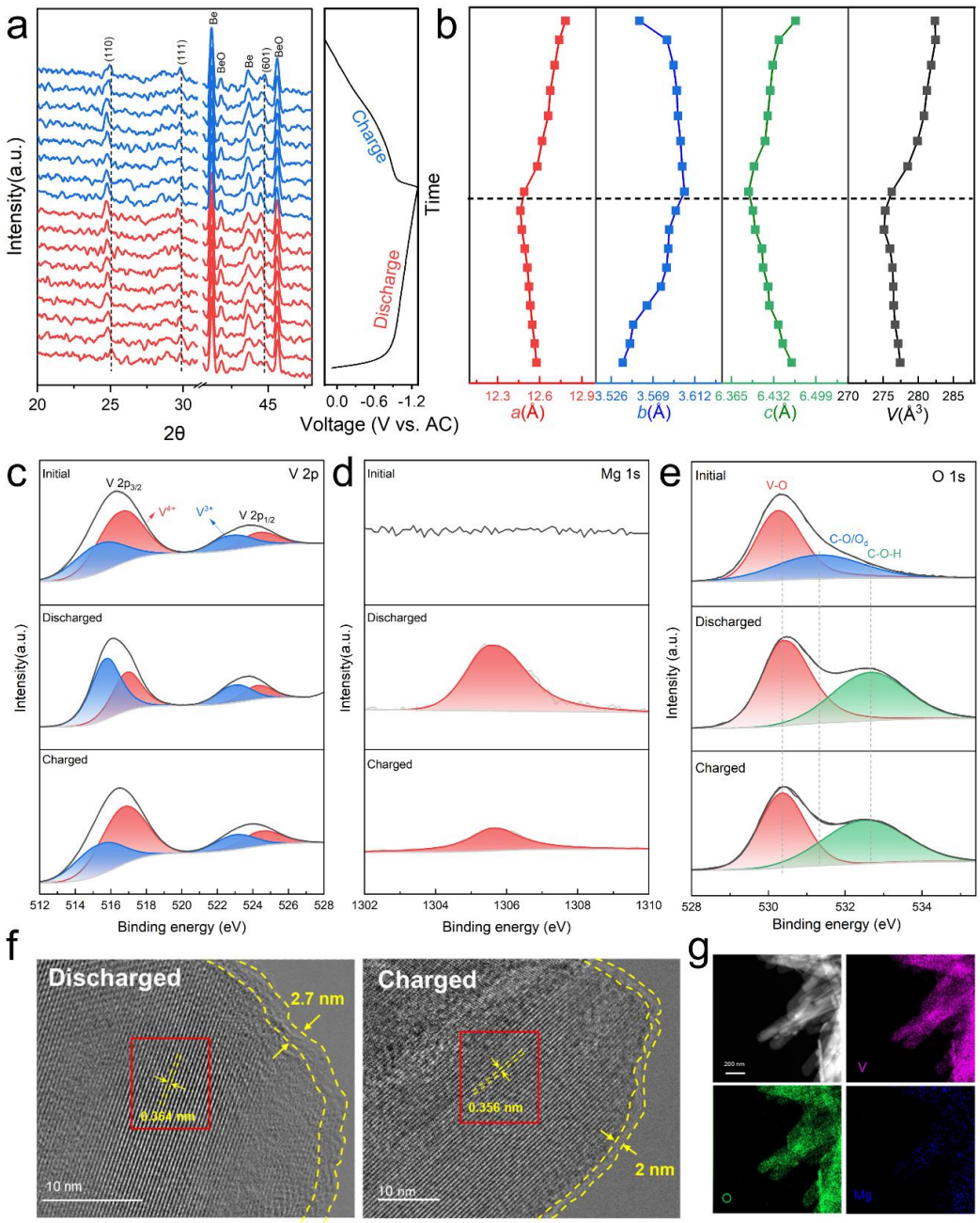

Figure 4.12 (a) In-situ XRD spectra and charge/discharge voltage profiles for VO_2 cathode. (b) Lattice parameter evolution during charge/discharge derived from (a). XPS spectra of (c) V 2p, (d) Mg 1s and (e) O 1s for initial, fully discharged and fully charged VO_2. (f) HRTEM images of VO_2 at fully discharged and charged states. (g) HAADF image and corresponding V, O and Mg mapping of discharged VO_2.

The insertion of Mg^{2+} ions in VO_2 was also confirmed by HRTEM images (**Figure 4.12f**). After the charging process, the interlayer space of (110) decreased to 0.356 nm, consistent with

in-situ XRD results. TEM images of cycled VO_2 nanowires show intact morphologies (**Figure 4.13**), thus demonstrating the stability of VO_2 cycling in the RMB system.

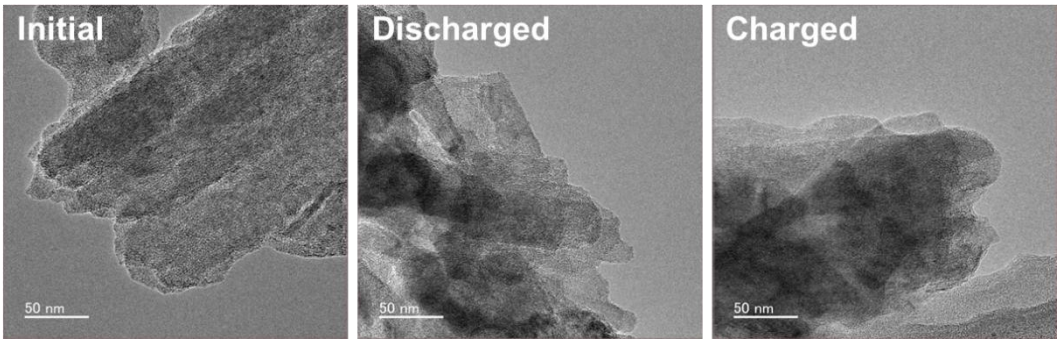

Figure 4.13 TEM image of the VO_2 at different states. After the discharging/charging process, VO_2 retains the nanowire morphology.

The chemical structures of VO_2 after charging and discharging reactions were studied by ex-situ XPS (**Figure 4.12c** to **4.12e**). For pristine VO_2, the V 2p spectrum present two peaks referring to V $2p_{3/2}$ (516.4 eV) and V $2p_{1/2}$ (523.8 eV) [154]. The V $2p_{3/2}$ peak can be deconvoluted into V^{4+} state at 516.8 eV and V^{3+} state at 515.7 eV [55]. The marginal V^{3+} may come from the excessive reduction of VO_2 during material synthesis. For the fully discharged VO_2, the V^{4+} peak weakens along with the strengthen of the V^{3+} peak and the appearance of a strong Mg 1s peak at 1304.5 e. This result indicates the reduction of V^{4+} to V^{3+} during the Mg^{2+} insertion into VO_2 crystals At the charged state, the V^{4+} and V^{3+} peaks mostly returned to original states, and a marginal amount of Mg^{2+} is preserved. The O 1s peak at 532.6 eV corresponding to C-O-H from EG exhibit significantly elevated intensities for dischcarged and charged samples, which imply the involvement of EG derives at the CEI layer. HRTEM images in **Figure 4.12f** present the CEI layers of approximate 2 nm in thickness on the surface of VO_2 particles.

To understand the chemical compositions of the CEI layers formed in these two electrolytes, we conducted in-depth XPS characterizations under different Ar^+ etching time (0, 30, 60, and 120 s). The gradient distribution of C-O-H peaks in the C 1s (286.5 eV) and O 1s (532.6 eV) spectra (**Figure 4.14a**) confirmed the formation of EG-derived compounds [155]. In the S 2p spectra, only a small amount of $TFSI^-$ was detected on the surface, and no relevant

decomposition byproducts were found in subsequent in-depth analysis, suggesting mitigated side effects. Conversely, in $Mg(TFSI)_2$/DME electrolyte (**Figure 4.14b**), the prominent C-O-C peaks in the C 1s (286.4 eV) and O 1s (532.5 eV) is mainly derived from DME-rich solvation, which is detrimental to Mg^{2+} diffusion. Additionally, the increased intensity of the C-F peaks and the emergence of MgF_2 (685.2 eV) and MgS (163.7 eV) peaks suggest extensive decomposition of $TFSI^-$ [91, 156], resulting in a partially Mg^{2+}-blocking layer [38]. A schematic illustration of the CEI layers is depicted in **Figure 4.14c**. In the $Mg(TFSI)_2$/DME electrolyte, the strong solvation structure and anions decomposition result in poor Mg^{2+} storage in VO_2 cathodes, in contrast, the $Mg(TFSI)_2$ EG/DME electrolyte with its weaken solvation and formation of an EG-driven buffer layer, promotes the Mg^{2+} storage performance in VO_2 cathodes.

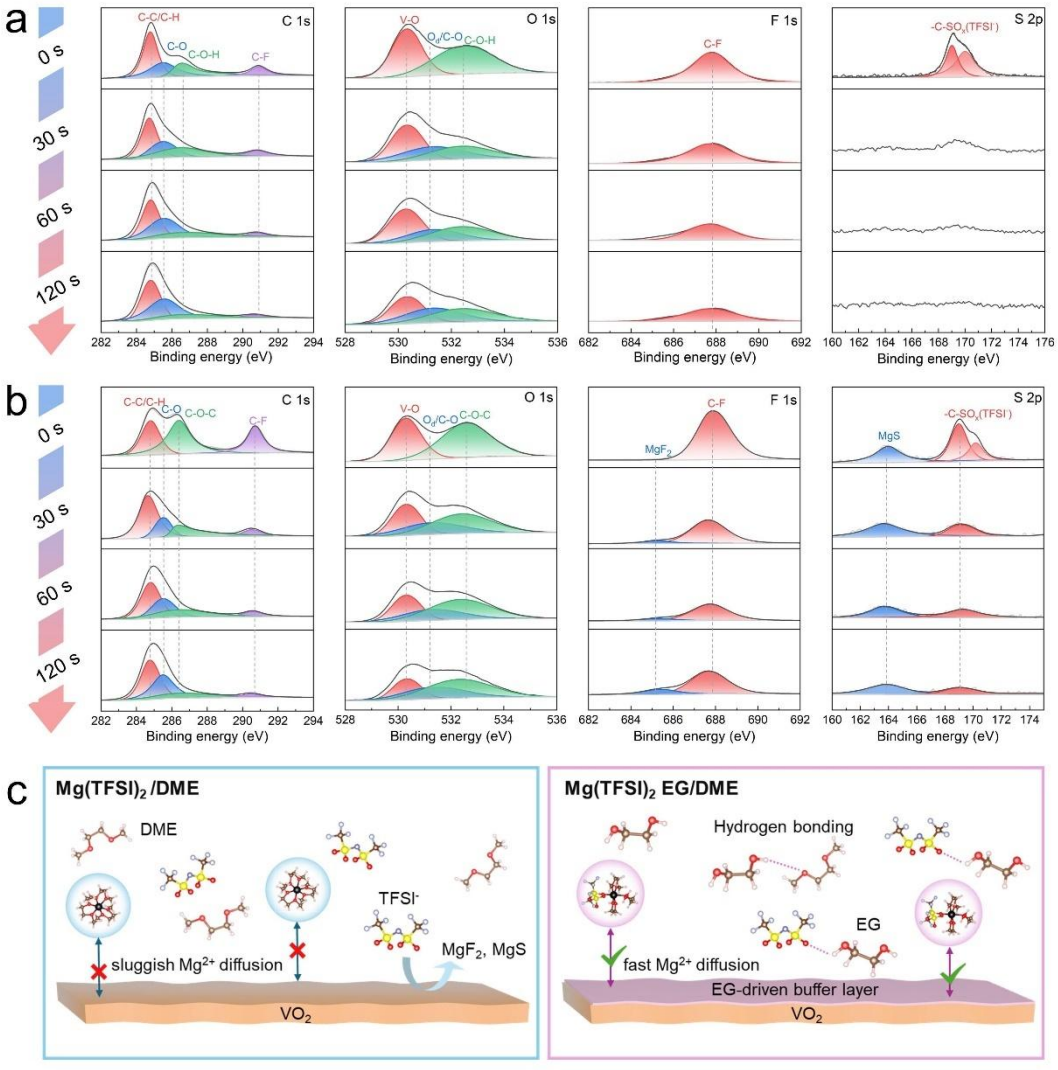

Figure 4.14 (a) In-depth C 1s, O 1s, F 1s, and S 2p XPS spectra for the cycled VO_2 in $Mg(TFSI)_2$ EG/DME electrolyte. (b) In-depth XPS spectra of C 1s O 1s, F 1s, and S 2p for the cycled VO_2 in $Mg(TFSI)_2$/DME. (c) Schematic illusitration of Mg^{2+} diffusion behaviors at the cathode-electrolyte interface in VO_2 cathode using $Mg(TFSI)_2$/DME (left) and $Mg(TFSI)_2$ EG/DME (right) electrolytes.

4.2.5 Full cell application

Finally, to verify the compatibility of $Mg(TFSI)_2$ EG/DME electrolyte with Mg metal anodes, we assembled a Mg//Mg symmetric cell and cycled it at a current density of 0.1 mA cm^{-2}. As shown in **Figure 4.15**, in $Mg(TFSI)_2$/DME electrolyte, the Mg//Mg symmetrical cell exhibited a large overpotential (~2 V) for Mg stripping/plating. In contrast, the overpotentials in the co-solvent electrolyte was significantly suppressed to lower than 0.2 V, allowing for stable operation up to 120 h with the absence of soft circuits (**Figure 4.16**).

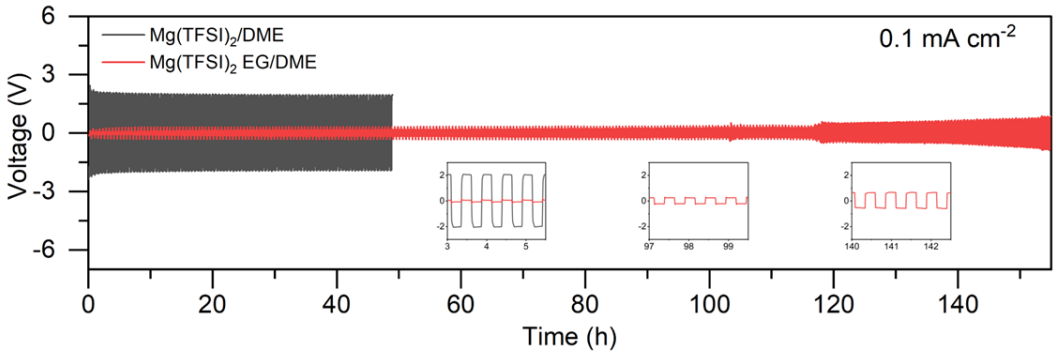

Figure 4.15 Mg//Mg symmetric cells with $Mg(TFSI)_2$/DME and $Mg(TFSI)_2$ EG/DME electrolytes at 0.1 mA cm^{-2}.

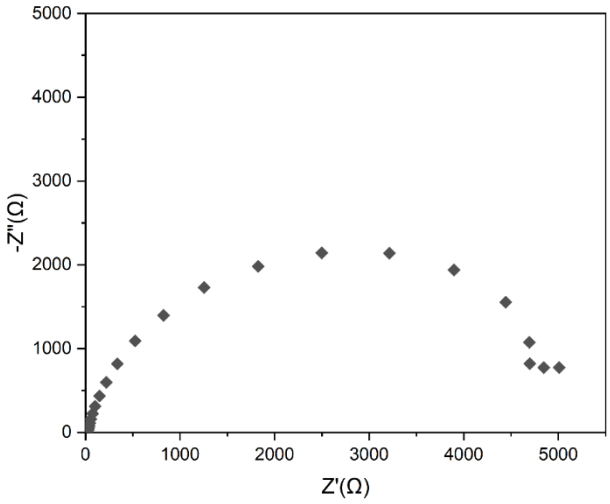

Figure 4.16 Nyquist plot of the Mg//Mg symmetric cell in $Mg(TFSI)_2$ EG/DME electrolyte after cycling at 0.1 mA cm^{-2}.

SEM images of the cycled Mg metal electrode in these electrolytes revealed notable differences (**Figure 4.17**). The Mg metal cycled in $Mg(TFSI)_2$/DME displayed large-area cracks on its surface. Conversely, the Mg metal cycled in $Mg(TFSI)_2$ EG/DME appeared much smoother, with only minor pitting marks from the cation stripping process. Even after 120 h cycling (**Figure 4.18**), the Mg surface remains dendrite-free with discernible stripping trances.

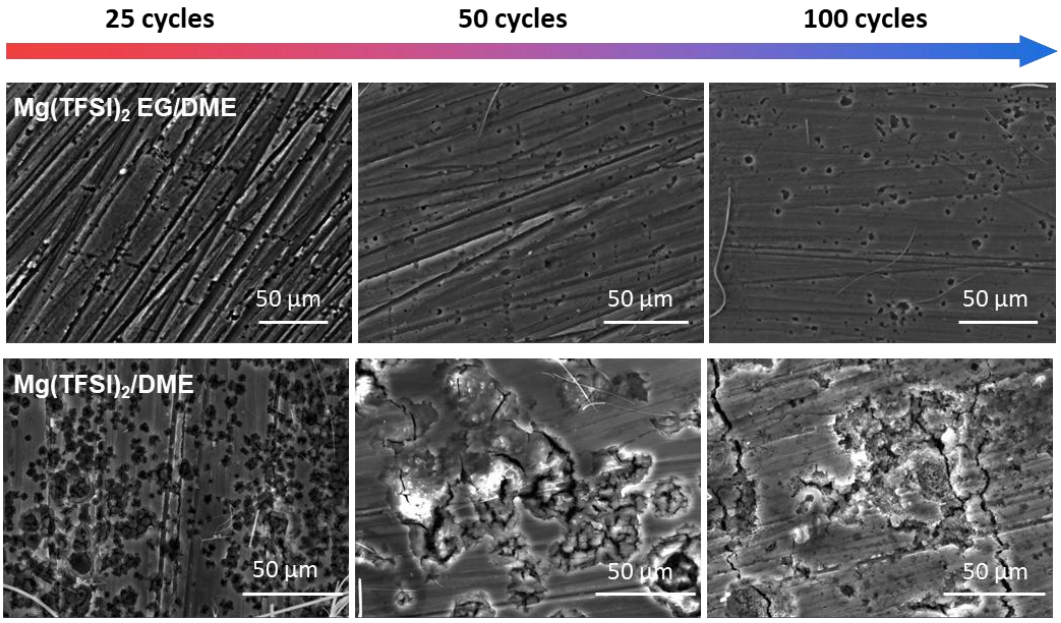

Figure 4.17 SEM images of Mg anodes cycled at a current density of 0.1 $mAcm^{-2}$ in various electrolytes.

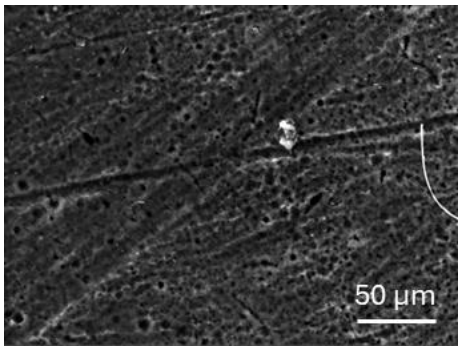

Figure 4.18 SEM image of a Mg anode after 120 hours of cycling at a current density of 0.1 mA cm^{-2} in $Mg(TFSI)_2$ EG/DME electrolyte.

To investigate the SEI on the surface of cycled Mg metal anodes, EDX and XPS analyses were conducted. **Figure 4.19** shows that the cycled Mg metal in $Mg(TFSI)_2$/DME electrolyte exhibits more decomposition products than these in $Mg(TFSI)_2$ EG/DME electrolyte.

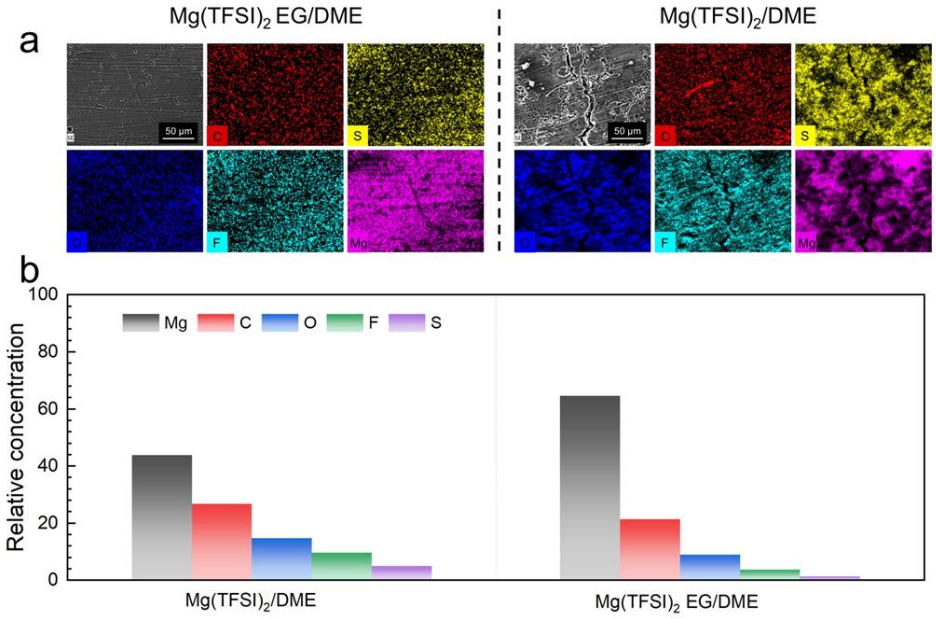

Figure 4.19 (a) EDS mapping and (b) corresponding molar percentage of SEI species on the surface of cycled Mg surface in $Mg(TFSI)_2$/DME and $Mg(TFSI)_2$ EG/DME electrolytes.

The XPS results in **Figure 4.20** demonstrate that the SEI layer drived from $Mg(TFSI)_2$/DME electrolyte contains significant amounts of MgF_2 and MgS, which are passive components [156, 157]. In contrast, the corresponding XPS peaks are significantly weaker in the SEI layers derived from the $Mg(TFSI)_2$ EG/DME electrolyte. Furthermore, the Mg deposition

was confirmed in Mg//SS asymmetric cells (**Figure 4.21**). CV tests reveal distinctive redox peaks for Mg plating/tripping reactions. SEM, TEM and XPS analyses of the plated electrodes also demonstrate the deposition of Mg metal nanoparticles on SS current collectors (**Figure 4.22**).

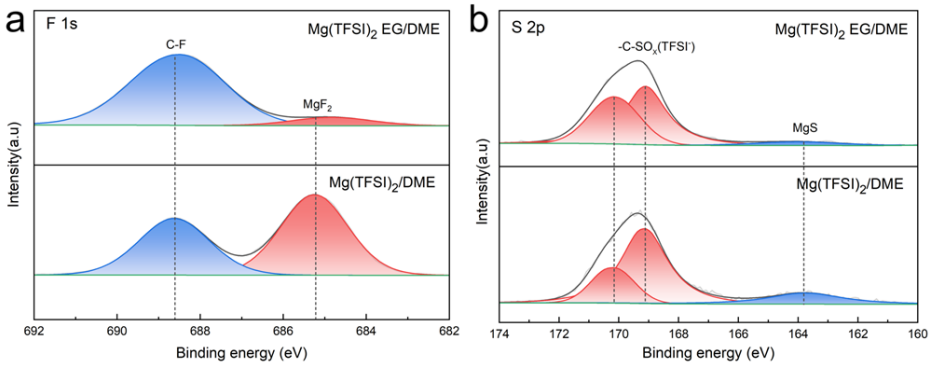

Figure 4.20 (a) F 1s and (b) S 2p XPS results on the cycled Mg anodes in $Mg(TFSI)_2$/DME (bottom) and $Mg(TFSI)_2$ EG/DME (top) electrolytes.

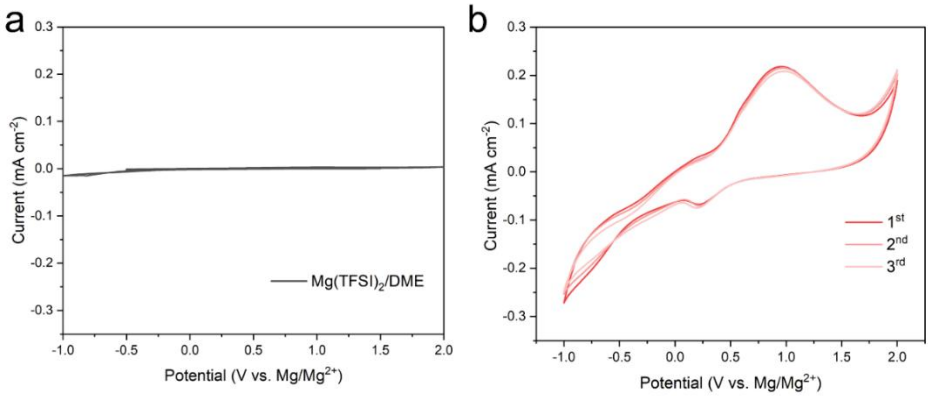

Figure 4.21 CV curves of the Mg//SS asymmetric cell in (a) $Mg(TFSI)_2$/DME and (b) $Mg(TFSI)_2$ EG/DME electrolyte at a scanning rate of 25 mV s^{-1}.

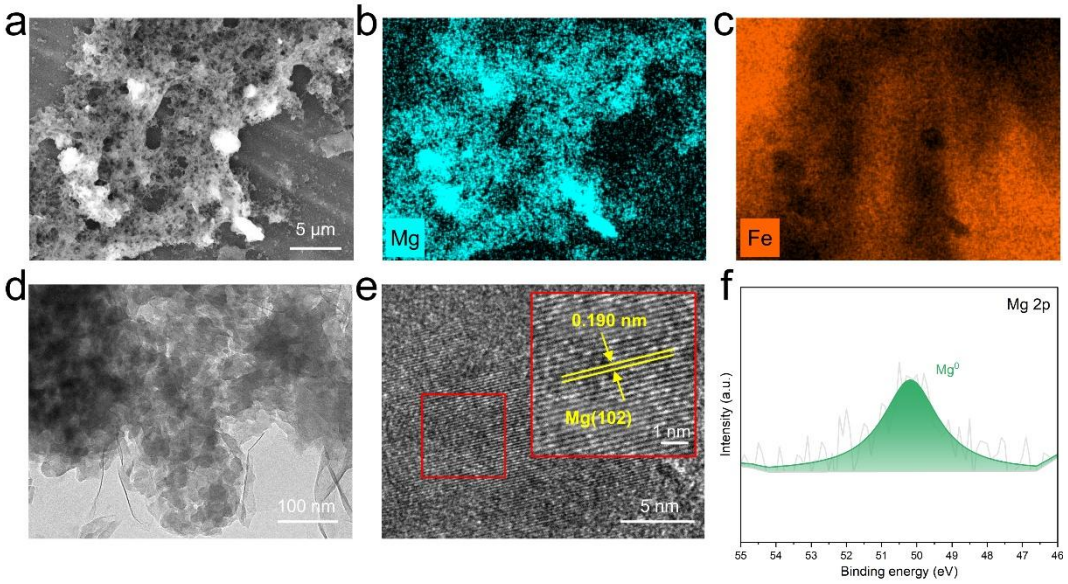

Figure 4.22 The morphology and composition of Mg deposits on SS substrate. (a) SEM image and corresponding EDS elemental mapping of (b) Mg and (c) Fe. (d) TEM, (e) HRTEM images, and (f) Mg 2p XPS spectrum of Mg electrodeposits.

The practical feasibility of $Mg(TFSI)_2$ EG/DME electrolyte is demonstrated in full cells containing Mg metal anodes and VO_2 cathodes in the $Mg(TFSI)_2$ EG/DME electrolyte (**Figure 4.23a**). The Mg//VO_2 full cell exhibited an initial charge capacity of 283.6 mAh g^{-1} (**Figure 4.23b**) and retained a capacity over 160 mAh g^{-1} after 50 cycles (**Figure 4.23c**). Under an increased active material mass loading of 2 mg cm^{-2}, the Mg//VO_2 full cell delivered high capacities of 182.9 mAh g^{-1} and 113 mAh g^{-1} at the 1st and 30th cycles (**Figure 4.24**). The electrochemical performance in the hybrid electrolyte is competitive when comparing with previously reported RMBs using $Mg(TFSI)_2$-based electrolytes (**Table 4.3**), underscoring the effectiveness of our EG/DME hybrid electrolyte in advancing Mg metal batteries.

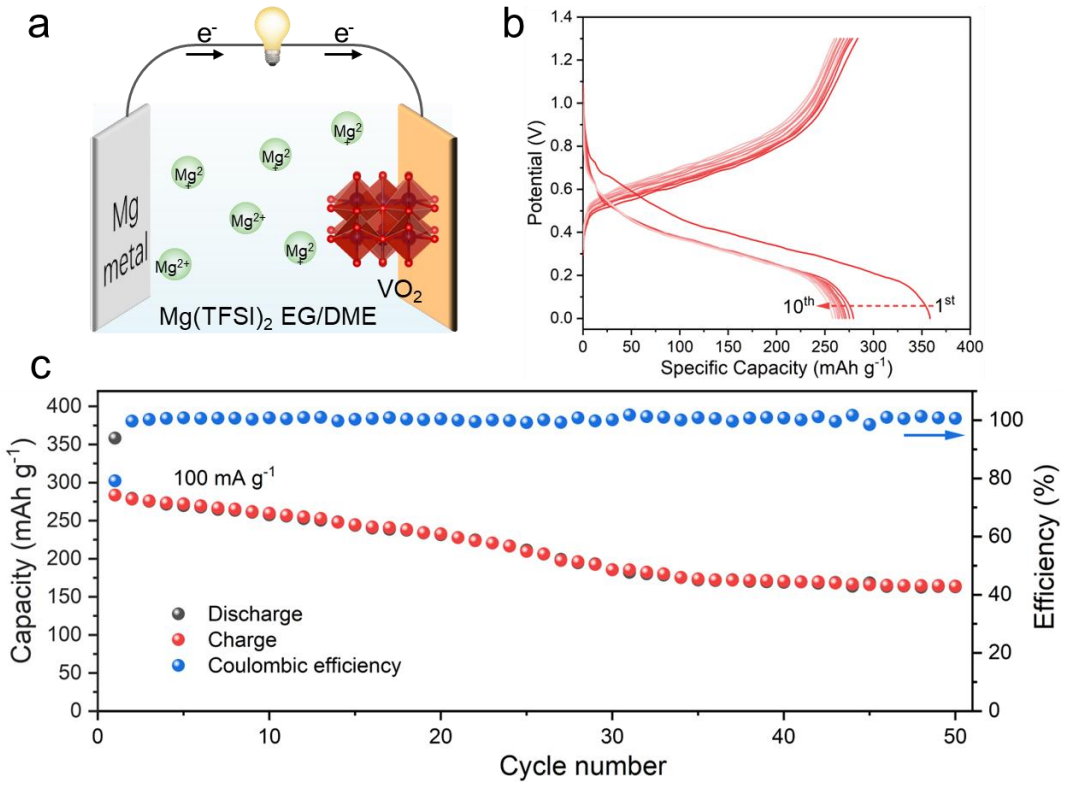

Figure 4.23 (a) Schematic representation of the Mg//VO_2 full cell. (b) GCD curves during the initial 10 cycles. (c) Cyclic performance and Coulombic efficiencies at 100 mA g^{-1}.

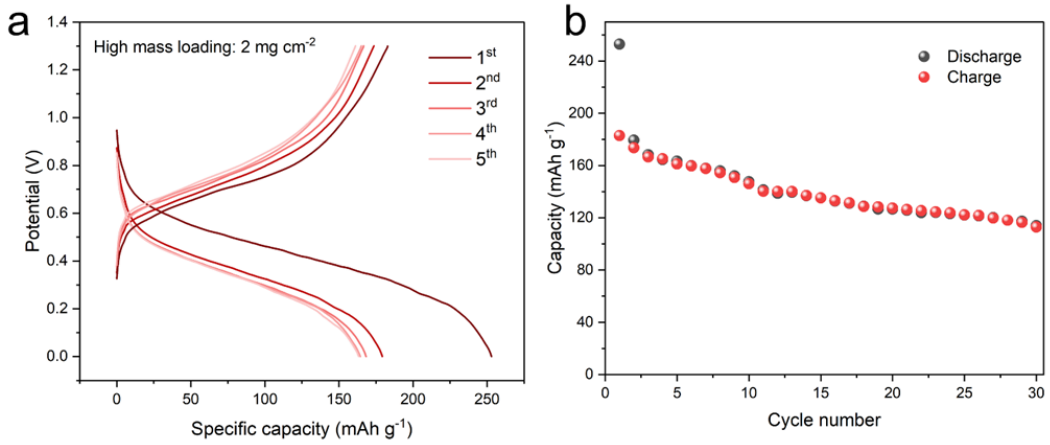

Figure 4.24 Electrochemical performance of Mg//VO_2 full cells in the cosolvent electrolyte with high cathode mass loading of 2 mg cm^{-2}. (a) GCD curves for the initial 5 cycles and (b) corresponding cycling capacity at 100 mA g^{-1}.

Table 4.3 Comparison of the electrochemical performance of Mg metal full cells using chloride-free electrolytes.

Electrolyte formula	Cell type	Cell performance	Capacity retention	Ref
$Mg(TFSI)_2$ EG/DME	**Mg//VO_2**	**283.6 mAh g^{-1}@100 mA g^{-1}**	**163.0 mAh g^{-1} after 50 cycles**	**This work**
$Mg(CF_3SO_3)_2$/PC+H_2O	Mg//V_2O_5	235 mAh g^{-1}@100 mA g^{-1}	58 mAh g^{-1} after 40 cycles	[140]
$Mg(TFSI)_2$/DME +TMP	Mg//Mo_6S_8	115 mAh g^{-1}@20 mA g^{-1}	45 mAh g^{-1} after 50 cycles	[42]
$Mg(TFSI)_2$/DME	Mg//$MgMn_2O_4$	158.2 mAh g^{-1}@10 mAg^{-1}	-	[158]
$Mg(TFSI)_2$/DME+H_2O	Mg//$Na_5V(PO_4)_2F_2$	145 mAh g^{-1}@5 mAg^{-1}	-	[159]
$Mg(TFSI)_2$/$PY_{14}TFSI$	Mg//ζ-V_2O_5	141 mAh g^{-1}@0.05C	122.8 mAh g^{-1} after 15 cycles	[160]
$Mg(TFSI)_2$/triglyme	Mg//$Mg(Mg_{0.3}{}_3V_{1.57}Nix_{0.1})O_4$	145 mAh g^{-1}@5 mA g^{-1}	140.7 mAh g^{-1} after 15 cycles	[161]

4.3 Summary

In summary, we present a glycol-glyme hybrid electrolyte containing EG/DME $Mg(TFSI)_2$ with EG-rich solvation sheath and hydrogen bond networks for high-performance RMBs. The hydroxyl-rich EG molecules play a pivotal role in regulating the solvation structure of Mg^{2+}, while simultaneously forming hydrogen bond networks with DME molecules and $TFSI^-$ anions, thereby significantly enhancing Mg^{2+} diffusion and mitigating potential passivation to VO_2 cathode. Consequently, VO_2 cathode achieved a specific capacity of 258 mAh g^{-1} with outstanding stability over 2000 cycles. Moreover, Mg//VO_2 full cells maintained over 160 mAh g^{-1} after 50 cycles. This study paves the way for the development of low-cost organic electrolytes in multivalent batteries, contributing to enhanced sustainability in energy storage systems.

Chapter 5 A sulfolane-based hydrated eutectic electrolyte inhibits cathode dissolution for ultra-stable aqueous magnesium ion batteries

5.1 Introduction

To address fossil fuel depletion and achieve carbon neutrality, aqueous magnesium-ion batteries (AMIBs) are being developed as a safer, more cost-effective, and sustainable electrochemical energy storage technology due to their use of abundant magnesium resources and high ionic conductivity of aqueous electrolytes.[10, 55, 61]. Generally, the energy density of AMIBs largely depends on the capacity and working potential of the cathode materials. Up to now, only a handful of cathode materials have been reported, including Chevrel phase Mo_6S_8 [43, 49], Prussian blue analogues [58, 89], layered transition metal oxides/sulfur [55, 162, 163], and organic electrodes [59, 89]. Among these, orthorhombic V_2O_5 stands out due to its layered structure and inherent structural flexibility, which together facilitate improved Mg^{2+} diffusion kinetics and enhanced stability compared to other vanadium-based cathodes such as VO_2. As a result, V_2O_5 exhibits a high capacity (exceeding 300 mAh g^{-1}), elevated operating voltage, and superior structural stability. [164-166]. However, V_2O_5 suffers from inevitable vanadium dissolution in aqueous electrolytes during charge/discharge process, leading to irreversible structural collapse and capacity loss. This dissolution primarily arises from the attack of water molecules ($V_2O_5 + 3H_2O \rightarrow 2VO_2(OH)_2 + 2H^+$) at the CEI [167-169]. The highly active water molecules readily adsorb onto the V_2O_5 surface, where they can reversibly interact with the vanadium oxide lattice and induce surface charged. Subsequently, additional H_2O molecules attracted by this charged layer attack the lattice, causing the irreversible detachment of vanadium oxide units and initiating continuous dissolution cycles that finally destabilize vanadium complexes. During electrochemical cycling, the intensified charge exchange further accelerates cathode degradation by facilitating additional H_2O intercalation, which aggravates the instability of

V_2O_5 cathode. Consequently, reducing water activity and restricting its interaction with the cathode are critical for improving interfacial stability and mitigating V_2O_5 dissolution.

To address this challenge, numerous electrolyte optimization strategies have been developed for AMIBs, including water-in-salt electrolytes (WISEs) [58], hydrated eutectic electrolytes (HEEs) [59, 60], and organic/water hybrid electrolytes [54, 61]. Of these efforts, HEEs are particularly notable by virtue of their low cost, ease of synthesis, and high ionic conductivity. In HEEs, the water content originates entirely from the crystal water in the metallic salts, which inherently reduces free water activity. Additionally, the Lewis acid-base reactions and intermolecular hydrogen bond interactions within HEEs significantly modify the water-dominated solvation structure and disrupt hydrogen bonding network among water molecules. This unconditionally restricts water activity and enhances interfacial stability [170-172].

State-of-the-art amide-based HEEs, such as $Mg(NO_3)_2 \cdot 6H_2O$/acetamide [59] and $MgCl_6 \cdot 6H_2O$/acetamide/urea [60], have demonstrated their compatibility with several electrodes through rational design for the bulk electrolytes. Despite these advancements, exploration beyond amide-based hydrated eutectic systems remains limited. Additionally, the lack of comprehensive studies on the electrode-electrolyte interface hingers the establishment of systematic guidance for the practical implementation of subsequent hydrated eutectic systems.

In this study, we developed a novel sulfolane (SL) -based hydrated eutectic system by combining SL with $Mg(ClO_4)_2 \cdot 6H_2O$, aiming to achieve comprehensive improvements from bulk electrolyte to electrode interface and thereby enhance the performance of V_2O_5 cathode in AMIBs. Compared to other salts, $Mg(ClO_4)_2 \cdot 6H_2O$ offers several advantages, including low cost, high stability against moisture and air, non-toxicity, and good solubility. Additionally, its inherent crystal water promotes intermolecular hydrogen bonding with SL, further improving electrolyte performance. In bulk electrolyte, SL forms stronger hydrogen bonds with water molecules, displacing the initial hydrogen bonding network among water molecules and

effectively suppressing water activity. Additionally, its involvement in the solvation structure facilitates Mg^{2+} de-solvation and minimizes the content of interfacial bound water. When it comes to the CEI, the preferential adsorption of sulfolane effectively blocks water molecules from attacking the V_2O_5 cathode (**Figure 5.1a**). Through this integrated strategy, the sulfolane-based HEE exhibits superior compatibility with V_2O_5 cathode, realizing a high capacity of 322.7 mAh g^{-1} at 50 mA g^{-1} and exceptional cycling stability over 5000 cycles with a minimal capacity degradation rate of 0.0061% per cycle at 1000 mA g^{-1}. Furthermore, leveraging this advancement, a full PTCDA//V_2O_5 battery with the HEE demonstrates a remarkable discharge capacity of 252.3 mAh g^{-1} at 50 mA g^{-1} and a capacity exceeding 190 mAh g^{-1} for over 200 cycles. This electrolyte offers new insights into designing high-energy and high-stable aqueous multivalent batteries.

5.2 Results and discussion

5.2.1 V_2O_5 cathode dissolution behavior in hydrated eutectic electrolytes

To directly observe dissolution behavior of V_2O_5 cathode in the two different electrolytes, we conducted immersion experiments. As depicted in **Figure 5.1b**, the 1 M $Mg(ClO_4)_2$ aqueous electrolyte (marked as AE) quickly turns yellow, indicating the gradual dissolution of V_2O_5 in water. This color change visually confirms the presence of dissolved vanadium species. To quantify this dissolution, we performed inductively coupled plasma-optical emission spectrometer (ICP-OES) tests, which shows a nearly linear increase in vanadium concentration with immersion time (**Figure 5.1c**).

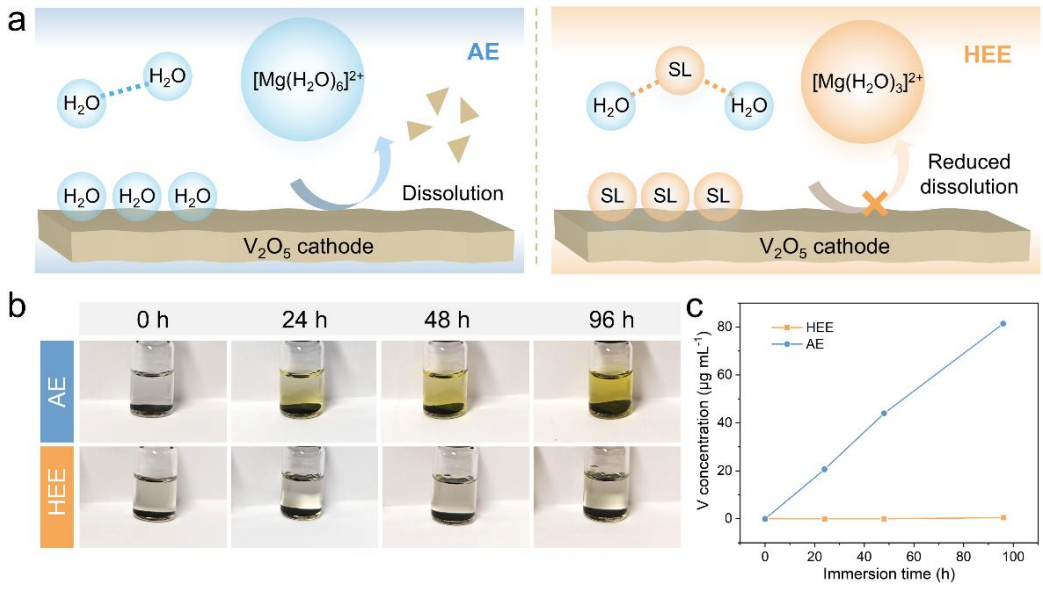

Figure 5.1 (a) Schematic illustration of hydrated eutectic electrolyte strategy. (b) Optical photos of V_2O_5 immersed in two electrolytes with different immersion times and (c) the corresponding ICP-OES results of electrolytes with V_2O_5.

SEM and EDS mapping further reveal changes in V_2O_5 cathode's morphology and element distribution. XRD pattern in **Figure 5.2a** indexed the V_2O_5 to an orthorhombic phase with lattice parameters of a = 11.48 Å, b = 4.36 Å, c = 3.55 Å, and $\alpha = \beta = \gamma = 90°$ in the $Pmn2_1$ space group. Initially, the cathode displays an irregular rod-like structure with dimensions of 250~750 nm in length and 75~120 nm in diameter (**Figure 5.2b**). However, due to vanadium dissolution in aqueous electrolyte, the surface becomes blurred and collapsed (**Figure 5.3 and Figure 5.4**), with the rod-like morphology almost disappearing after two weeks immersion (**Figure 5.7**).

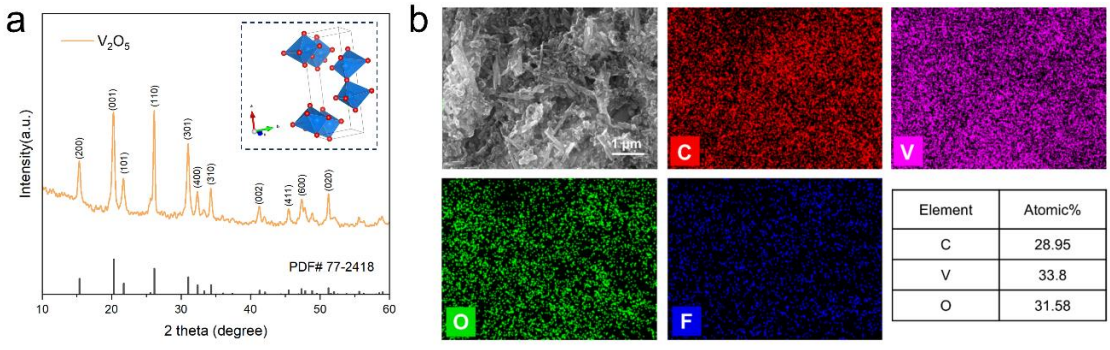

Figure 5.2 (a) XRD pattern and crystal structure (inset) of V_2O_5. (b) SEM image with EDS

elemental mapping of the pristine V_2O_5 cathode.

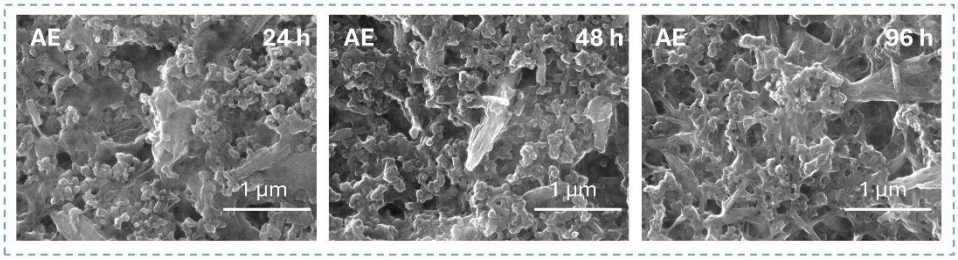

Figure 5.3 SEM images of V_2O_5 cathodes using 1 M $Mg(ClO_4)_2$ aqueous electrolyte with different immersion times.

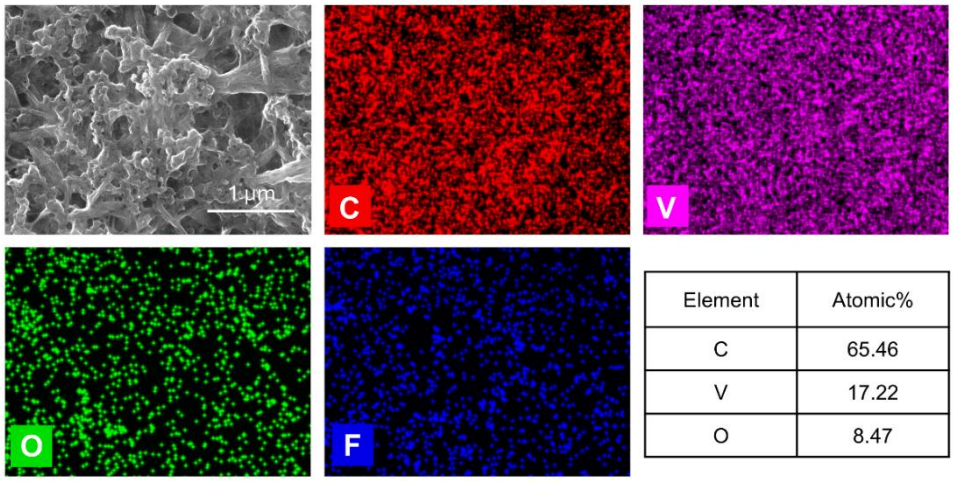

Element	Atomic%
C	65.46
V	17.22
O	8.47

Figure 5.4 SEM image and corresponding EDS mapping for V_2O_5 cathode dissolved in aqueous electrolyte for 96 h.

In contrast, the $Mg(ClO_4)_2 \cdot 6H_2O$/sulfolane hydrated eutectic electrolyte (marked as HEE) ($n_{Mg(ClO4)2 \cdot 6H2O}$: $n_{sulfolane}$ =1:8) remained transparent with no significant color change after 96 h. The corresponding ICP-OES results confirm negligible vanadium presence in the solution. SEM images show that V_2O_5 cathode retains its rod-like structure (**Figure 5.5**, **Figure 5.6**, and **Figure 5.7**), demonstrating the effectiveness of the proposed hydrated eutectic electrolyte in inhibiting the dissolution of V_2O_5 cathode.

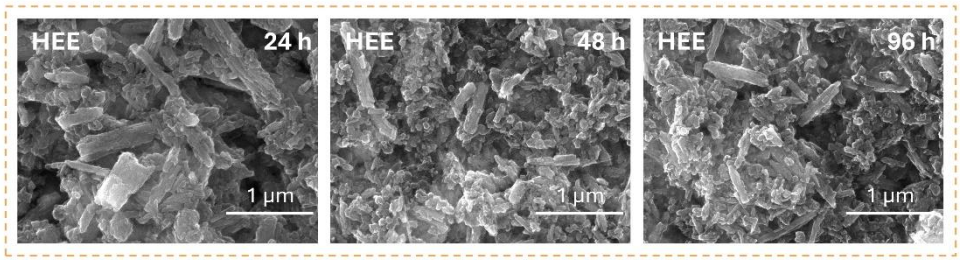

Figure 5.5 SEM images of V_2O_5 cathodes using $Mg(ClO_4)_2 \cdot 6H_2O$/sulfolane hydrated eutectic electrolyte with different immersion times.

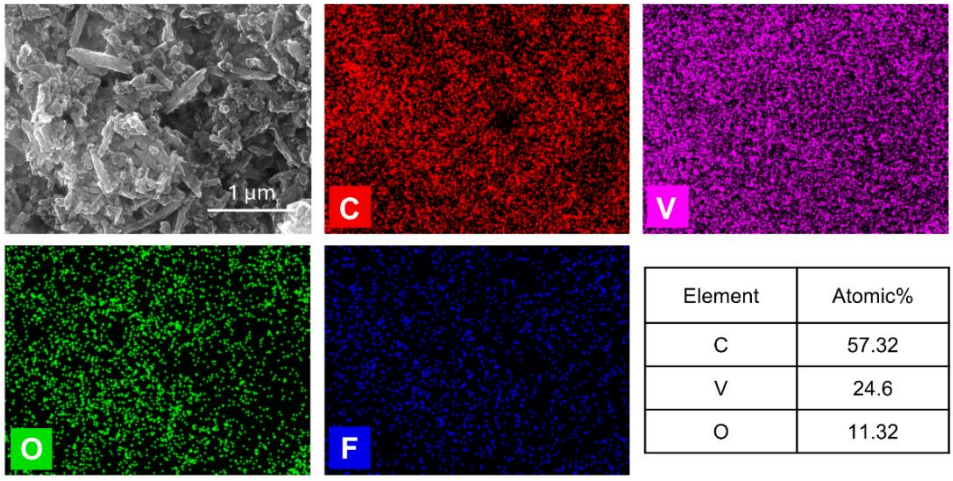

Element	Atomic%
C	57.32
V	24.6
O	11.32

Figure 5.6 SEM image and corresponding EDS mapping for V_2O_5 cathode dissolved in hydrated eutectic electrolyte for 96 h.

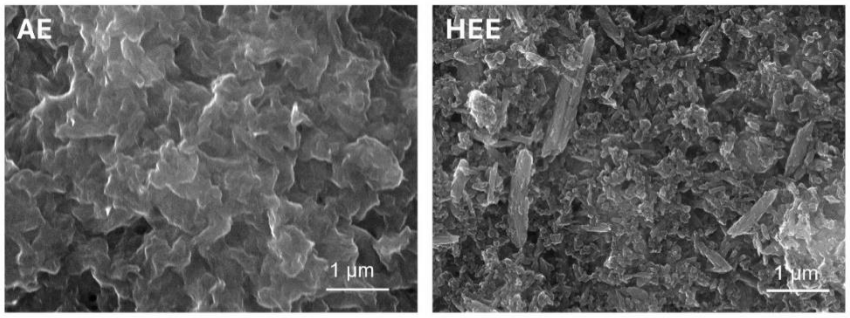

Figure 5.7 SEM images of V_2O_5 cathode after immersing with AE and HEE for two weeks.

5.2.2 Electrochemical performance of V_2O_5 cathode in hydrated eutectic electrolytes

To verify the practicality of the hydrated eutectic strategy in mitigating capacity loss from electrode dissolution, we conducted an open-circuit voltage (OCV) static test at a low current density of 100 mA g^{-1} using a Mg-ion half-cell configuration with V_2O_5 cathodes and AC as the counter electrode. AC was chosen for its high specific surface area and electrochemical

inertness in Mg-ion electrolytes [89, 145], minimizing potential side reactions on the anode side. After fully charging the battery, it was left in an open circuit state for 72 hours, and the recoverable capacity was measured. The observed discharge capacity reduction during this period can be mainly attributed to structural damages from vanadium dissolution [168, 173]. As shown in **Figure 5.8a** and **5.8b**, the Coulombic efficiency after 72 hours is only 58.9% in aqueous electrolyte, compared to 98.8% in hydrated eutectic electrolyte. Especially, the aqueous electrolyte causes a noticeable yellow stain on the glass fiber, indicating vanadium' dissolution, while hydrated eutectic electrolyte shows no such change, suggesting its dissolution inhibition capability. Overall, these findings confirm that the hydrated eutectic electrolyte offers superior resistance to self-discharge, supporting our previous hypotheses.

To further investigate differences in electrochemical performance of these two electrolytes, CV measurements were conducted at a scan rate of 0.5 mV s^{-1} to evaluate Mg-ion intercalation/deintercalation behavior in a voltage window of −1 to 1 V versus AC, equivalent to 1.4 to 3.4 V versus Mg^{2+}/Mg [70, 89]. **Figure 5.8c** shows that the initial CV curve of V_2O_5 cathode in aqueous electrolyte has a higher current response with multiple redox peaks (two reduction peaks at -0.47 V and -0.5 V, three oxidation peaks at -0.35 V, 0.02 V and 0.47 V, respectively). However, due to severe vanadium dissolution, these peaks shift leftward in subsequent scans, with an obvious decrease in current density, implying significant irreversibility (**Figure 5.8d**). Conversely, V_2O_5 cathode in hydrated eutectic electrolyte exhibits stable cycling performance. V_2O_5 exhibits one reduction peak at -0.45 V and one oxidation peak at 0.09 V in the initial CV cycle, which is related to the successful Mg^{2+} intercalation and deintercalation respectively. In the following ten cycles, all peaks appear to be completely overlapped (**Figure5.8e**), indicating excellent reversibility.

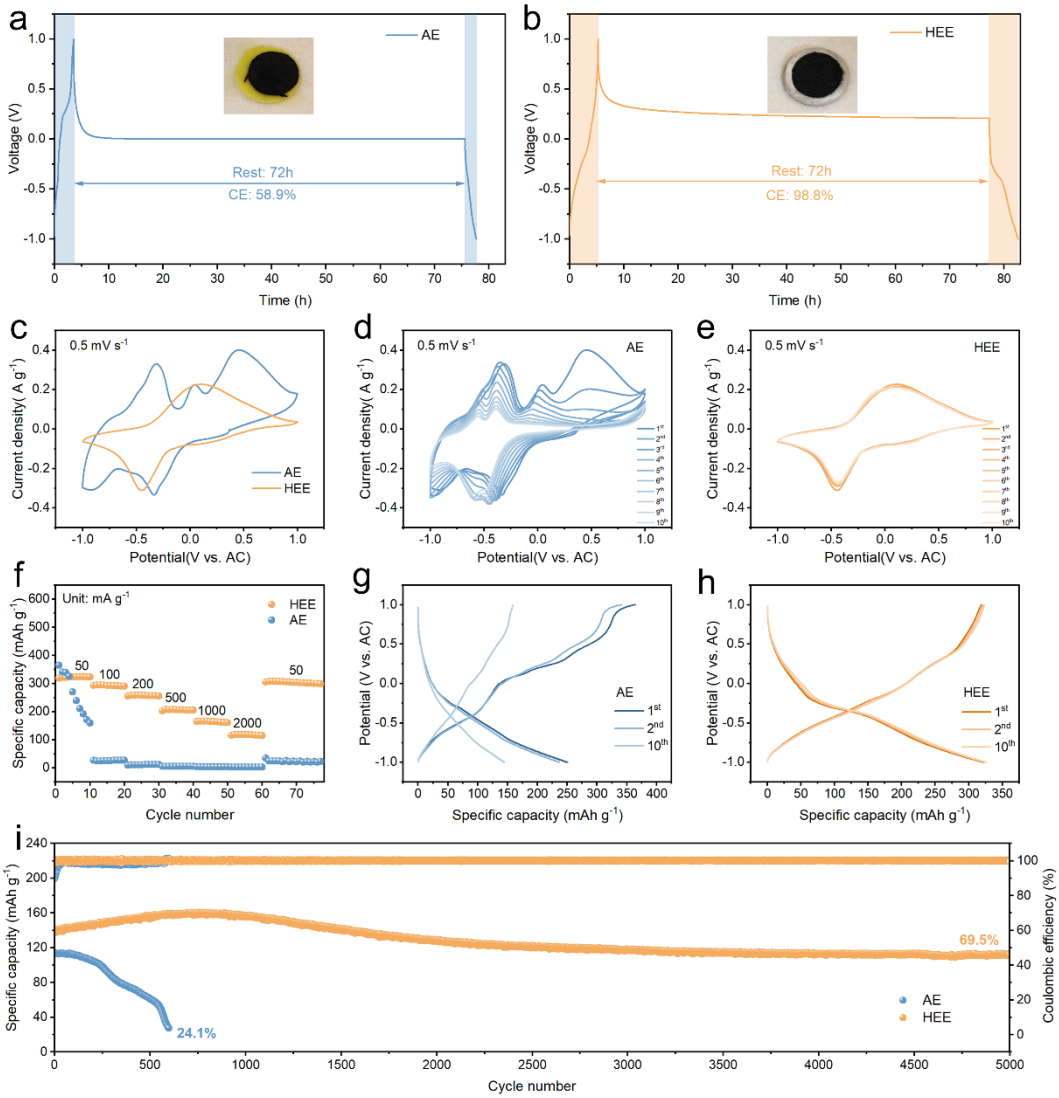

Figure 5.8 Self-discharging test at full charged state in (a) AE and (b) HEE. (c) The initial CV curves for V_2O_5 cathode in different electrolytes. The 1st to 10th cycles of CV curves for V_2O_5 cathode in (d) AE and (e) HEE. (f) Rate capability of V_2O_5 cathode in different electrolytes, and the corresponding voltage-capacity curves at 50 mA g^{-1} in (g) AE and (h) HEE. (i) Long cycling stability of V_2O_5 cathode in different electrolyte solutions at 1000 mA g^{-1}.

Superior rate performance is observed for the HEE at multiple current densities. As shown in **Figure 5.8f** to **5.8h**, V_2O_5 with hydrated eutectic electrolyte delivers average specific capacities of 322.7, 292.8, 257.3, 206.3, 164.5, and 117.6 mAh g^{-1} at current densities of 50, 100, 200, 500, 1000, and 2000 mA g^{-1}, respectively. Notably, when the current density returns to 50 mA g^{-1}, the cathode maintains a high specific capacity of 306.3 mAh g^{-1}, indicating

excellent capacity retention. In contrast, V_2O_5 with aqueous electrolyte initially achieves a slightly higher capacity of 364.2 mAh g^{-1} at 50 mA g^{-1} due to water intercalation [55, 155]. However, the dissolution reactions between the aqueous solution and vanadium species led to a significant loss of active material, resulting in only 43.8% capacity retention after 10 cycles (**Figure 5.8g**). Additionally, the capacity declines sharply with increasing current density, highlighting poor compatibility between V_2O_5 cathode and aqueous electrolyte. To investigate the different dissolution behavior in the electrochemical process, V_2O_5 electrodes at different discharge states were extracted from coin cells and immersed in their respective electrolytes for several hours. As shown in **Figure 5.9**, in aqueous electrolyte, both half-discharged and full-charged electrodes yield a light-yellow solution, indicating dissolution of electrode products, the corresponding SEM images reveal significant morphological collapses, consistent with the abovementioned dissolution effect. In contrast, electrodes at the same states in hydrated eutectic electrolytes result in transparent solutions and retain well-preserved nanorods morphology in SEM images, demonstrating the superior anti-dissolution capability of the hydrated eutectic electrolyte.

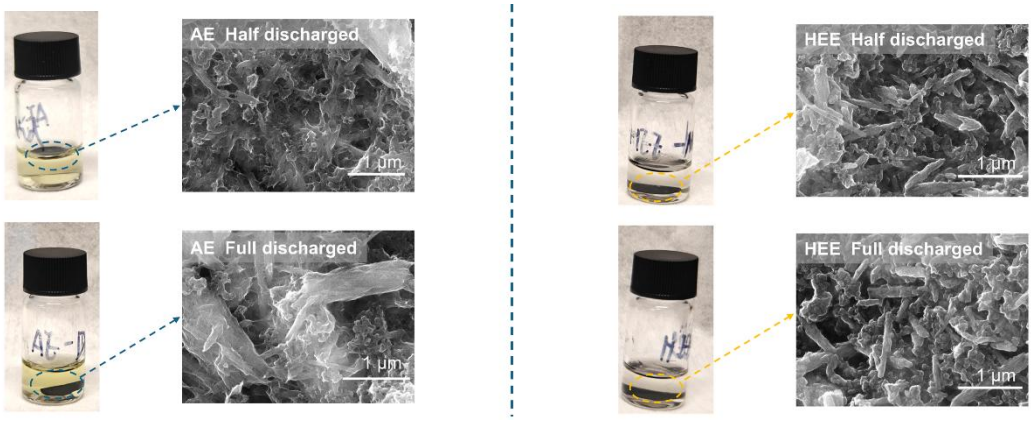

Figure 5.9 Optical photos and SEM images of V_2O_5 at various discharge stages.

Long-term cycling stability was also assessed at a high current density of 1000 mA g^{-1}. As shown in **Figure 5.8i**, the capacity in aqueous electrolyte rapidly declines due to irreversible vanadium dissolution, leaving only 24.1% capacity retention after around 600 cycles. In

contrast, with hydrated eutectic electrolyte, the initial specific capacity is 129.2 mAh g^{-1}, and after an activation process, the capacity can be well maintained, with an ultra-low capacity degradation rate of 0.0061% per cycle for 5000 cycles. Compared to recently reported vanadium-based electrodes in Mg ion batteries, V_2O_5 with this hydrated eutectic electrolyte demonstrates significantly enhanced electrochemical performance (**Table 5.1**), particularly in capacity and cycling stability.

Table 5.1. Comparison of the electrochemical performance for V_2O_5 in HEE with other vanadium-based electrodes for Mg ion batteries.

Working electrode	Counter electrode	Electrolyte	Specific capacity	Capacity /Cycle number/current	Ref.
V_2O_5	**AC**	**$Mg(ClO_4)_2·6H_2O$/ SL**	**322.7 mAh g^{-1}@50 mA g^{-1}**	**111.4 mA g^{-1} /5000/1 A g^{-1}**	**This work**
Mn-NVO	Pt	$MgCl_2·6H_2O$/ acetamide/urea	191.6 mAh g^{-1} @100 mA g^{-1}	105.3 mAh g^{-1}/60/500 mAg^{-1}	[60]
NVO	Pt	$Mg(ClO_4)_2$/TEGDME/H_2O	351 mAh g^{-1} @300 mA g^{-1}	81.7 mAh g^{-1}/1000/1.5 Ag^{-1}	[54]
CaVOnH	AC	$Mg(TFSI)_2$/PEG/DMSO/H_2O	264 mAh g^{-1} @50 mA g^{-1}	78 mAh g^{-1}/2000/1 Ag^{-1}	[162]
V_2O_5	AC	$Mg(TFSI)_2$/PEG/H_2O	326 mAh g^{-1} @50 mA g^{-1}	286 mAh g^{-1}/100/50 mAg^{-1}	[61]
V_2O_5	Pt	$Mg(TFSI)_2$/TMP/PEG/H_2O	300 $mAhg^{-1}$@0.1C	240 mAh g^{-1}/20/0.1 C	[164]
$Mg_{0.3}V_2O_5·1.1H_2O$	AC	$Mg(TFSI)_2$/AN	164 mAh g^{-1} @100 mA g^{-1}	108 mAh g^{-1}/10000/1 Ag^{-1}	[70]
V_2O_5-PAN	AC	$Mg(TFSI)_2$/AN	180 mAh g^{-1} @50 mA g^{-1}	56.6 mAh g^{-1}/18000/2 Ag^{-1}	[163]
NaV_3O_8	AC	$Mg(ClO_4)_2$/AN	204.2 mAh g^{-1} @100 mA g^{-1}	160 mAh g^{-1}/100/1A g^{-1}	[148]

5.2.3 Chemical structures of hydrated eutectic electrolytes

The distinct electrochemical performance for V_2O_5 cathode in these two electrolytes can be attributed to their distinct chemical structures and interfacial properties. In hydrated eutectic

electrolyte, a hydrogen bond forms between a donor with a hydrogen atom and an acceptor with lone electron pairs. Typically, the acceptor is a highly electronegative atom with a small radius, such as N or S, which helps anchor water molecules via forming stronger hydrogen networks to stabilize the electrolyte. Sulfolane serves as an effective regulator, capable of forming two hydrogen bonds with water molecules due to its two lone pairs of electrons (**Figure 5.10)**.

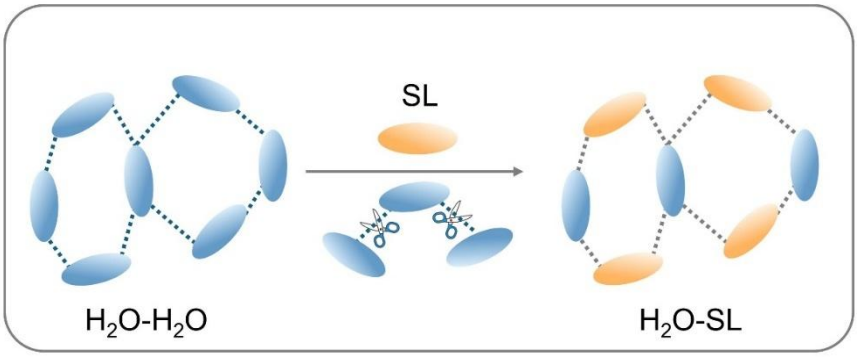

Figure 5.10 Schematic representation of hydrogen bonding between H_2O and SL.

As shown in **Figure 5.11a**, the oxygen atom in SL (S=O) has a more negative charge distribution (-40.94 kcal mol^{-1}) compared to the O-H in water (-37.3 kcal mol^{-1}), indicating a stronger attraction to hydrogen atoms. Density functional theory (DFT) calculations reveal that the hydrogen bond length of S=O…H-O (1.919 Å) is slightly shorter than H-O…H-O (1.933 Å) (**Figure 5.11b**). Furthermore, the binding energy for H_2O-SL (-0.34 eV) exceeds that of H_2O-H_2O (-0.25 eV) (**Figure 5.11c)**. These results suggest that SL can form stronger hydrogen bonds with water to suppress H_2O activity.

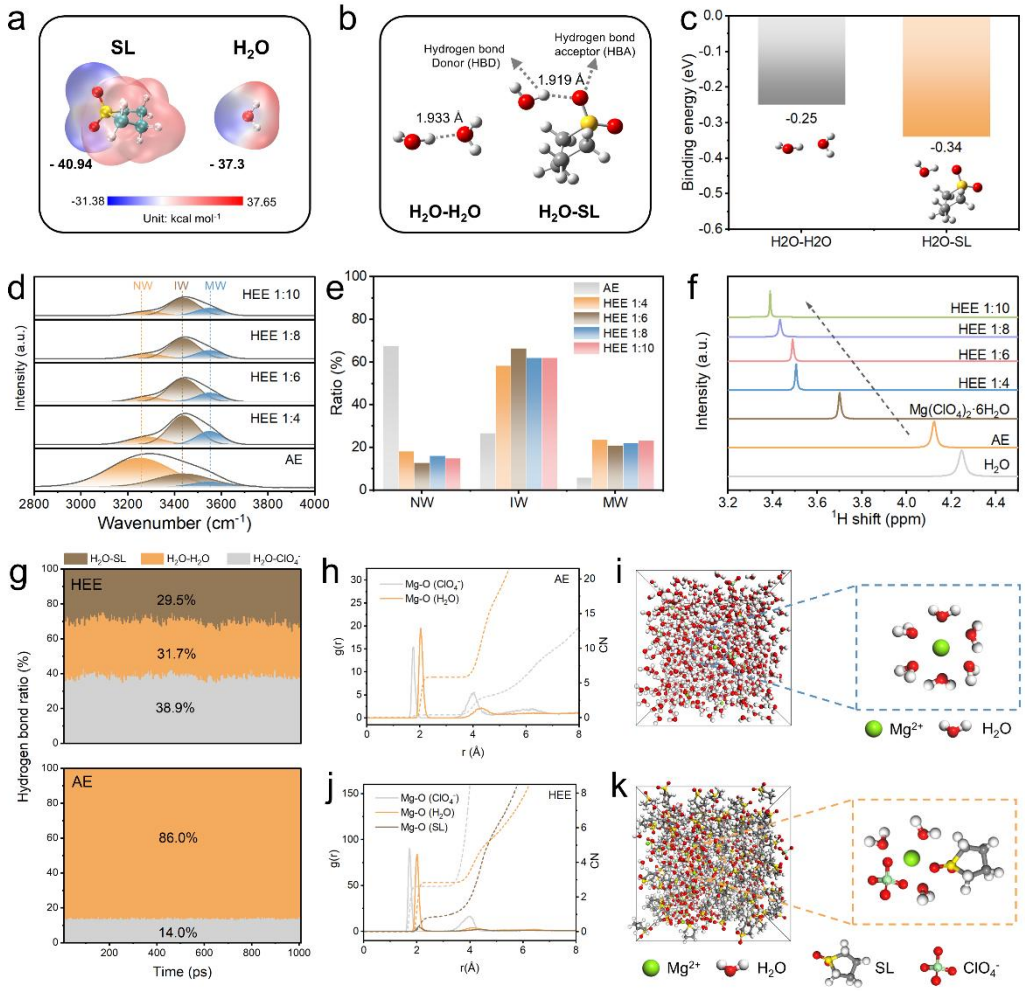

Figure 5.11 (a) Electrostatic potentials of SL and H_2O molecules. (b) Hydrogen bond lengths and (c) binding energies for H_2O-H_2O and H_2O-SL pairs. (d) FT-IR spectra of the O−H stretching region. (e) The ratios of different hydrogen bonds in AE and HEE. (f) The ^1H NMR spectra of H_2O, $Mg(ClO_4)_2·6H_2O$, AE, and HEEs. (g) Different types of hydrogen bonds ratio in AE and HEE from MD simulation. (h) Radial distribution functions and (i) 3D snapshot from MD simulation showing representative solvation structures in AE. (j) Radial distribution functions and (k) 3D snapshot from MD simulation showing representative solvation structures in HEE.

To illustrate the chemical interactions of SL and H_2O in hydrated eutectic electrolytes, we prepared a series of HEEs by mixing $Mg(ClO_4)_2·6H_2O$ and SL with different molar ratios ($n_{Mg(ClO4)2·6H2O}$: n_{SL}=1:4, 1:6, 1:8, and 1:10). All of them exhibit good solubility and characteristics of hydrated eutectic electrolytes (**Figure 5.12** and **Figure 5.13**). A 1 M

$Mg(ClO_4)_2$ aqueous electrolyte was used as the reference group.

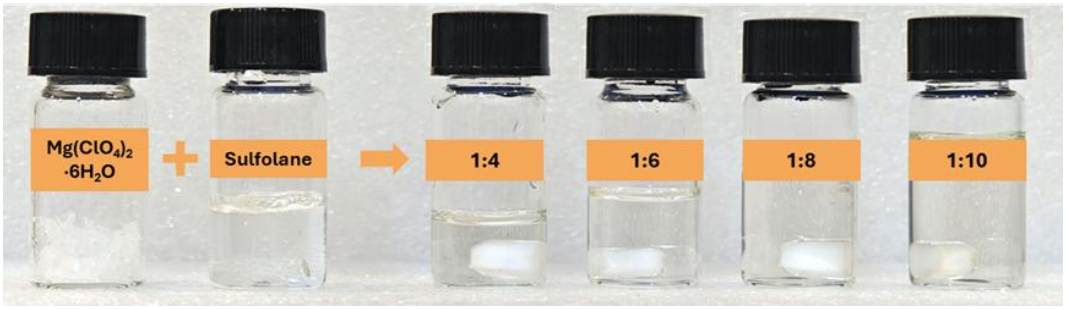

Figure 5.12 Optical photographs of the as-prepared HEEs with different molar ratios.

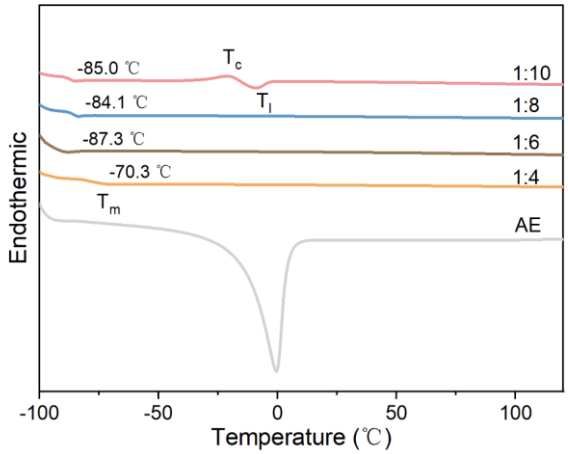

Figure 5.13 DSC curves of aqueous electrolyte and hydrated eutectic electrolytes with different molar ratios.

FT-IR spectra, known for its sensitivity to changes in molecular dipole moments, was adopted to investigate the hydrogen bond networks in these two electrolytes. As depicted in **Figure 5.11d**, in aqueous electrolyte, absorbance bands between 2800 and 4000 cm^{-1} correspond to the O-H stretching of H_2O, featuring three main peaks at 3270, 3440, 3550 cm^{-1}. These peaks represent network water (NW), intermediate water (IW), and multimeric water (MW), respectively [174, 175]. In hydrated eutectic electrolytes, these peaks exhibit a noticeable blueshift, indicating weakened H_2O-H_2O hydrogen bond networks and strengthened intermolecular hydrogen bonds [176, 177]. This shift is likely due to SL disrupting hydrogen bonds and altering Mg^{2+} coordination with H_2O. Additionally, the ratio of the three hydrogen bond peaks shows a decrease in intramolecular hydrogen bonding network (H_2O-H_2O) and a

significant increase in intermediate hydrogen bonds (H_2O-SL) **(Figure 5.11e)**. This result is consistent with DFT calculations results, as the higher binding energy of H_2O-SL (-0.34 eV) than that of H_2O-H_2O (-0.25 eV) in **Figure 5.11c**. This effect is further supported by ^1H liquid-state NMR spectra (**Figure 5.11f**), where the addition of $Mg(ClO_4)_2$ in aqueous electrolyte causes a slight chemical shift of hydrogen in water molecules (from 4.25 ppm to 4.13 ppm). In hydrated eutectic electrolytes, stronger SL-H_2O interactions increase the electron density around H_2O [177], shifting δ values to a higher field with a larger offset (from 3.7 ppm to 3.39 ppm).

To further understand the chemical structures of these two electrolytes, MD simulations were conducted to quantitatively analyze the hydrogen bonding species and solvation structures. The addition of SL destroys H_2O-H_2O hydrogen bonds, with reducing their average ratio from 86% in aqueous electrolyte to 31.5% in hydrated eutectic electrolyte (**Figure 5.11g**). Instead, new H_2O-SL hydrogen bonds are generated, reducing free water activity in bulk electrolyte. These descriptions are consistent with the results of FT-IR and NMR for the hydrated eutectic electrolyte. Solvation structures were examined using the RDFs and CNs. For aqueous electrolyte, the coordination primarily happens between Mg^{2+} and H_2O with six H_2O molecules surrounding one Mg^{2+} (designated as $[Mg(H_2O)_6]^{2+}$) at approximately 2 Å (**Figure 5.11h** and **5.11i**). These bounded H_2O molecules react with V_2O_5 cathode during Mg^{2+} insertion, aggravating vanadium dissolution and structural damage [178, 179]. As a comparison, in the hydrated eutectic electrolyte, Mg^{2+} is mainly coordinated by three H_2O molecules (designated as $[Mg(H_2O)_3]^{2+}$), with SL and ClO_4^- anions replacing some H_2O, leading to a decrease in the amount of bound water in the solvated structure (**Figure 5.11j** and **5.11k**). This aligns with the binding energy calculation results, which show that Mg^{2+}-SL (-6.71 eV) and Mg^{2+}-ClO_4^- (-13.78 eV) have higher binding energies than Mg^{2+}-H_2O (-3.59 eV), as presented **Figure 5.14**. In summary, these experimental and theoretical characterizations indicate that compared to traditional aqueous electrolytes, hydrated eutectic electrolytes could generate stronger

hydrogen bonding networks and simultaneously reduce coordinated H_2O with Mg^{2+} to suppress water activity.

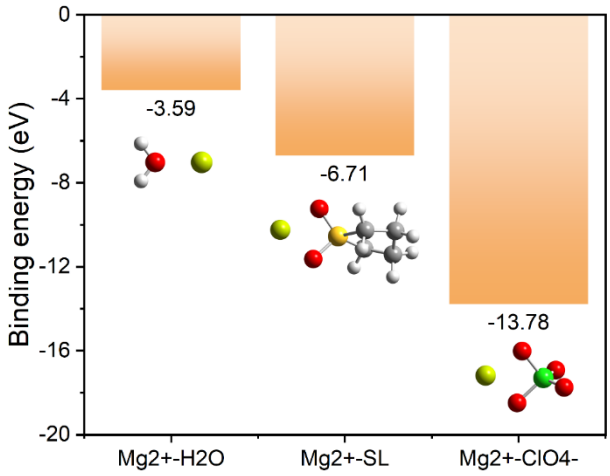

Figure 5.14 Binding energies of Mg^{2+}-H_2O, Mg^{2+}-SL, and Mg^{2+}-ClO_4^-.

5.2.4 CEI characteristics analysis

In addition to variations in bulk electrolyte structure, the Mg ion storage capacities for V_2O_5 cathode are also affected by the properties of the CEI. To explore this, we examined the desolvation energy of Mg^{2+} in the V_2O_5 cathode using symmetric cells with V_2O_5 cathodes at a half-charged state, employing varying-temperature EIS [168]. As depicted in **Figure 5.15**, the desolvation energy in the hydrated eutectic electrolyte is 18.2 kJ mol^{-1}, significantly lower than the 27.8 kJ mol^{-1} observed in aqueous electrolyte.

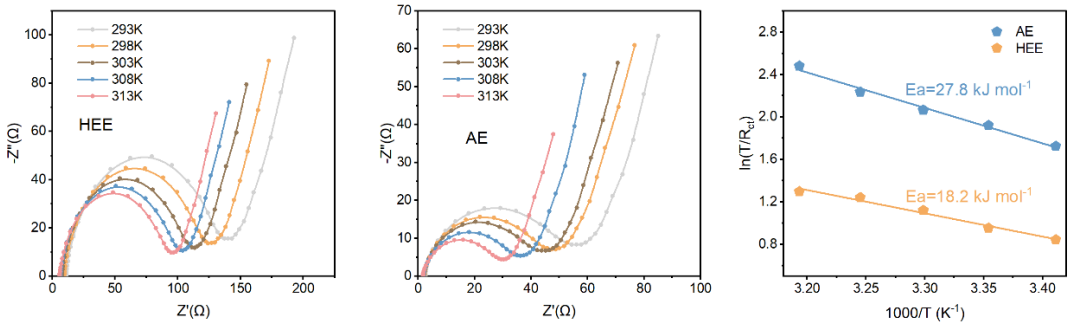

Figure 5.15 Temperature-dependent Nyquist plots of symmetric V_2O_5// V_2O_5 cells in hydrated eutectic electrolyte and aqueous electrolyte, and the corresponding desolvation energy of Mg^{2+} derived from Nyquist plots.

Additionally, **Figure 5.16** compares the wettability of two different electrolytes on V_2O_5 cathode. The result shows that the hydrated eutectic electrolyte significantly reduces the contact angle at the CEI, thereby facilitating the transport of Mg^{2+} flux across this interface.

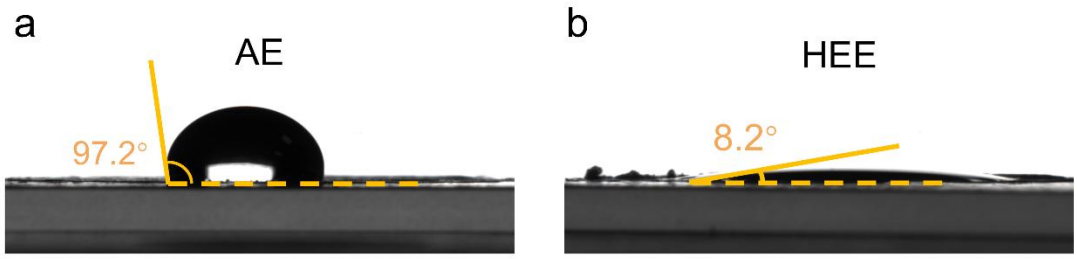

Figure 5.16 Contact angle measurement results of the V_2O_5 electrode with (a) aqueous electrolyte and (b) hydrated eutectic electrolyte.

DFT calculations offer an atomic-level perspective on these interactions. SL molecules exhibit lower adsorption energies than H_2O on the V_2O_5 cathode (**Figure 5.17a**), indicating a preference for SL adsorption at the interface. In more detail, differential charge density analysis reveals that vanadium atoms of V_2O_5 and hydrogen atoms of H_2O or sulfur atoms of SL primarily lose electrons, while the oxygen atoms from H_2O or SL gain electrons (**Figure 5.17b** and **5.17c**). In aqueous electrolyte, the interactions between H_2O and V_2O_5 involve a partial transfer of delocalized electrons from vanadium to oxygen (**Figure 5.17b**), potentially leading to V–O bonds disruption and V_2O_5 cathode dissolution [167, 173]. In contrast, in hydrated eutectic electrolyte, the interaction between SL and V_2O_5 results in less electrons loss from vanadium atoms due to a more uniform charge distribution of SL, improving the stability of V-O bonds. Moreover, the sulfur atoms of SL also participate in electron transfer, strengthening the chemical affinity between SL and the V_2O_5 cathode.

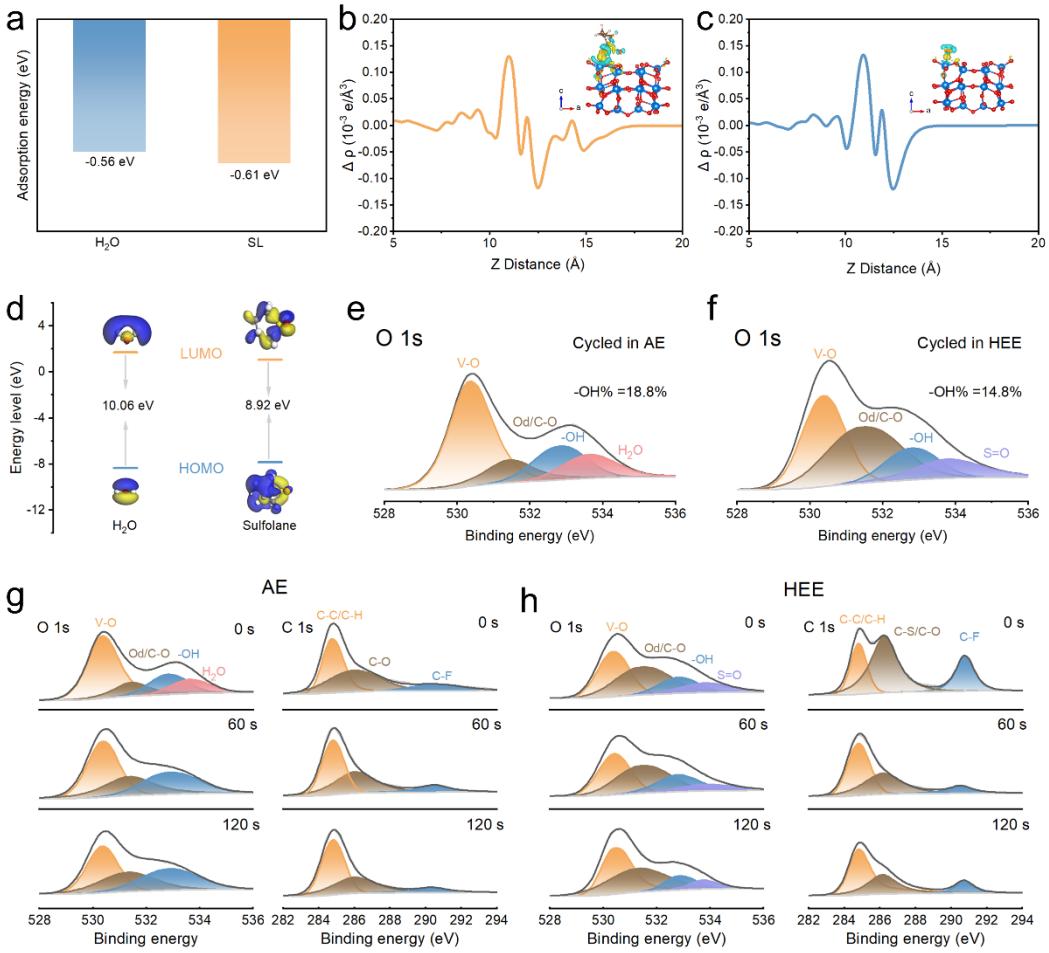

Figure 5.17 (a)Adsorption energy of H_2O and SL on V_2O_5 cathode. Planar average differential charge density of (b)SL and (c) H_2O on V_2O_5 cathode. Regions of charge accumulation are shown in yellow, and regions of charge depletion are shown in blue. (d) LUMO-HOMO energy level of H_2O and SL. XPS spectra of O 1s for V_2O_5cycled in (e) AE and (f) HEE. (g) In-depth XPS spectra of O 1s and C 1s for the cycled V_2O_5 in AE. (h) In-depth XPS spectra of O 1s and C 1s for the cycled V_2O_5 in HEE.

To evaluate the potential chemical structure of the CEI, the energy levels of the lowest unoccupied molecular orbital (LUMO) and the highest occupied molecular orbital (HOMO) were calculated. As illustrated in **Figure 5.17d**, SL molecules exhibit a lower LUMO energy level (1.06 eV) than water molecules (1.70 eV). This indicates that SL molecules are more prone to get electrons attached to the cathode, accelerating delocalized electron transfer from SL to V_2O_5 cathode [180]. This description aligns with previous DFT calculations on the cathode-

electrolyte interactions. Therefore, SL molecules could not only restructure hydrogen bonds but also preferentially adsorb at the cathode interface, thereby mitigating water-induced deterioration.

Ex-situ XRD and XPS were employed to analyze the impact of the two electrolytes on the V_2O_5 cathode. Ex-situ XRD patterns of the V_2O_5 cathode reveal similar transition processes in both aqueous and hydrated eutectic electrolytes (**Figure 5.18**). During full discharge, most V_2O_5 reflections shifted to lower angles, and upon full charge, they return to initial position, indicating a reversible solid solution transition. However, in aqueous electrolyte, V_2O_5 peak intensity gradually becomes weak, particularly after 20 and 50 cycles, there is nearly no peak observed, corresponding to the severe active material dissolution. Conversely, when cycled in hydrated eutectic electrolyte, almost all characteristic peaks of V_2O_5 are well maintained, demonstrating better compatibility with the cathode.

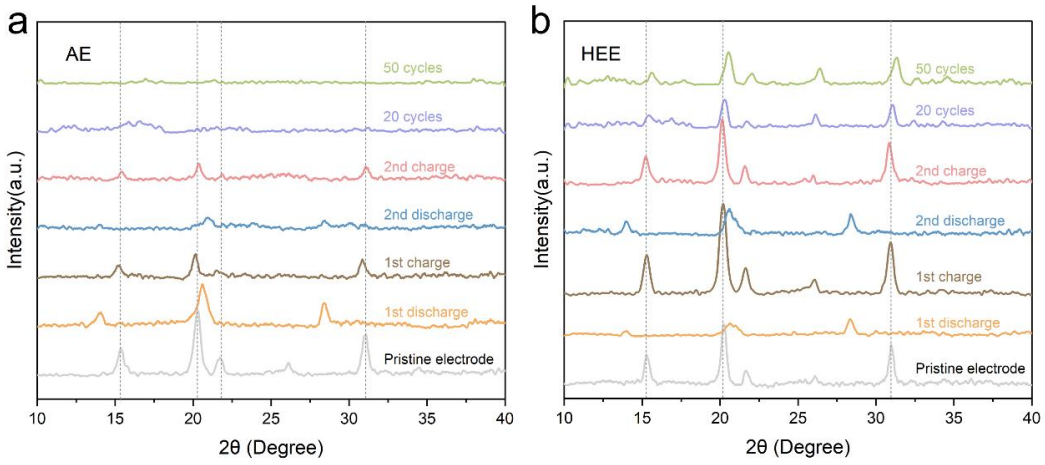

Figure 5.18 Ex-situ XRD spectra of V_2O_5 cathode in (a) AE and (b) HEE.

For pristine V_2O_5, the O 1s spectra shows peaks at 530.3, 531.3, and 532.8 eV, corresponding to V-O, O_d/C-O, and -OH, respectively (**Figure 5.19**) [181]. Cycling in aqueous electrolyte introduces a new peak at 533.6 eV (H_2O), increasing the -OH proportion to 18.8% (**Figure 5.17e**). Differently, cycling in hydrated eutectic electrolyte results in a new peak at 533.8 eV (S=O) and increased C-O bonds (**Figure 5.17f**), which can be attributed to SL's

preferential adsorption.

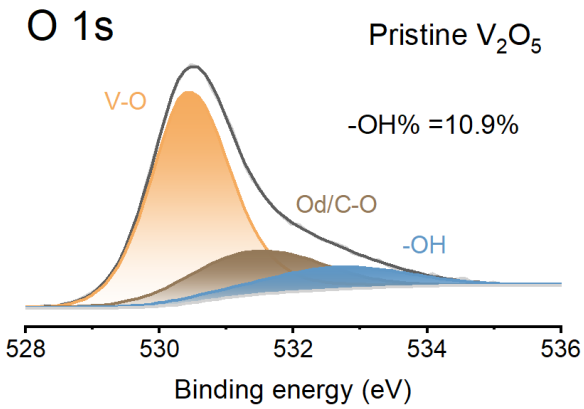

Figure 5.19 XPS spectra of O 1s for the pristine V_2O_5.

To thoroughly investigate the potential formation of the CEI layer, we conducted in-depth XPS characterizations with varying Ar^+ etching time (0, 60, and 120 s). As shown in **Figure 5.17g**, a continuous -OH distribution was observed in the aqueous electrolyte, attributing to strong interactions between water molecules and the cathode. In contrast, the hydrated eutectic electrolyte exhibits a gradient distribution of C-O and S=O peaks in the C 1s and O 1s spectra (**Figure 5.17f**). This finding further confirms the protective capability of SL, which effectively shields V_2O_5 from water, thereby maintaining cathode stability.

5.2.5 PTCDA//V_2O_5 full cells application in hydrated eutectic electrolytes

Finally, to explore the practical application of the hydrated eutectic electrolyte, we assembled a full cell using V_2O_5 as the cathode and an open-framework Perylene-3,4,9,10-tetracarboxylic dianhydride (PTCDA) as the anode (**Figure 5.22a**). PTCDA was chosen for its stable monoclinic structure and rapid Mg^{2+} diffusion capability [59, 164], which aligns well with the hydrated eutectic electrolyte (**Figure 5.20** and **5.21**).

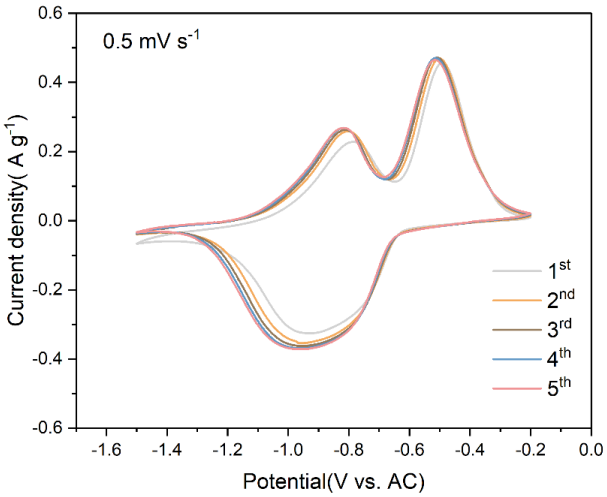

Figure 5.20 CV curves of PTCDA in HEE.

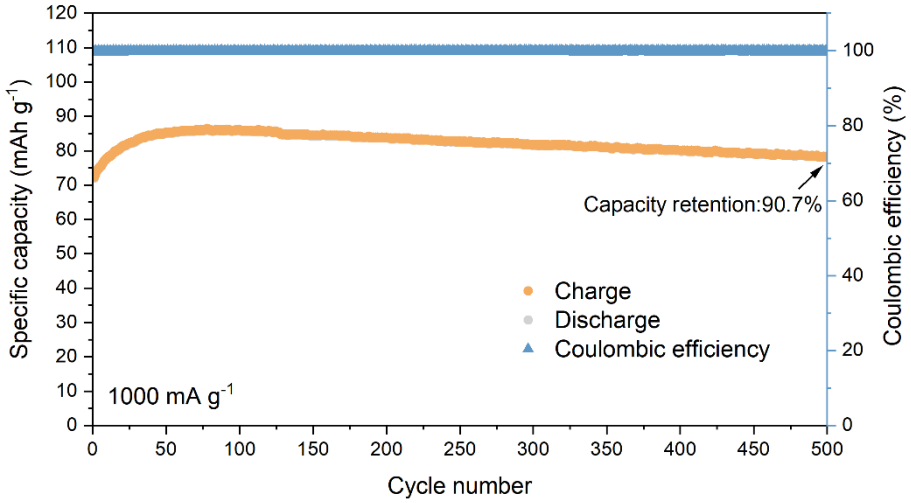

Figure 5.21 Cycling performance of PTCDA in hydrated eutectic electrolyte at the current density of 1000 mA g^{-1}.

The electrochemical performance of the PTCDA//V_2O_5 full cells with the hydrated eutectic electrolyte was evaluated within a voltage range of 0.01-2.2 V. During the experiments, the N/P (negative-to-positive electrode) ratio was kept at approximately 1.2. CV measurements were performed at a scan rate of 0.5 mV s^{-1}. As illustrated in **Figure 5.22b**, in the charging process, a distinct oxidation peak appears around 0.7 V, indicating Mg^{2+} extraction from the pre-magnesiumized V_2O_5 cathode and its intercalation into PTCDA anode. In the discharging process, a reduction peak appears at approximately 0.17 V, corresponding to Mg^{2+} de-intercalation from PTCDA anode and its insertion into V_2O_5 cathode. All CV curves remain

almost intact even after 20 cycles, demonstrating outstanding electrochemical stability and reversibility.

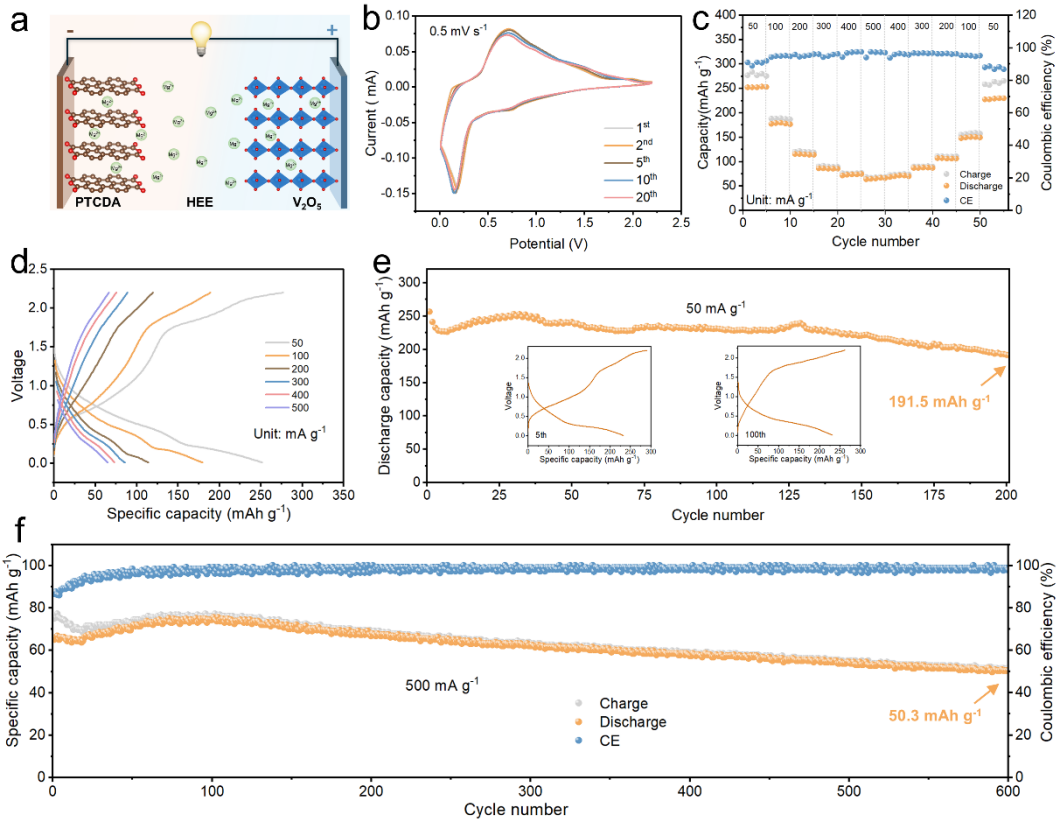

Figure 5.22 (a) Schematic representation of a PTCDA//V_2O_5 full cell. (b) CV curves of PTCDA//V_2O_5 full cells in HEE at 0.5 mV s^{-1}. (c) rate capability of PTCDA//V_2O_5 full cells in HEE from the current rate of 50 mA g^{-1} to 500 mA g^{-1} and (d) Voltage-capacity curves of PTCDA//V_2O_5 full cells in HEE at different current densities. Cycling performance of PTCDA//V_2O_5 full cells in HEE at (e) 50 mA g^{-1} and (f) 500 mA g^{-1}.

As illustrated in **Figure 5.22c** and **5.22d**, the rate performance reveals high discharge capacities of 252.3, 178.0, 114.7, 86.0, 73.4 and 65.6 mAh g^{-1} at current densities of 50, 100, 200, 300, 400, 500 mA g^{-1}, respectively. When current densities gradually return to the initial values, the capacity remains very high, indicating superior electrochemical stability. Finally, the long cycling performance of the full cells was evaluated at a rate of 50 mA g^{-1} and 500 mA g^{-1}, respectively. The specific capacity remains above 190 mAh g^{-1}@ 50 mA g^{-1} after 200 cycles (**Figure 5.22e**) and 50 mA g^{-1} @ 500 mA g^{-1} after 600 cycles (**Figure 5.22f**), outperforming

most of the reported magnesium ion full batteries (**Table 5.2**). These findings highlight the practical feasibility of hydrated eutectic systems, paving the way for further advancement in AMIBs.

Table 5.2 Comparison of the electrochemical performance of full MIBs.

Electrolyte formula	Cell type	Cell performance	Capacity /Cycle number/current	Ref
$Mg(ClO_4)_2·6H_2O$/ SL	**PTCDA//V_2O_5**	**252.3 mAh g^{-1}@50 mA g^{-1}**	**191.5 mAh g^{-1}/200/50 mA g^{-1} 50.3 mAh g^{-1}/600/500 mA g^{-1}**	**This work**
$MgCl_2·6H_2O$/ acetamide/urea	Mn-NVO//CuHCF	59.1 mAh g^{-1} @100 mA g^{-1}	38.7 mAh g^{-1}/800/1 A g^{-1}	[60]
$Mg(TFSI)_2$/TMP/PEG/H_2O	PTCDI//V_2O_5	227.6 mAh g^{-1} @0.1C	50 mAh g^{-1}/850/0.5 C	[164]
$Mg(NO_3)_2·6H_2O$/ acetamide	PTCDA//CuHCF	38.1 mAh g^{-1} @5C	24 mAh g^{-1}/1000/8 C	[59]
$MgCl_2·6H_2O/H_2O$	Mg//CuHCF	47 mAh g^{-1}@250 mA g^{-1}	20 mAh g^{-1}/700/0.5 A g^{-1}	[58]
$Mg(TFSI)_2$/AN	$MgNaTi_3O_7$//$Mg_{0.3}V_2O_5·1.1H_2O$	57 mAh g^{-1} @100 mA g^{-1}	42 mAh g^{-1}/100/100 mA g^{-1}	[70]
$Mg(TFSI)_2$/AN	$MgNaTi_3O_7$//V_2O_5-PAN	120.6 mAh g^{-1} @100 mA g^{-1}	50 mAh g^{-1}/80/100 mA g^{-1}	[163]
$Mg(TFSI)_2/H_2O$	PPMDA//$Mg_xLiV_2(PO_4)_3$	52 mAh g^{-1} @100 mA g^{-1}	43 mAh g^{-1}/1000/200 mA g^{-1}	[150]

5.3 Summary

In summary, we have developed a novel sulfolane-based hydrated eutectic electrolyte to comprehensively prevent cathode dissolution in AMIBs. In bulk electrolyte, the incorporation of SL forms stronger hydrogen bonds with water and simultaneously displaces some bound water in the Mg^{2+} solvation structure. This significantly reduces water activity, thereby minimizing its chemical attack to V_2O_5 cathode. Additionally, SL preferentially adsorbs onto the cathode surface, providing further protection against water-induced dissolution. Consequently, V_2O_5 cathode paired with the hydrated eutectic electrolyte demonstrates a high

capacity of 322.7 mAh g^{-1} at 50 mA g^{-1} and exceptional cycling stability over 5000 cycles, with a minimal capacity degradation rate of 0.0061% per cycle at 1000 mA g^{-1}. As a proof of concept, a full PTCDA//V_2O_5 battery using HEE was successfully assembled, achieving a remarkable discharge capacity of 252.3 mAh g^{-1} at 50 mA g^{-1} and maintaining a capacity exceeding 190 mAh g^{-1} for over 200 cycles. This electrolyte strategy offers a promising approach for designing cost-effective aqueous multivalent batteries in the future.

Chapter 6 Conclusion and future work

6.1 Conclusion

This thesis explores a series of electrolyte engineering strategies to address the challenges of sluggish Mg^{2+} kinetics and electrode/electrolyte interface incompatibility in MRBs. The primary goal is to achieve fast Mg^{2+} kinetics and long-life MRBs that are essential for real-world, high-energy implementations. In addition, this work includes a fundamental investigation of electrolyte structures and their impact on the electrode/electrolyte interface, providing crucial insights for stabilizing both cathode and anode during extended cycling. A systematic comparison of the proposed electrolytes is conducted from several key perspectives, including cost-effectiveness, ionic conductivity, cycling stability, energy density, and safety, highlighting their respective advantages and disadvantages and their potential suitability for various applications.

MCE demonstrates notable benefits in terms of safety and energy density. Experimental and simulation results reveal that urea-Mg^{2+} solvation structures form anion-rich groups, promoting rapid Mg^{2+} migration in the MCE. In Mg//Mg symmetric cells, the electrolyte produces a microporous, fluoride-rich organic/inorganic hybrid layer on the Mg metal surface. This distinctive interface enables efficient Mg^{2+} diffusion, supporting reversible Mg metal stripping and plating. The practical viability of MCE is further validated in Mg//V_2O_5 full cells. However, the cycling stability remains inferior compared to current liquid-state electrolytes. Overall, this work pioneers the crystallization of deep eutectic solvents into room-temperature solid-state electrolytes, offering new strategy for multivalent metal batteries.

The advancement of RMBs is limited by the absence of high-capacity cathodes, primarily due to sluggish Mg^{2+} desolvation at the cathode-electrolyte interface and $TFSI^-$-induced surface passivation in conventional $Mg(TFSI)_2$/DME electrolyte. To overcome these challenges, we incorporated a hydroxyl-rich EG solvent into the ether-based electrolyte, which disrupts unfavorable $[Mg(DME)_3]^{2+}$ complexes and establishes hydrogen bond networks. This

modification enhances Mg^{2+} ion migration while simultaneously suppressing $TFSI^-$ decomposition. While further improvements in cycling stability and safety are necessary, the EG/DME co-solvent electrolyte exhibits superior ionic conductivity and energy density, enabling high-capacity VO_2 cathodes to achieve ultra-long cycling stability. Notably, Mg//VO_2 full cells utilizing this electrolyte deliver capacities exceeding 160 mAh g^{-1} over 50 cycles, advancing the practical application of RMBs.

Aqueous RMBs are increasingly recognized as promising options for large-scale energy storage, owing to their low cost and inherent safety. V_2O_5 cathode, despite its high specific capacity, suffers from severe dissolution issues caused by strong interactions with water molecules in conventional aqueous electrolytes. This HEE greatly reduced the cathode dissolution issues caused by high water activity in conventional aqueous electrolytes, achieving ultra-stable electrochemical performance. Specifically, the S=O group in sulfolane disrupts H_2O-H_2O hydrogen bonding, lowering water activity in the bulk electrolyte. Its involvement in Mg^{2+} solvation further decreases water content at the cathode-electrolyte interface and facilitates Mg^{2+} desolvation. Additionally, the preferential adsorption of sulfolane at the interface protects V_2O_5 from water-induced vanadium dissolution. Although the ionic conductivity and energy density of HEE require further enhancement compared to current organic electrolytes, it offers significant advantages in cost-effectiveness, cycling stability, and energy density, enabling V_2O_5 cathodes to achieve high capacity with exceptional cycling stability over 5000 cycles. As a proof of concept, a full PTCDA//V_2O_5 battery with HEE demonstrates high capacity and high voltage output, which provides new ideas for durable multivalent batteries.

6.2 Future work

To commercialize MRBs as a cost-effective alternative to current LIBs, the development of suitable electrolytes remains a critical challenge. In this thesis, we have designed a series of

electrolytes compatible with both cathodes and anodes, and systematically investigated their structures as well as the corresponding electrode-electrolyte interfacial chemistry. These findings lay a solid foundation for the future commercialization of MRBs. However, as research on MRBs is still in its early stages, the availability of high-capacity cathodes and compatible anodes remains limited, hindering their competitiveness with LIBs. Therefore, future efforts should prioritize not only optimizing electrolyte design strategies but also advancing the development of high-performance cathodes and stable anodes.

(1) *Efficient electrolytes screening strategi*es: Traditionally, electrolyte engineering relied on trial-and-error approaches, which are both time-consuming and resource-intensive. The advent of artificial intelligence now enables the rapid screening of suitable salts, solvents, and additives through advanced computational algorithms. This data-driven methodology significantly enhances research efficiency compared to conventional techniques, thereby accelerating the practical implementation of MRBs.

(2) *High-performance cathodes*: The current mainstream cathode, Chevrel phase Mo_6S_8, has low voltage and theoretical capacity, insufficient for high-capacity needs. Although some high-capacity cathodes, such as layered transition metal oxides/sulfur, show relatively high energy density, they are limited in availability, and the mechanisms are not fully understood. Future research should focus on developing new high-performance cathodes to meet practical development needs.

(3) *Stable anodes*: While the Mg metal anode is the most ideal choice due to its stability, safety, and low reduction potential, most commercial electrolytes are incompatible with Mg metal, leading to severe passivation and poor cycling life. To achieve MRB's stable operation, it is essential to modify and protect the Mg metal anode or develop suitable anode alternatives to pair with other battery components.

References

(1) Zhang, P.; Zhu, F.; Wang, F.; Wang, J.; Dong, R.; Zhuang, X.; Schmidt, O. G.; Feng, X. Stimulus-responsive micro-supercapacitors with ultrahigh energy density and reversible electrochromic window. *Adv. Mater.* 2017, 29 (7), 1604491.

(2) Chang, P.; Mei, H.; Zhang, M.; Zhao, Y.; Wang, X.; Cheng, L.; Zhang, L. 3D printed electrochromic supercapacitors with ultrahigh mechanical strength and energy density. *Small* 2021, 17 (41), e2102639.

(3) Yang, Z.; Zhang, J.; Kintner-Meyer, M. C.; Lu, X.; Choi, D.; Lemmon, J. P.; Liu, J. Electrochemical energy storage for green grid. *Chem. Rev.* 2011, 111 (5), 3577-3613.

(4) Yoshino, A. The birth of the lithium-ion battery. *Angew. Chem. Int. Ed.* 2012, 51 (24), 5798-5800.

(5) Zheng, S.; Shi, X.; Das, P.; Wu, Z. S.; Bao, X. The road towards planar microbatteries and micro-supercapacitors: from 2D to 3D device geometries. *Adv. Mater.* 2019, 31 (50), e1900583.

(6) Niu, H.; Zhang, N.; Lu, Y.; Zhang, Z.; Li, M.; Liu, J.; Zhang, N.; Song, W.; Zhao, Y.; Miao, Z. Strategies toward the development of high-energy-density lithium batteries. *J. Energy Storage* 2024, 88, 111666.

(7) Koyamparambath, A.; Santillán-Saldivar, J.; McLellan, B.; Sonnemann, G. Supply risk evolution of raw materials for batteries and fossil fuels for selected OECD countries (2000–2018). *Resour. Policy* 2022, 75, 102465.

(8) Li, H.; Zhu, T.; Chen, X.; Liu, H.; He, G. Improving China's global lithium resource development capacity. *Front. Environ. Sci.* 2022, 10, 938534.

(9) Shi, F.; Chen, C.; Xu, Z.-L. Recent advances on electrospun nanofiber materials for post-lithium ion batteries. *Adv. Fiber Mater.* 2021, 3 (5), 275-301.

(10) Liang, Y.; Dong, H.; Aurbach, D.; Yao, Y. Current status and future directions of multivalent metal-ion batteries. *Nat. Energy* 2020, 5 (9), 646-656.

(11) Attias, R.; Salama, M.; Hirsch, B.; Goffer, Y.; Aurbach, D. Anode-electrolyte interfaces in

secondary magnesium batteries. *Joule* 2019, 3 (1), 27-52.

(12) Mohtadi, R.; Tutusaus, O.; Arthur, T. S.; Zhao-Karger, Z.; Fichtner, M. The metamorphosis of rechargeable magnesium batteries. *Joule* 2021, 5 (3), 581-617.

(13) Muldoon, J.; Bucur, C. B.; Gregory, T. Quest for nonaqueous multivalent secondary batteries: magnesium and beyond. *Chem. Rev.* 2014, 114 (23), 11683-720.

(14) Deivanayagam, R.; Ingram, B. J.; Shahbazian-Yassar, R. Progress in development of electrolytes for magnesium batteries. *Energy Storage Mater.* 2019, 21, 136-153.

(15) Zhang, J.; Chang, Z.; Zhang, Z.; Du, A.; Dong, S.; Li, Z.; Li, G.; Cui, G. Current design strategies for rechargeable magnesium-based batteries. *ACS Nano* 2021, 15 (10), 15594-15624.

(16) Sun, Q.; Luo, S.; Huang, R.; Yan, S.; Lin, X. Recent progress of magnesium electrolytes for rechargeable magnesium batteries. *Coord. Chem. Rev.* 2024, 515, 215956.

(17) Gregory, T. D.; Hoffman, R. J.; Winterton, R. C. Nonaqueous electrochemistry of magnesium: applications to energy storage. *J. Electrochem. Soc.* 1990, 137 (3), 775.

(18) Kim, J.; Kim, M.; Lee, J.; An, J.; Yang, S.; Ahn, H. C.; Yoo, D.-J.; Choi, J. W. Insights from Li and Zn systems for advancing Mg and Ca metal batteries. *Chem. Soc. Rev.* 2024, 53 (17), 8878-8902.

(19) Shi, H.; Wang, G.; Wang, Z.; Yang, L.; Zhang, S.; Dong, S.; Qu, B.; Du, A.; Li, Z.; Zhou, X.; Cui, G. Understanding the cathode-electrolyte interfacial chemistry in rechargeable magnesium batteries. *Adv. Sci.* 2024, 11 (25), e2401536.

(20) Son, S.-B.; Gao, T.; Harvey, S. P.; Steirer, K. X.; Stokes, A.; Norman, A.; Wang, C.; Cresce, A.; Xu, K.; Ban, C. An artificial interphase enables reversible magnesium chemistry in carbonate electrolytes. *Nat. Chem.* 2018, 10 (5), 532-539.

(21) Liu, F.; Cao, G.; Ban, J.; Lei, H.; Zhang, Y.; Shao, G.; Zhou, A.; Fan, L. z.; Hu, J. Recent advances based on Mg anodes and their interfacial modulation in Mg batteries. *J. Magnes. Alloys.* 2022, 10 (10), 2699-2716.

(22) Mohtadi, R.; Mizuno, F. Magnesium batteries: current state of the art, issues and future

perspectives. *Beilstein J. Nanotechnol.* 2014, 5 (1), 1291-1311.

(23) Zhang, H.; Qiao, L.; Kühnle, H.; Figgemeier, E.; Armand, M.; Eshetu, G. G. From lithium to emerging mono-and multivalent-cation-based rechargeable batteries: non-aqueous organic electrolyte and interphase perspectives. *Energy Environ. Sci.* 2023, 16 (1), 11-52.

(24) Zhao, W.; Liu, Y.; Zhao, X.; Pan, Z.; Chen, J.; Zheng, S.; Qu, L.; Yang, X. Chloride-free electrolytes for high-voltage magnesium metal batteries: challenges, strategies, and perspectives. *Chem. Eur. J.* 2023, 29 (10), e202203334.

(25) Zhang, Z.; Cui, Z.; Qiao, L.; Guan, J.; Xu, H.; Wang, X.; Hu, P.; Du, H.; Li, S.; Zhou, X.; Dong, S.; Liu, Z.; Cui, G.; Chen, L. Novel design concepts of efficient Mg-ion electrolytes toward high-performance magnesium-selenium and magnesium-sulfur batteries. *Adv. Energy Mater.* 2017, 7 (11), 1602055.

(26) Aurbach, D.; Lu, Z.; Schechter, A.; Gofer, Y.; Gizbar, H.; Turgeman, R.; Cohen, Y.; Moshkovich, M.; Levi, E. Prototype systems for rechargeable magnesium batteries. *Nature* 2000, 407 (6805), 724-727.

(27) Aurbach, D.; Gofer, Y.; Lu, Z.; Schechter, A.; Chusid, O.; Gizbar, H.; Cohen, Y.; Ashkenazi, V.; Moshkovich, M.; Turgeman, R.; Levi, E. A short review on the comparison between Li battery systems and rechargeable magnesium battery technology. *J. Power Sources* 2001, 97, 28-32.

(28) Aurbach, D.; Weissman, I.; Gofer, Y.; Levi, E. Nonaqueous magnesium electrochemistry and its application in secondary batteries. *Chem. Rec.* 2003, 3 (1), 61-73.

(29) Mizrahi, O.; Amir, N.; Pollak, E.; Chusid, O.; Marks, V.; Gottlieb, H.; Larush, L.; Zinigrad, E.; Aurbach, D. Electrolyte solutions with a wide electrochemical window for rechargeable magnesium batteries. *J. ElectroChem. Soc.* 2007, 155 (2), A103.

(30) Kim, H. S.; Arthur, T. S.; Allred, G. D.; Zajicek, J.; Newman, J. G.; Rodnyansky, A. E.; Oliver, A. G.; Boggess, W. C.; Muldoon, J. Structure and compatibility of a magnesium electrolyte with a sulphur cathode. *Nat. Commun.* 2011, 2 (1), 427.

(31) Doe, R. E.; Han, R.; Hwang, J.; Gmitter, A. J.; Shterenberg, I.; Yoo, H. D.; Pour, N.; Aurbach, D. Novel, electrolyte solutions comprising fully inorganic salts with high anodic stability for rechargeable magnesium batteries. *Chem. Commun.* 2014, 50 (2), 243-245.

(32) Canepa, P.; Jayaraman, S.; Cheng, L.; Rajput, N. N.; Richards, W. D.; Gautam, G. S.; Curtiss, L. A.; Persson, K. A.; Ceder, G. Elucidating the structure of the magnesium aluminum chloride complex electrolyte for magnesium-ion batteries. *Energy Environ. Sci.* 2015, 8 (12), 3718-3730.

(33) Mohtadi, R.; Matsui, M.; Arthur, T. S.; Hwang, S.-J. Magnesium borohydride: from hydrogen storage to magnesium battery. *Angew. Chem. Int. Ed.* 2012, 51 (39), 9780.

(34) Tutusaus, O.; Mohtadi, R.; Arthur, T. S.; Mizuno, F.; Nelson, E. G.; Sevryugina, Y. V. An efficient halogen-free electrolyte for use in rechargeable magnesium batteries. *Angew. Chem. Int. Ed.* 2015, 127 (27), 8011-8015.

(35) Dong, H.; Tutusaus, O.; Liang, Y.; Zhang, Y.; Lebens-Higgins, Z.; Yang, W.; Mohtadi, R.; Yao, Y. High-power Mg batteries enabled by heterogeneous enolization redox chemistry and weakly coordinating electrolytes. *Nat. Energy* 2020, 5 (12), 1043-1050.

(36) Zhao-Karger, Z.; Bardaji, M. E. G.; Fuhr, O.; Fichtner, M. A new class of non-corrosive, highly efficient electrolytes for rechargeable magnesium batteries. *J. Mater. Chem. A* 2017, 5 (22), 10815-10820.

(37) Li, S.; Zhang, J.; Zhang, S.; Liu, Q.; Cheng, H.; Fan, L.; Zhang, W.; Wang, X.; Wu, Q.; Lu, Y. Cation replacement method enables high-performance electrolytes for multivalent metal batteries. *Nat. Energy* 2024, 9 (3), 285-297.

(38) Attias, R.; Salama, M.; Hirsch, B.; Pant, R.; Gofer, Y.; Aurbach, D. Anion effects on cathode electrochemical activity in rechargeable magnesium batteries: a case study of V_2O_5. *ACS Energy Lett.* 2018, 4 (1), 209-214.

(39) Liu, Y.; Zhao, W.; Pan, Z.; Fan, Z.; Zhang, M.; Zhao, X.; Chen, J.; Yang, X. Interfacial engineering of magnesiophilic coordination layer stabilizes Mg metal anode. *Angew. Chem. Int.*

Ed. 2023, 62 (25), e202302617.

(40) Wang, M.; Sun, W.; Zhang, K.; Zhang, Z.; Du, A.; Dong, S.; Zhang, J.; Liu, J.; Chen, X.; Zhou, Z.; Li, F.; Li, Z.; Li, G.; Cui, G. Synergy of coordination and trace ionization from co-solvents enables reversible magnesium electroplating/stripping behavior. *Energy Environ. Sci.* 2024, 17(2), 630-641.

(41) Hou, S.; Ji, X.; Gaskell, K.; Wang, P.-f.; Wang, L.; Xu, J.; Sun, R.; Borodin, O.; Wang, C. Solvation sheath reorganization enables divalent metal batteries with fast interfacial charge transfer kinetics. *Science* 2021, 374 (6564), 172-178.

(42) Zhao, W.; Pan, Z.; Zhang, Y.; Liu, Y.; Dou, H.; Shi, Y.; Zuo, Z.; Zhang, B.; Chen, J.; Zhao, X.; Yang, X. Tailoring coordination in conventional ether-based electrolytes for reversible magnesium-metal anodes. *Angew. Chem. Int. Ed.* 2022, 61 (30), e202205187.

(43) Li, C.; Guha, R. D.; Shyamsunder, A.; Persson, K. A.; Nazar, L. F. A weakly ion pairing electrolyte designed for high voltage magnesium batteries. *Energy Environ. Sci.* 2024, 17(1), 190-201.

(44) Zhang, D.; Wang, Y.; Yang, Y.; Zhang, Y.; Zhao, Y.; Pan, M.; Sun, Y.; Chen, S.; Liu, X.; Wang, J.; NuLi, Y. Constructing efficient $Mg(CF_3SO_3)_2$ electrolyte via tailoring solvation and interface chemistry for high-performance rechargeable magnesium batteries. *Adv. Energy Mater.* 2023, 13 (39), 2301795.

(45) Li, C.; Guha, R. D.; House, S. D.; Bazak, J. D.; Yu, Y.; Zhou, L.; Zavadil, K.; Persson, K. A.; Nazar, L. F. A dynamically bare metal interface enables reversible magnesium electrodeposition at 50 mAh cm^{-2}. *Joule* 2024, 9 (2), 101790.

(46) Roy, A.; Sotoudeh, M.; Dinda, S.; Tang, Y.; Kübel, C.; Groß, A.; Zhao-Karger, Z.; Fichtner, M.; Li, Z. Improving rechargeable magnesium batteries through dual cation co-intercalation strategy. *Nat. Commun.* 2024, 15 (1), 492.

(47) Wan, L. F.; Perdue, B. R.; Apblett, C. A.; Prendergast, D. Mg desolvation and intercalation mechanism at the Mo_6S_8 chevrel phase surface. *Chem. Mater.* 2015, 27 (17), 5932-5940.

(48) Attias, R.; Chae, M. S.; Dlugatch, B.; Oliel, M.; Goffer, Y.; Aurbach, D. The role of surface adsorbed Cl^- complexes in rechargeable magnesium batteries. *ACS Catal.* 2020, 10 (14), 7773-7784.

(49) Wang, D.; Du, X.; Chen, G.; Song, F.; Du, J.; Zhao, J.; Ma, Y.; Wang, J.; Du, A.; Cui, Z.; Zhou, X.; Cui, G. Cathode electrolyte interphase (CEI) endows Mo_6S_8 with Fast interfacial magnesium-ion transfer kinetics. *Angew. Chem. Int. Ed.* 2023, 62 (14), e202217709.

(50) Attias, R.; Salama, M.; Hirsch, B.; Gofer, Y.; Aurbach, D. Solvent effects on the reversible intercalation of magnesium-ions into V_2O_5 electrodes. *ChemElectroChem* 2018, 5 (22), 3514-3524.

(51) Ye, X.; Xiao, X.; Wu, Z.; Zhan, Y.; Wu, X.; Liu, S. Recent advances in rechargeable aqueous magnesium-ion batteries. *J. Mater. Chem. A* 2024.

(52) Novák, P.; Desilvestro, J. Electrochemical insertion of magnesium in metal oxides and sulfides from aprotic electrolytes. *J. ElectroChem. Soc.* 1993, 140 (1), 140.

(53) Huang, J.; Guo, Z.; Ma, Y.; Bin, D.; Wang, Y.; Xia, Y. Recent progress of rechargeable batteries using mild aqueous electrolytes. *Small Methods* 2019, 3 (1), 1800272.

(54) Wang, X.; Zhang, X.; Zhao, G.; Hong, H.; Tang, Z.; Xu, X.; Li, H.; Zhi, C.; Han, C. Ether-water hybrid electrolyte contributing to excellent Mg ion storage in layered sodium vanadate. *ACS Nano* 2022, 16(4), 6093-6102.

(55) Huang, M.; Wang, X.; Wang, J.; Meng, J.; Liu, X.; He, Q.; Geng, L.; An, Q.; Yang, J.; Mai, L. Proton/Mg^{2+} co-insertion chemistry in aqueous Mg-ion batteries: from the interface to the inner. *Angew. Chem. Int. Ed.* 2023, 62 (37), e202308961.

(56) Zhou, R.; Fan, K.; Hou, Z.; Liu, Q.; Huang, H.; Zhang, B. Synergistic proton and Mg^{2+}/Ca^{2+} insertion boosting aqueous divalent ion batteries. *Energy Storage Mater.* 2023, 63, 103012.

(57) Deng, M.; Wang, L.; Vaghefinazari, B.; Xu, W.; Feiler, C.; Lamaka, S. V.; Höche, D.; Zheludkevich, M. L.; Snihirova, D. High-energy and durable aqueous magnesium batteries:

recent advances and perspectives. *Energy Storage Mater.* 2021, 43, 238-247.

(58) Leong, K. W.; Pan, W.; Wang, Y.; Luo, S.; Zhao, X.; Leung, D. Y. C. Reversibility of a high-voltage, Cl^--regulated, aqueous Mg metal battery enabled by a water-in-salt electrolyte. *ACS Energy Lett.* 2022, 7 (8), 2657-2666.

(59) Zhu, Y.; Guo, X.; Lei, Y.; Wang, W.; Emwas, A.-H.; Yuan, Y.; He, Y.; Alshareef, H. N. Hydrated eutectic electrolytes for high-performance Mg-ion batteries. *Energy Environ. Sci.* 2022, 15 (3), 1282-1292.

(60) Song, X.; Ge, Y.; Xu, H.; Bao, S.; Wang, L.; Xue, X.; Yu, Q.; Xing, Y.; Wu, Z.; Xie, K.; Zhu, T.; Zhang, P.; Liu, Y.; Wang, Z.; Tie, Z.; Ma, J.; Jin, Z. Ternary eutectic electrolyte-assisted formation and dynamic breathing effect of the solid-electrolyte interphase for high-stability aqueous magnesium-ion full batteries. *J. Am. Chem. Soc.* 2024, 146(10), 7018-7028.

(61) Fu, Q.; Wu, X.; Luo, X.; Indris, S.; Sarapulova, A.; Bauer, M.; Wang, Z.; Knapp, M.; Ehrenberg, H.; Wei, Y.; Dsoke, S. High-voltage aqueous Mg-ion batteries enabled by solvation structure reorganization. *Adv. Funct. Mater.* 2022, 32 (16), 2110674.

(62) Xu, Y.; Liu, Z.; Zheng, X.; Li, K.; Wang, M.; Yu, W.; Hu, H.; Chen, W. Solid electrolyte interface regulated by solvent-in-water electrolyte enables high-voltage and stable aqueous Mg-MnO_2 batteries. *Adv. Energy Mater.* 2022, 12 (22), 2103352.

(63) Qu, K.; Lu, X.; Jiang, N.; Wang, J.; Tao, Z.; He, G.; Yang, Q.; Qiu, J. Eutectic electrolytes convoying low-temperature metal-ion batteries. *ACS Energy Lett.* 2024, 9 (3), 1192-1209.

(64) Zhong, Y.; Xie, X.; Zeng, Z.; Lu, B.; Chen, G.; Zhou, J. Triple-function hydrated eutectic electrolyte for enhanced aqueous zinc batteries. *Angew. Chem. Int. Ed.* 2023, 62 (40), e202310577.

(65) Song, S.; Kotobuki, M.; Zheng, F.; Li, Q.; Xu, C.; Wang, Y.; Li, W. D. Z.; Hu, N.; Lu, L. Communication—a composite polymer electrolyte for safer Mg batteries. *J. Electrochem. Soc.* 2017, 164 (4), A741.

(66) Bae, J.; Park, H.; Guo, X.; Zhang, X.; Warner, J. H.; Yu, G. High-performance magnesium

metal batteries via switching the passivation film into a solid electrolyte interphase. *Energy Environ. Sci.* 2021, 14 (8), 4391-4399.

(67) Shao, Y.; Rajput, N. N.; Hu, J.; Hu, M.; Liu, T.; Wei, Z.; Gu, M.; Deng, X.; Xu, S.; Han, K. S. Nanocomposite polymer electrolyte for rechargeable magnesium batteries. *Nano Energy* 2015, 12, 750-759.

(68) Du, A.; Zhang, H.; Zhang, Z.; Zhao, J.; Cui, Z.; Zhao, Y.; Dong, S.; Wang, L.; Zhou, X.; Cui, G. A Crosslinked Polytetrahydrofuran-borate-based polymer electrolyte enabling wide-working-temperature-range rechargeable magnesium batteries. *Adv. Mater.* 2019, 31 (11), e1805930.

(69) Li, Z.; Ganapathy, S.; Xu, Y.; Zhou, Z.; Sarilar, M.; Wagemaker, M. Mechanistic insight into the electrochemical performance of Zn/VO_2 batteries with an aqueous $ZnSO_4$ electrolyte. *Adv. Energy Mater.* 2019, 9 (22), 1900237.

(70) Xu, Y.; Deng, X.; Li, Q.; Zhang, G.; Xiong, F.; Tan, S.; Wei, Q.; Lu, J.; Li, J.; An, Q.; Mai, L. Vanadium oxide pillared by interlayer Mg^{2+} ions and water as ultralong-life cathodes for magnesium-ion batteries. *Chem* 2019, 5 (5), 1194-1209.

(71) Lu, T.; Chen, F. Multiwfn: A multifunctional wavefunction analyzer. *J. Comput. Chem.* 2012, 33 (5), 580-592.

(72) Xiao, Y.; Wang, Y.; Bo, S.-H.; Kim, J. C.; Miara, L. J.; Ceder, G. Understanding interface stability in solid-state batteries. *Nat. Rev. Mater.* 2020, 5 (2), 105-126.

(73) Liu, W.; Yi, C.; Li, L.; Liu, S.; Gui, Q.; Ba, D.; Li, Y.; Peng, D.; Liu, J. Designing polymer-in-salt electrolyte and fully infiltrated 3D electrode for integrated solid-state lithium batteries. *Angew. Chem. Int. Ed.* 2021, 133 (23), 13041-13050.

(74) Feiyang, C.; Zheng-Long, X. Design and manufacture of high-performance microbatteries: lithium and beyond. *Microstruct.* 2022, 2 (3), 2022012.

(75) Cheng, X.; Zhang, Z.; Kong, Q.; Zhang, Q.; Wang, T.; Dong, S.; Gu, L.; Wang, X.; Ma, J.; Han, P.; Lin, H. J.; Chen, C. T.; Cui, G. Highly reversible cuprous mediated cathode *chem*istry

for magnesium batteries. *Angew. Chem. Int. Ed.* 2020, 59 (28), 11477-11482.

(76) Zhao, Y.; Du, A.; Dong, S.; Jiang, F.; Guo, Z.; Ge, X.; Qu, X.; Zhou, X.; Cui, G. A bismuth-based protective layer for magnesium metal anode in noncorrosive electrolytes. *ACS Energy Lett.* 2021, 6 (7), 2594-2601.

(77) Tang, K.; Du, A.; Du, X.; Dong, S.; Lu, C.; Cui, Z.; Li, L.; Ding, G.; Chen, F.; Zhou, X.; Cui, G. A Novel Regulation strategy of solid electrolyte interphase based on anion-solvent coordination for magnesium metal anode. *Small* 2020, 16 (49), 2005424.

(78) He, Y.; Li, Q.; Yang, L.; Yang, C.; Xu, D. Electrochemical-conditioning-free and water-resistant hybrid $AlCl_3/MgCl_2/Mg(TFSI)_2$ electrolytes for rechargeable magnesium batteries. *Angew. Chem. Int. Ed.* 2019, 58 (23), 7615-7619.

(79) Li, R.; Yu, J.; Chen, F.; Su, Y.; Chan, K. C.; Xu, Z. L. High-power and ultrastable aqueous calcium-ion batteries enabled by small organic molecular crystal anodes. *Adv. Funct. Mater.* 2023, 33(30), 2214304.

(80) Zhou, X.; Li, G.; Yu, Y.; Lei, M.; Chen, K.; Li, C. Building organic–inorganic robust interphases from deep eutectic solution for highly stable Mg metal anode in conventional electrolyte. *Small Methods* 2023, 8 (7), 2301109.

(81) Hu, M.; Li, G.; Chen, K.; Zhou, X.; Li, C. A gradient structured SEI enabling record-high areal capacity anode for high-rate Mg metal batteries. *Chem. Eng. J.* 2024, 480, 148193.

(82) Li, Y.; Zhou, X.; Hu, J.; Zheng, Y.; Huang, M.; Guo, K.; Li, C. Reversible Mg metal anode in conventional electrolyte enabled by durable heterogeneous SEI with low surface diffusion barrier. *Energy Storage Mater.* 2022, 46, 1-9.

(83) Aravindan, V.; Karthikaselvi, G.; Vickraman, P.; Naganandhini, S. P. Polyvinylidene fluoride-based novel polymer electrolytes for magnesium-rechargeable batteries with Mg(CF3SO3)2. *J. Appl. Polym. Sci.* 2009, 112 (5), 3024-3029.

(84) Deivanayagam, R.; Cheng, M.; Wang, M.; Vasudevan, V.; Foroozan, T.; Medhekar, N. V.; Shahbazian-Yassar, R. Composite polymer electrolyte for highly cyclable room-temperature

solid-state magnesium batteries. *ACS Appl. Energy Mater.* 2019, 2 (11), 7980-7990.

(85) Oh, J.-S.; Ko, J.-M.; Kim, D.-W. Preparation and characterization of gel polymer electrolytes for solid state magnesium batteries. *Electrochim. Acta* 2004, 50 (2-3), 903-906.

(86) Pandey, G. P.; Agrawal, R. C.; Hashmi, S. A. Magnesium ion-conducting gel polymer electrolytes dispersed with fumed silica for rechargeable magnesium battery application. *J. Solid State Electr.* 2010, 15 (10), 2253-2264.

(87) Tripathi, S. K.; Jain, A.; Gupta, A.; Mishra, M. Electrical and electrochemical studies on magnesium ion-based polymer gel electrolytes. *J. Solid State Electr.* 2012, 16 (5), 1799-1806.

(88) Muldoon, J.; Bucur, C. B.; Oliver, A. G.; Zajicek, J.; Allred, G. D.; Boggess, W. C. Corrosion of magnesium electrolytes: chlorides – the culprit. *Energy Environ. Sci.* 2013, 6 (2), 482-487.

(89) Ma, L.; Li, X.; Zhang, G.; Huang, Z.; Han, C.; Li, H.; Tang, Z.; Zhi, C. Initiating a wearable solid-state Mg hybrid ion full battery with high voltage, high capacity and ultra-long lifespan in air. *Energy Storage Mater.* 2020, 31, 451-458.

(90) Yoo, H. D.; Liang, Y.; Dong, H.; Lin, J.; Wang, H.; Liu, Y.; Ma, L.; Wu, T.; Li, Y.; Ru, Q.; Jing, Y.; An, Q.; Zhou, W.; Guo, J.; Lu, J.; Pantelides, S. T.; Qian, X.; Yao, Y. Fast kinetics of magnesium monochloride cations in interlayer-expanded titanium disulfide for magnesium rechargeable batteries. *Nat. Commun.* 2017, 8 (1), 339.

(91) Li, Y.; Zuo, P.; Li, R.; Huo, H.; Ma, Y.; Du, C.; Gao, Y.; Yin, G.; Weatherup, R. S. Formation of an artificial Mg^{2+}-permeable interphase on Mg anodes compatible with ether and carbonate electrolytes. *ACS Appl. Mater. Interfaces* 2021, 13 (21), 24565-24574.

(92) Shuai, H.; Xu, J.; Huang, K. Progress in retrospect of electrolytes for secondary magnesium batteries. *Coord. Chem. Rev.* 2020, 422, 213478.

(93) Yoo, H. D.; Shterenberg, I.; Gofer, Y.; Gershinsky, G.; Pour, N.; Aurbach, D. Mg rechargeable batteries: an on-going challenge. *Energy Environ. Sci.* 2013, 6 (8), 2265-2279.

(94) Park, B.; Schaefer, J. L. Review—Polymer electrolytes for magnesium batteries: forging

away from analogs of lithium polymer electrolytes and towards the rechargeable magnesium metal polymer battery. *J. Electrochem. Soc.* 2020, 167 (7), 070545.

(95) Song, J.; Si, Y.; Guo, W.; Wang, D.; Fu, Y. Organosulfide-based deep eutectic electrolyte for lithium batteries. *Angew. Chem. Int. Ed.* 2021, 60 (18), 9881-9885.

(96) Qiu, H.; Hu, R.; Du, X.; Chen, Z.; Zhao, J.; Lu, G.; Jiang, M.; Kong, Q.; Yan, Y.; Du, J.; Zhou, X.; Cui, G. Eutectic crystallization activates solid-state zinc-ion conduction. *Angew. Chem. Int. Ed.* 2022, 61 (2), e202113086.

(97) Kim, H.-I.; Shin, E.; Kim, S.-H.; Lee, K. M.; Park, J.; Kang, S. J.; So, S.; Roh, K. C.; Kwak, S. K.; Lee, S.-Y. Aqueous eutectic lithium-ion electrolytes for wide-temperature operation. *Energy Storage Mater.* 2021, 36, 222-228.

(98) Zhao, J.; Zhang, J.; Yang, W.; Chen, B.; Zhao, Z.; Qiu, H.; Dong, S.; Zhou, X.; Cui, G.; Chen, L. "Water-in-deep eutectic solvent" electrolytes enable zinc metal anodes for rechargeable aqueous batteries. *Nano Energy* 2019, 57, 625-634.

(99) Yamanaka, T.; Hayashi, A.; Yamauchi, A.; Tatsumisago, M. Preparation of magnesium ion conducting $MgS–P_2S_5–MgI_2$ glasses by a mechanochemical technique. *Solid State Ion.* 2014, 262, 601-603.

(100) Smith, E. L.; Abbott, A. P.; Ryder, K. S. Deep eutectic solvents (DESs) and their applications. *Chem. Rev.* 2014, 114 (21), 11060-11082.

(101) Lu, X.; Hansen, E. J.; He, G.; Liu, J. Eutectic electrolytes chemistry for rechargeable Zn batteries. *Small* 2022, 18 (21), 2200550.

(102) Shuai, H.; Xu, J.; Huang, K. Progress in retrospect of electrolytes for secondary magnesium batteries. *Coord. Chem. Rev.* 2020, 422, 213478.

(103) Jiang, L. L.; Yan, C.; Yao, Y. X.; Cai, W.; Huang, J. Q.; Zhang, Q. Inhibiting solvent co-intercalation in a graphite anode by a localized high-concentration electrolyte in fast-charging batteries. *Angew. Chem. Int. Ed.* 2021, 60 (7), 3402-3406.

(104) Manivannan, M.; Rajendran, S. Investigation of inhibitive action of urea-Zn^{2+} system in

the corrosion control of carbon steel in sea water. *Int. J. Eng. Sci. Technol*. 2011, 3 (11), 8048-8060.

(105) Geng, L.; Wang, X.; Han, K.; Hu, P.; Zhou, L.; Zhao, Y.; Luo, W.; Mai, L. Eutectic electrolytes in advanced metal-ion batteries. *ACS Energy Lett.* 2022, 7 (1), 247-260.

(106) Liang, H.; Li, H.; Wang, Z.; Wu, F.; Chen, L.; Huang, X. New binary room-temperature molten salt electrolyte based on urea and LiTFSI. *J. Phys. Chem. B* 2001, 105 (41), 9966-9969.

(107) Manthiram, A.; Yu, X.; Wang, S. Lithium battery chemistries enabled by solid-state electrolytes. *Nat. Rev. Mater.* 2017, 2 (4), 16103.

(108) Lu, Z.; Schechter, A.; Moshkovich, M.; Aurbach, D. On the electrochemical behavior of magnesium electrodes in polar aprotic electrolyte solutions. *J. Electroanal. Chem.* 1999, 466 (2), 203-217.

(109) Amdisen, M. B.; Grinderslev, J. B.; Skov, L. N.; Jensen, T. R. Methylamine magnesium borohydrides as electrolytes for all-solid-state magnesium batteries. *Chem. Mater.* 2023, 35 (3), 1440-1448.

(110) Wei, Z.; Maile, R.; Riegger, L. M.; Rohnke, M.; Müller-Buschbaum, K.; Janek, J. Ionic liquid-incorporated metal-organic framework with high magnesium ion conductivity for quasi-solid-state magnesium batteries. *Batteries Supercaps* 2022, 5 (12), e202200318.

(111) Anilkumar, K. M.; Jinisha, B.; Manoj, M.; Jayalekshmi, S. Poly(ethylene oxide) (PEO) – poly(vinyl pyrrolidone) (PVP) blend polymer based solid electrolyte membranes for developing solid state magnesium ion cells. *Eur. Polym. J.* 2017, 89, 249-262.

(112) Aziz, A. A.; Tominaga, Y. Effect of Li salt addition on electrochemical properties of poly(ethylene carbonate)-Mg salt electrolytes. *Polym. J.* 2019, 51 (1), 61-67.

(113) Ramaswamy, M.; Malayandi, T.; Subramanian, S.; Srinivasalu, J.; Rangaswamy, M. Magnesium ion conducting polyvinyl alcohol–polyvinyl pyrrolidone-based blend polymer electrolyte. *Ionics* 2017, 23 (7), 1771-1781.

(114) Sarangika, H. N. M.; Dissanayake, M. A. K. L.; Senadeera, G. K. R.; Rathnayake, R. R.

D. V.; Pitawala, H. M. J. C. Polyethylene oxide and ionic liquid-based solid polymer electrolyte for rechargeable magnesium batteries. *Ionics* 2017, 23 (10), 2829-2835.

(115) Ab Aziz, A.; Tominaga, Y. Magnesium ion-conductive poly(ethylene carbonate) electrolytes. *Ionics* 2018, 24 (11), 3475-3481.

(116) Gershinsky, G.; Yoo, H. D.; Gofer, Y.; Aurbach, D. Electrochemical and spectroscopic analysis of Mg^{2+} intercalation into thin film electrodes of layered oxides: V_2O_5 and MoO_3. *Langmuir* 2013, 29 (34), 10964-10972.

(117) Sun, J.; Zou, Y.; Gao, S.; Shao, L.; Chen, C. Robust strategy of quasi-solid-state electrolytes to boost the stability and compatibility of Mg ion batteries. *ACS Appl. Mater. Interfaces* 2020, 12 (49), 54711-54719.

(118) Shao, Y.; Rajput, N. N.; Hu, J.; Hu, M.; Liu, T.; Wei, Z.; Gu, M.; Deng, X.; Xu, S.; Han, K. S.; Wang, J.; Nie, Z.; Li, G.; Zavadil, K. R.; Xiao, J.; Wang, C.; Henderson, W. A.; Zhang, J.-G.; Wang, Y.; Mueller, K. T.; Persson, K.; Liu, J. Nanocomposite polymer electrolyte for rechargeable magnesium batteries. *Nano Energy* 2015, 12, 750-759.

(119) Kisu, K.; Kim, S.; Inukai, M.; Oguchi, H.; Takagi, S.; Orimo, S.-i. Magnesium borohydride ammonia borane as a magnesium ionic conductor. *ACS Appl. Energy Mater.* 2020, 3 (4), 3174-3179.

(120) Manjuladevi, R.; Selvasekarapandian, S.; Thamilselvan, M.; Mangalam, R.; Monisha, S.; Selvin, P. C. A study on blend polymer electrolyte based on poly (vinyl alcohol)-poly (acrylonitrile) with magnesium nitrate for magnesium battery. *Ionics* 2018, 24 (11), 3493-3506.

(121) Abdel-Samiea, B. M.; Gamal, R.; Sheha, E. M. Effect of succinonitrile on electrical, structural and thermal properties of PVA-based polymer electrolyte for magnesium battery. *J. Energy Power Eng.* 2014, 8 (6).

(122) Li, B.; Masse, R.; Liu, C.; Hu, Y.; Li, W.; Zhang, G.; Cao, G. Kinetic surface control for improved magnesium-electrolyte interfaces for magnesium ion batteries. *Energy Storage Mater.* 2019, 22, 96-104.

(123) Zhang, D.; Duan, S.; Liu, X.; Yang, Y.; Zhang, Y.; Ren, W.; Zhang, S.; Cheng, M.; Yang, W.; Wang, J.; NuLi, Y. Deeping insight of $Mg(CF_3SO_3)_2$ and comprehensive modified electrolyte with ionic liquid enabling high-performance magnesium batteries. *Nano Energy* 2023, 109, 108257.

(124) Lee, H. J.; Park, Y. J. Interface characterization of MgF_2-coated $LiCoO_2$ thin films. *Solid State Ion.* 2013, 230, 86-91.

(125) Børresen, B.; Haarberg, G. M.; Tunold, R. Electrodeposition of magnesium from halide melts—charge transfer and diffusion kinetics. *Electrochim. Acta* 1997, 42 (10), 1613-1622.

(126) Yang, L.; Yang, C.; Chen, Y.; Pu, Z.; Zhang, Z.; Jie, Y.; Zheng, X.; Xiao, Y.; Jiao, S.; Li, Q.; Xu, D. Hybrid $MgCl_2/AlCl_3/Mg(TFSI)_2$ electrolytes in DME enabling high-rate rechargeable Mg batteries. *ACS Appl. Mater. Interfaces* 2021, 13 (26), 30712-30721.

(127) Gao, T.; Hou, S.; Huynh, K.; Wang, F.; Eidson, N.; Fan, X.; Han, F.; Luo, C.; Mao, M.; Li, X.; Wang, C. Existence of solid electrolyte interphase in Mg batteries: Mg/S chemistry as an example. *ACS Appl. Mater. Interfaces* 2018, 10 (17), 14767-14776.

(128) Gursu, H.; Gencten, M.; Sahin, Y. Preparation of sulphur-doped graphene-based electrodes by cyclic voltammetry: a potential application for vanadium redox flow battery. *Int. J. Electrochem. Sci.* 2018, 13, 875-885.

(129) Cao, Z.; Zheng, X.; Qu, Q.; Huang, Y.; Zheng, H. Electrolyte design enabling a high-safety and high-performance Si Anode with a tailored electrode-electrolyte interphase. *Adv. Mater.* 2021, 33 (38), e2103178.

(130) Zhang, Q.; Pan, J.; Lu, P.; Liu, Z.; Verbrugge, M. W.; Sheldon, B. W.; Cheng, Y. T.; Qi, Y.; Xiao, X. Synergetic effects of inorganic components in solid electrolyte interphase on high cycle efficiency of lithium ion batteries. *Nano Lett.* 2016, 16 (3), 2011-2016.

(131) Xiao, J.; Zhang, X.; Fan, H.; Zhao, Y.; Su, Y.; Liu, H.; Li, X.; Su, Y.; Yuan, H.; Pan, T.; Lin, Q.; Pan, L.; Zhang, Y. Stable solid electrolyte interphase *in situ* formed on magnesium-metal anode by using a perfluorinated alkoxide-based all-magnesium salt electrolyte. *Adv.*

Mater. 2022, 34 (30), e2203783.

(132) Du, Y.; Chen, Y.; Tan, S.; Chen, J.; Huang, X.; Cui, L.; Long, J.; Wang, Z.; Yao, X.; Shang, B.; Huang, G.; Zhou, X.; Li, L.; Wang, J.; Pan, F. Strong solvent coordination effect inducing gradient solid-electrolyte-interphase formation for highly efficient Mg plating/stripping. *Energy Storage Mater.* 2023, 62, 102939.

(133) Chen, T.; Ceder, G.; Sai Gautam, G.; Canepa, P. Evaluation of Mg compounds as coating materials in Mg batteries. *Front. Chem.* 2019, 7, 24.

(134) Chen, T.; Sai Gautam, G.; Canepa, P. Ionic transport in potential coating materials for Mg batteries. *Chem. Mater.* 2019, 31 (19), 8087-8099.

(135) Wan, J.; Wang, R.; Liu, Z.; Zhang, S.; Hao, J.; Mao, J.; Li, H.; Chao, D.; Zhang, L.; Zhang, C. Hydrated eutectic electrolyte induced bilayer interphase for high-performance aqueous Zn-ion batteries with 100 degrees c wide-temperature range. *Adv. Mater.* 2023, 36(11), e2310623.

(136) Geng, L.; Meng, J.; Wang, X.; Han, C.; Han, K.; Xiao, Z.; Huang, M.; Xu, P.; Zhang, L.; Zhou, L.; Mai, L. Eutectic electrolyte with unique solvation structure for high-performance zinc-ion batteries. *Angew. Chem. Int. Ed.* 2022, 61 (31), e202206717.

(137) Wang, S.; Wang, K.; Zhang, Y.; Jie, Y.; Li, X.; Pan, Y.; Gao, X.; Nian, Q.; Cao, R.; Li, Q.; Jiao, S.; Xu, D. High-entropy electrolyte enables high reversibility and long lifespan for magnesium metal anodes. *Angew. Chem. Int. Ed.* 2023, 62 (31), e202304411.

(138) Chen, R.; Zhang, C.; Li, J.; Du, Z.; Guo, F.; Zhang, W.; Dai, Y.; Zong, W.; Gao, X.; Zhu, J. A hydrated deep eutectic electrolyte with finely-tuned solvation chemistry for high-performance zinc-ion batteries. *Energy Environ. Sci.* 2023, 16 (6), 2540-2549.

(139) Cui, M.; Ma, N.; Lei, H.; Liu, Y.; Ling, W.; Chen, S.; Wang, J.; Li, H.; Li, Z.; Fan, J.; Huang, Y. I_3^-/I^- redox reaction-mediated organic zinc-air batteries with accelerated kinetics and long shelf lives. *Angew. Chem. Int. Ed.* 2023, 62 (26), e202303845.

(140) Li, G.; Li, Y.; Lei, M.; Chen, K.; Li, C. Multifunctional water additive enabling stable cycling of chloride-free magnesium metal batteries based on carbonate electrolyte. *Small* 2024,

20 (50), e2405568.

(141) Kopač Lautar, A.; Bitenc, J.; Rejec, T.; Dominko, R.; Filhol, J.-S.; Doublet, M.-L. Electrolyte reactivity in the double layer in mg batteries: an interface potential-dependent DFT study. *J. Am. Chem. Soc.* 2020, 142 (11), 5146-5153.

(142) Xu, D.; Liu, Z.; Liu, F.; Chen, M.; Zhou, D.; Xiao, Z. Stereochemistry-directed solvent molecular design for advanced lithium-sulfur batteries. *Chem. Eng. J.* 2025, 505, 159330.

(143) Chen, Y.; Yu, Z.; Rudnicki, P.; Gong, H.; Huang, Z.; Kim, S. C.; Lai, J.-C.; Kong, X.; Qin, J.; Cui, Y. Steric effect tuned ion solvation enabling stable cycling of high-voltage lithium metal battery. *J. Am. Chem. Soc.* 2021, 143 (44), 18703-18713.

(144) Théobald, F.; Cabala, R.; Bernard, J. Essai sur la structure de VO_2 (B). *J. Solid State Chem.* 1976, 17 (4), 431-438.

(145) Yi, Y.; Xing, Y.; Wang, H.; Zeng, Z.; Sun, Z.; Li, R.; Lin, H.; Ma, Y.; Pu, X.; Li, M. M.; Park, K. Y.; Xu, Z. L. Deciphering anion-modulated solvation structure for calcium intercalation into graphite for Ca-ion batteries. *Angew. Chem. Int. Ed.* 2024, e202317177.

(146) Chen, Y.; Atwi, R.; Nguyen, D. T.; Bazak, J. D.; Hahn, N. T.; Ryu, J.; Sears, J. A.; Han, K. S.; Song, M.; Li, Z.; Karkamkar, A. J.; Hu, J. Z.; Zavadil, K. R.; Rajput, N. N.; Mueller, K. T.; Murugesan, V. From bulk to interface: solvent exchange dynamics and their role in ion transport and the interfacial model of rechargeable magnesium batteries. *J. Am. Chem. Soc.* 2024, 146 (19), 12984-12999.

(147) Vujković, M.; Pašti, I.; Simatović, I. S.; Šljukić, B.; Milenković, M.; Mentus, S. The influence of intercalated ions on cyclic stability of V_2O_5/graphite composite in aqueous electrolytic solutions: experimental and theoretical approach. *Electrochim. Acta* 2015, 176, 130-140.

(148) Tang, H.; Xiong, F.; Jiang, Y.; Pei, C.; Tan, S.; Yang, W.; Li, M.; An, Q.; Mai, L. Alkali ions pre-intercalated layered vanadium oxide nanowires for stable magnesium ions storage. *Nano Energy* 2019, 58, 347-354.

(149) Zhang, H.; Ye, K.; Zhu, K.; Cang, R.; Wang, X.; Wang, G.; Cao, D. Assembly of aqueous rechargeable magnesium ions battery capacitor: the nanowire Mg-OMS-2/graphene as cathode and activated carbon as anode. *ACS Sustain. Chem. Eng.* 2017, 5 (8), 6727-6735.

(150) Wang, F.; Fan, X.; Gao, T.; Sun, W.; Ma, Z.; Yang, C.; Han, F.; Xu, K.; Wang, C. High-voltage aqueous magnesium ion batteries. *ACS Cent. Sci.* 2017, 3 (10), 1121-1128.

(151) Pei, C.; Yin, Y.; Liao, X.; Xiong, F.; An, Q.; Jin, M.; Zhao, Y.; Mai, L. Structural properties and electrochemical performance of different polymorphs of Nb_2O_5 in magnesium-based batteries. *J. Energy Chem.* 2021, 58, 586-592.

(152) Gu, M.; Zhou, X.; Yang, Q.; Chu, S.; Li, L.; Li, J.; Zhao, Y.; Hu, X.; Shi, S.; Chen, Z. Anion-reinforced solvation structure enables stable operation of ether-based electrolyte in high-voltage potassium metal batteries. *Angew. Chem. Int. Ed.* 2024, 136(30), e202402946.

(153) Zhou, X.; Huang, Y.; Wen, B.; Yang, Z.; Hao, Z.; Li, L.; Chou, S.-L.; Li, F. Regulation of anion–Na^+ coordination chemistry in electrolyte solvates for low-temperature sodium-ion batteries. *Proc. Natl. Acad. Sci.* 2024, 121 (5), e2316914121.

(154) Wang, Y.; Wang, J.; Zhang, W.; Chao, F.; Li, J.; Kong, Q.; Qiao, F.; Zhang, L.; Huang, M.; An, Q. Promising VO_2(B)/rGO heterojunction cathode for building high-capacity and long-lifespan Ca-ion batteries. *Adv. Funct. Mater.* 2024, 34(27), 2314761.

(155) Li, M.; Li, C.; Zuo, C.; Hu, J.; Li, C.; Luo, W.; Luo, S.; Duan, A.; Wang, J.; Wang, X.; Sun, W.; Mai, L. Strategically modulating proton activity and electric double layer adsorption for innovative all-vanadium aqueous Mn^{2+}/proton hybrid batteries. *Adv. Mater.* 2024, 36(41), e2407233.

(156) Dou, H.; Zhao, X.; Zhang, Y.; Zhao, W.; Yan, Y.; Ma, Z.-F.; Wang, X.; Yang, X. Revisiting the degradation of solid/electrolyte interfaces of magnesium metal anodes: decisive role of interfacial composition. *Nano Energy* 2021, 86, 106087.

(157) Zhang, J.; Liu, J.; Wang, M.; Zhang, Z.; Zhou, Z.; Chen, X.; Du, A.; Dong, S.; Li, Z.; Li, G. The origin of anode–electrolyte interfacial passivation in rechargeable Mg-metal batteries.

Energy Environ. Sci. 2023, 16 (3), 1111-1124.

(158) Ruiz, R.; Pérez-Vicente, C.; Rubio, S.; Stoyanova, R.; Zuo, W.; Yang, Y.; Ortiz, G. F. A Cubic Mg_2MnO_4 Cathode for non-aqueous magnesium batteries. *Energy Storage Mater.* 2022, 48, 12-19.

(159) Rubio, S.; Liang, Z.; Liu, X.; Lavela, P.; Tirado, J. L.; Stoyanova, R.; Zhecheva, E.; Liu, R.; Zuo, W.; Yang, Y.; Pérez-Vicente, C.; Ortiz, G. F. Reversible multi-electron storage enabled by $Na_5V(PO_4)_2F_2$ for rechargeable magnesium batteries. *Energy Storage Mater.* 2021, 38, 462-472.

(160) Johnson, I. D.; Nolis, G.; Yin, L.; Yoo, H. D.; Parajuli, P.; Mukherjee, A.; Andrews, J. L.; Lopez, M.; Klie, R. F.; Banerjee, S. Enhanced charge storage of nanometric ζ-V_2O_5 in Mg electrolytes. *Nanoscale* 2020, 12 (43), 22150-22160.

(161) Idemoto, Y.; Kawakami, N.; Ishida, N.; Kitamura, N. Synthesis, electrochemical properties, and changes in crystal and electronic structures during charge/discharge process of spinel-type cathode materials $Mg_4V_{5-x}Ni_xO_{12}$ (x = 0, 0.3, 0.6, 1.0) for magnesium secondary batteries. *J. Power Sources* 2020, 455, 227962.

(162) Fu, Q.; Wu, X.; Luo, X.; Ding, Z.; Indris, S.; Sarapulova, A.; Meng, Z.; Desmau, M.; Wang, Z.; Hua, W.; Kübel, C.; Schwarz, B.; Knapp, M.; Ehrenberg, H.; Wei, Y.; Dsoke, S. Ca^{2+} pre-intercalated bilayered vanadium oxide for high-performance aqueous Mg-ion batteries. *Energy Storage Mater.* 2024, 66, 103212.

(163) Deng, R.; Wang, Z.; Tan, S.; Huang, X.; Gao, Z.; Fang, Y.; Chen, C.; Wang, R.; Xu, C.; Huang, G.; Wang, J.; Pan, F. Optimization of the electrode reaction kinetics of V_2O_5 via polyacrylonitrile intercalation for high-performance magnesium batteries. *Chem. Eng. J.* 2024, 489, 151095.

(164) Zhang, S.; Sun, Y.; Zeng, X.; Yang, J.; Wang, J.; NuLi, Y. PEG-based co-solvent aqueous electrolytes enabling high-energy rechargeable aqueous magnesium-ion batteries. *Nano Energy* 2024, 132, 110307.

(165) Andrews, J. L.; Mukherjee, A.; Yoo, H. D.; Parija, A.; Marley, P. M.; Fakra, S.; Prendergast, D.; Cabana, J.; Klie, R. F.; Banerjee, S. Reversible Mg-ion insertion in a metastable one-dimensional polymorph of V_2O_5. *Chem* 2018, 4 (3), 564-585.

(166) Fu, Q.; Sarapulova, A.; Trouillet, V.; Zhu, L.; Fauth, F.; Mangold, S.; Welter, E.; Indris, S.; Knapp, M.; Dsoke, S.; Bramnik, N.; Ehrenberg, H. In operando synchrotron diffraction and in operando X-ray absorption spectroscopy investigations of orthorhombic V_2O_5 nanowires as cathode materials for Mg-ion batteries. *J. Am. Chem. Soc.* 2019, 141 (6), 2305-2315.

(167) Lv, Z.; Tang, R.; Sun, C.; Meng, W.; Yang, J.; Li, S.; Wu, Q.; Zhang, M.; Zhao, J.; Yang, Y. Inhibiting cathode dissolution and shuttling of V–O species using a polybenzimidazole hydrogel electrolyte for durable high-areal-capacity Zn–V_2O_5 batteries. *Energy Environ. Sci.* 2025, 18(2), 762-773.

(168) Zhong, W.; Shen, Z.; Mao, J.; Zhang, S.; Cheng, H.; Kim, Y.; Lu, Y. Mitigating cathodic dissolution through interfacial water masking to enhance the longevity of aqueous zinc–ion batteries. *Energy Environ. Sci.* 2024, 17 (5), 2059-2068.

(169) Dou, X.; Xie, X.; Liang, S.; Fang, G. Low-current-density stability of vanadium-based cathodes for aqueous zinc-ion batteries. *Sci. Bull.* 2024, 69 (6), 833-845.

(170) Zhang, C.; Zhang, L.; Yu, G. Eutectic electrolytes as a promising platform for next-generation electrochemical energy storage. *Acc. Chem. Res.* 2020, 53 (8), 1648-1659.

(171) Yang, W.; Du, X.; Zhao, J.; Chen, Z.; Li, J.; Xie, J.; Zhang, Y.; Cui, Z.; Kong, Q.; Zhao, Z.; Wang, C.; Zhang, Q.; Cui, G. Hydrated eutectic electrolytes with ligand-oriented solvation shells for long-cycling zinc-organic batteries. *Joule* 2020, 4 (7), 1557-1574.

(172) Wang, Y.; Wang, T.; Dong, D.; Xie, J.; Guan, Y.; Huang, Y.; Fan, J.; Lu, Y.-C. Enabling high-energy-density aqueous batteries with hydrogen bond-anchored electrolytes. *Matter* 2022, 5 (1), 162-179.

(173) An, Q.; Zhang, W.; Zhu, S.; Yang, T.; Wu, L.; Li, J.; Liang, J.; Liu, Y.; Cui, L.; Tang, C.; Chen, X.; Zhou, H.; Qiao, F.; Zhou, M.; Luo, P.; Chi, F.; Liao, X.; Zhang, L. Hydrogen/electron

amphiphilic bi-functional water molecular inactivator-assisted interface stabilization in highly reversible Zn metal batteries. *Angew. Chem. Int. Ed.* 2024, e202419732.

(174) Petit, T.; Puskar, L.; Dolenko, T.; Choudhury, S.; Ritter, E.; Burikov, S.; Laptinskiy, K.; Brzustowski, Q.; Schade, U.; Yuzawa, H.; Nagasaka, M.; Kosugi, N.; Kurzyp, M.; Venerosy, A.; Girard, H.; Arnault, J.-C.; Osawa, E.; Nunn, N.; Shenderova, O.; Aziz, E. F. Unusual water hydrogen bond network around hydrogenated nanodiamonds. *J. Phys. Chem. C* 2017, 121 (9), 5185-5194.

(175) Wang, Y.; Wang, Z.; Pang, W. K.; Lie, W.; Yuwono, J. A.; Liang, G.; Liu, S.; Angelo, A. M.; Deng, J.; Fan, Y.; Davey, K.; Li, B.; Guo, Z. Solvent control of water O-H bonds for highly reversible zinc ion batteries. *Nat. Commun.* 2023, 14 (1), 2720.

(176) Lin, H.; Zeng, L.; Lin, C.; Wu, J.; He, H.; Huang, C.; Lai, W.; Xiong, P.; Xiao, F.; Qian, Q.; Chen, Q.; Lu, J. Interfacial regulation via configuration screening of a disodium naphthalenedisulfonate additive enabled high-performance wide-pH Zn-based batteries. *Energy Environ. Sci.* 2025, 18 (3), 1282-1293.

(177) Wang, Y.; Wang, T.; Bu, S.; Zhu, J.; Wang, Y.; Zhang, R.; Hong, H.; Zhang, W.; Fan, J.; Zhi, C. Sulfolane-containing aqueous electrolyte solutions for producing efficient ampere-hour-level zinc metal battery pouch cells. *Nat. Commun.* 2023, 14 (1), 1828.

(178) Liu, S.; He, J.; Liu, D.-s.; Ye, M.; Zhang, Y.; Qin, Y.; Li, C. C. Suppressing vanadium dissolution by modulating aqueous electrolyte structure for ultralong lifespan zinc ion batteries at low current density. *Energy Storage Mater.* 2022, 49, 93-101.

(179) Yue, J.; Lin, L.; Jiang, L.; Zhang, Q.; Tong, Y.; Suo, L.; Hu, Y.-s.; Li, H.; Huang, X.; Chen, L. Interface concentrated-confinement suppressing cathode dissolution in water-in-salt electrolyte. *Adv. Energy Mater.* 2020, 10 (36), 2000665.

(180) Peng, Z.; Tang, L.; Li, S.; Tan, L.; Chen, Y. Strong Replaces Weak: Hydrogen bond-anchored electrolyte enabling ultra-stable and wide-temperature aqueous zinc-ion capacitors. *Angew. Chem. Int. Ed.* 2024, e202418242.

(181) Niu, H.; Liu, H.; Yang, L.; Kang, T.; Shen, T.; Jiang, B.; Huang, W.-H.; Chang, C.-C.; Pei, Y.; Cao, G.; Liu, C. Impacts of distorted local chemical coordination on electrochemical performance in hydrated vanadium pentoxide. *Nat. Commun.* 2024, 15 (1), 9421.